Title

Synthesis and Applications of Graphene Nanoribbons and Heterostructures from Molecular Precursors

Author

Perkins, Wade Scott

Publication Date

2017

Synthesis and Applications of Graphene Nanoribbons and Heterostructures from Molecular Precursors

by

Wade Scott Perkins

A dissertation submitted in partial satisfaction of the

requirements for the degree of

Doctor of Philosophy

in

Chemistry

in the

Graduate Division

of the

University of California, Berkeley

Committee in charge:

Professor Felix Fischer, Chair
Professor K. Peter Vollhardt
Professor Richmond Sarpong
Professor James Analytis

Spring 2017

Synthesis and Applications of Graphene Nanoribbons and Heterostructures from Molecular Precursors

Abstract

Synthesis and Applications of Graphene Nanoribbons and Heterostructures from Molecular Precursors

by

Wade Scott Perkins

Doctor of Philosophy in Chemistry

University of California, Berkeley

Professor Felix Fischer, Chair

Graphene nanoribbons (GNRs), nanometer wide strips of graphene with extraordinary electronic and physical properties, represent the cutting edge of post-silicon electronics development. These nanomaterials boast potential solutions to downsizing of future electronics in both size and energy consumption, as well as opening the door to faster processing. Novel GNRs of varied width and heteroatom incorporation were synthesized in a surface assisted bottom-up fashion from novel small molecule precursors (Chapter 2). The advancement of GNR based technologies to new and advanced architectures requires the controlled formation of functional GNR heterostructures, and to this end, a GNR-porphyrin-GNR heterostructure was designed and developed which is shown to self-assemble on functionalized surfaces (Chapter 3). Furthermore, bulk GNRs are shown to have practical applications beyond the single ribbon scale, acting as functional support materials for inorganic nanoparticles (Chapter 4). This work advances both the development and applications of bottom-up synthesized GNRs.

Contents

List of Figures

List of Tables

Acknowledgments

I would like to thank my amazing family, who always stood by me and believed in me. I would also like to thank my friends and labmates, whose thought provoking conversation and help were invaluable. And lastly, I would like to thank my numerous collaborators, without whom little of this would have been possible.

Chapter 1

Introduction

In the first chapter of this thesis graphene, synthetic methods, and applications are introduced. Motivation for confinement of graphene into atomically precise narrow graphene nanoribbons is provided, and existing synthetic methods and characterization tools are explored. This provides a literature foundation for the novel synthetic methods, heteromaterials, and applications that will make up Chapters 2–4.

1.1 Graphene

Prior to its isolation in 2004,[1] graphene, a single atom layer of hexagonally arranged carbon atoms, was thought by many researchers to be too unstable for isolation due to the tendency to roll into other carbon allotropes such as fullerenes and carbon nanotubes (CNTs).[2–7] Since the discovery of the so called "Scotch-tape method" of repeated mechanical exfoliation of graphite flakes that first produced single-layer graphene, it has become one of the most intensely researched topics in materials, prompting the 2010 Nobel Prize in physics for Novoselov and Geim. Among the properties that have drawn significant attention for future electronics and materials applications are its outstanding charge carrier mobility (250,000 $\mathrm{cm^2/Vs}$, orders of magnitude higher than silicon),[8] high specific surface area (2630 $\mathrm{m^2/g}$),[9] thermal conductivity (5,000 W/mK),[10] high Young's modulus (1.0 TPa),[11] and remarkably high optical transparency (97.7%)[12] which make it an attractive material for flexible and optical electronics.

Today, a variety of synthetic methods for single- and few-layer graphene sheets exist. In addition to mechanical exfoliation via scotch tape, exfoliation of graphite using a ball mill,[13] as well as surfactant mediated electrochemical exfoliation,[14,15] have been shown to be viable options. Graphene can also be grown epitaxially on metal substrates,[16,17] among other methods. However, synthesis by chemical vapor deposition on various transition metal surfaces using solid,[18–26] liquid,[22,27–32] or gaseous[32–40] starting materials is the most commercially viable synthetic method for large, well controlled sheets.

Many electronic applications of graphene hinge on two main factors besides quality and scale of the synthesis. The first is the need to transfer the graphene sheet off of the metal surfaces that are commonly used for its synthesis onto a dielectric substrate such that the electronic properties of the graphene are not overshadowed by the metal substrate. This has been addressed in a variety of ways including polymer-assisted transfer,[41–44] roll-to-roll-transfer methods,[45,46] and even direct growth on dielectrics.[47,48] The second is the need for a bandgap for semiconducting applications. Because graphene is intrinsically semi-metallic in its conductance due to a lack of bandgap, new methods are required to modify the electronic structure of graphene. The most promising of which is lateral confinement of graphene into high aspect ratio strips of graphene called graphene nanoribbons (GNRs) that feature a tunable bandgap due to quantum confinement.

1.2 Graphene Nanoribbons

Graphene nanoribbons (GNRs) are semiconducting quasi-one dimensional strips of graphene whose electronic and magnetic properties depend heavily on their width and edge structure. Three of the most commonly investigated types of GNR edge structures (armchair or AGNRs, zig-zag or ZGNRs, and cove type GNRs) are shown in Figure 1.1. Due to the extremely sensitive relationship between the physical and electronic structures, high precision and reproducibility are key factors to be considered when developing a GNR synthetic method.

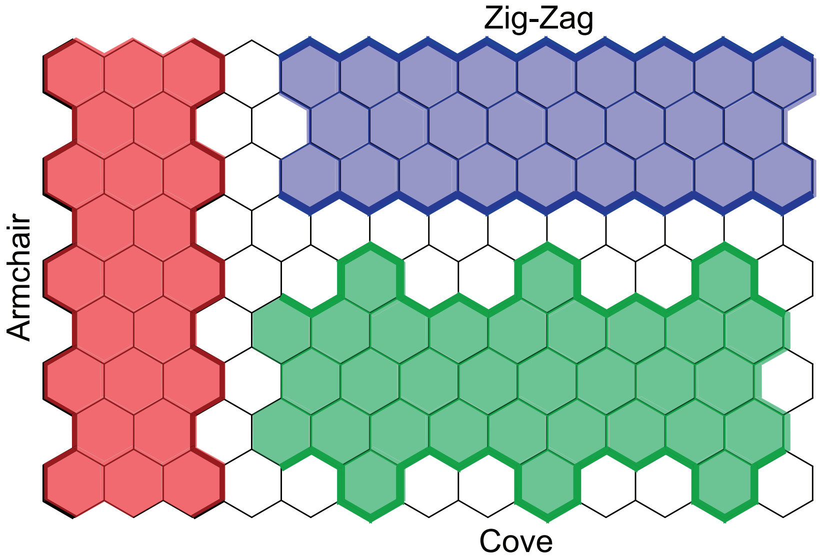

Figure 1.1: Three of the most commonly investigated graphene nanoribbon edge structures: armchair, zig-zag, and cove-type.

Researchers round the world have investigated synthetic methods that fall into two main categories: top-down and bottom-up synthesis.

Top-Down Synthesis

Top-down syntheses of GNRs start with larger graphitic structures (graphene, graphite, carbon nanotubes), and laterally confine them using a variety of methods. These methods commonly boast advantages in generation of commercially viable amounts of material, however confinement down to the sub 10 nm width scale and control over edge structure remain major challenges in the field.

GNRs by Sonication of Graphite

One method of top-down GNR fabrication that excels in smooth edges, high aspect ratios, and bulk production is the sonochemical cutting of graphite flakes. This method commonly makes use of dispersing a graphite flake in an aqueous solution using surfactants (such as sodium dodecyl sulfate or SDS) and strong oxidizing acids (H_2SO_4 or HNO_3) along with a templating polymer [PVP,[51] PmPV,[50] or self assembled flavin monocucleotide (FMV)[49]]. The primary challenges associated with using this methodology are the need to overcome the strong van der Waals forces between graphene sheets and the directional unzipping, which are addressed by the use of varied surfactants and templates.

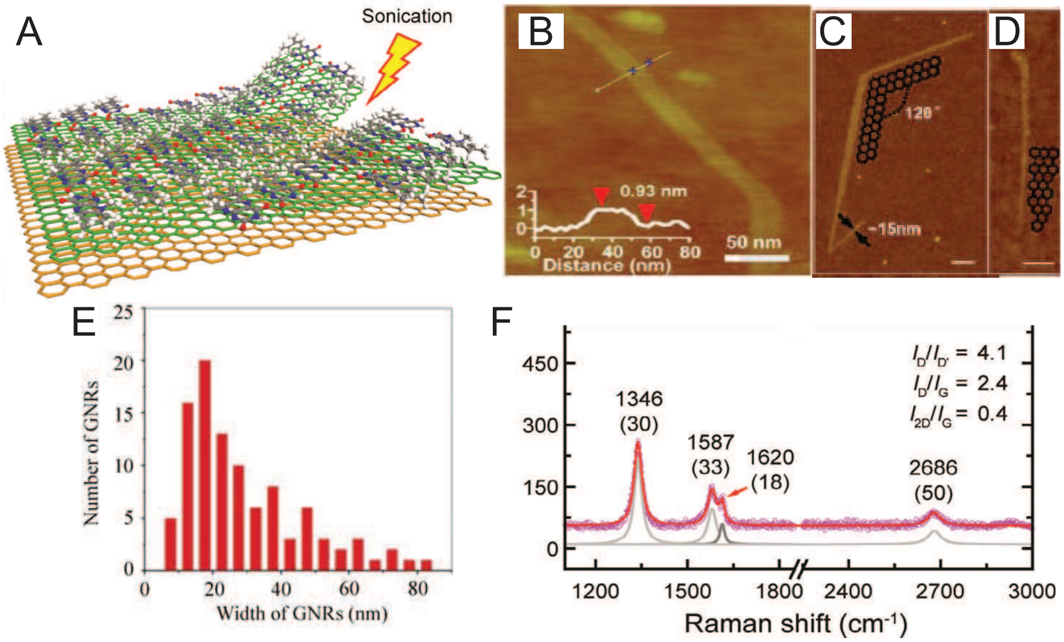

Figure 1.2: A) Representation of non-covalently templated sonication cutting of graphite. [Reproduced from reference[49]] B-D) AFM images of GNRs produced by sonication displaying a variety of defects. [Reproduced from references[50,51]] E) Histogram of GNR widths produced by sonication.[Reproduced from reference[51]] F) Raman spectra of GNRs produced by sonication showing broad peaks and high D/G ratio. [Reproduced from reference[49]]

However, the smooth edges touted by this method are commonly defined by having edge roughness smaller than the ribbon width, and do not have edges aligned with a crystallographic axis, which would lead to the atomically defined A- or ZGNRs. Indeed, examples of AFM topographical images include, in addition to edge roughness, defects such as kinks or wedge shaped ribbons as seen in Figure 1.2B, C, and D.[50 51] Furthermore, while this technique has been shown to produce ribbons that are sub 10 nm in width, the control is such that ribbons are always produced as a wide assortment of widths as seen in Figure 1.2E, which leads to large variability in electrical properties. Evidence for defects, which can include vacancies, edge functionalization, and topological defects, can be readily seen in the Raman spectra of the materials which tend to feature broad G peaks, as well as high D/G or D'/G ratios (Figure 1.2F).

While impressive device measurements have been obtained using GNRs produced in this method, such as the I_{on}/I_{off} ratios of up to 10^7 in a GNR FET,[50] the reproducibility is sufficiently low that these methods are inadequate for reliable fabrication of electronic devices.

GNRs by Unzipping Carbon Nanotubes

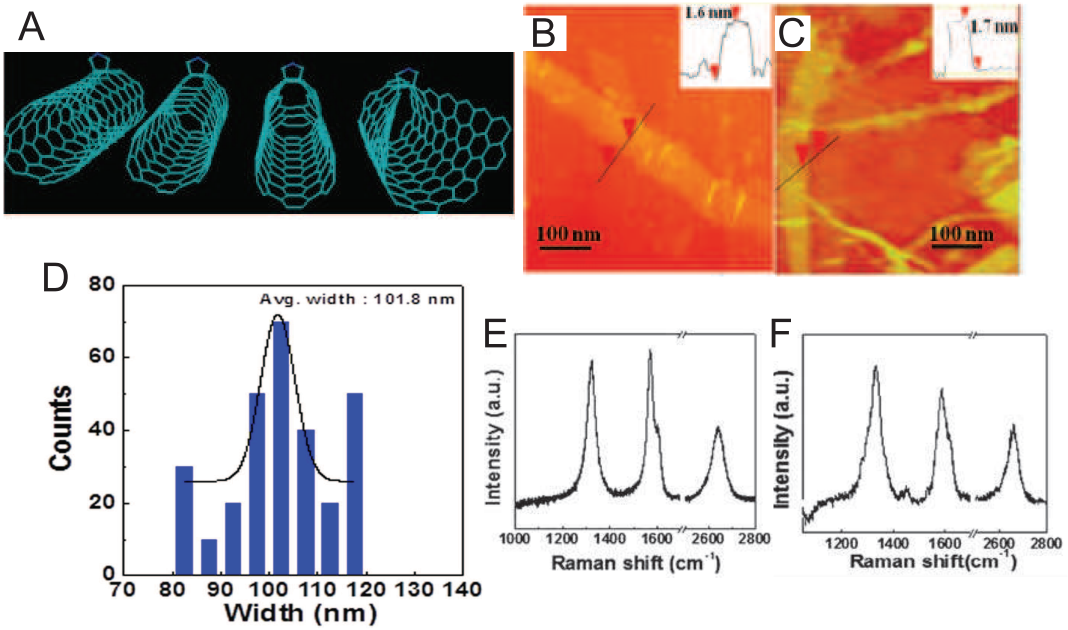

Figure 1.3: A) 3D representation of partial longitudinal unzipping of a CNT triggered by a sidewall modification. [Reproduced from reference[52]] AFM images of GNRs made by electrochemical unzipping of MWCNTs at B) 0.7V and C) 0.5V [Reproduced from reference[53]] D) Width distribution of GNRs produced by intercalation assisted oxidative unzipping of MWCNTs. [Reproduced from reference[54]] E)and F)Representative Raman spectra of GNRs produced by laser induced unzipping of MWCNTs. [Reproduced from reference[55]]

One of the most explored top-down methods of GNR synthesis that performs well in terms of bulk production and length is from the longitudinal unzipping of CNTs as shown in Figure 1.3A. This has been accomplished using both single-walled and multi-walled CNTs (SWCNT and MWCNT respectively), with unzipping derived from chemical oxidation, high pressure reduction with H_2, laser pulses, intercalation of ions (Li^+, K^+, NO_3^-, $SO_4{}^{2-}$, and others) in strong acid (H_2SO_4), followed by exfoliation with $KMnO_4$.

The harsh oxidative conditions commonly employed in chemical unzipping are well known to lead to a variety of edge oxidation products and disorder.[54] Other methods, including reductive unzipping,[56] electrochemical unzipping,[53] laser-induced unzipping,[55] and unzipping through a combination of other chemical reactivity and STM tip manipulation[52] are capable of limiting the amount of edge oxidation, but do not reduce the edge disorder and still lead to ribbons with highly defective edges, as seen in example AFM images (Figure 1.3B and C). A primary shortcoming of using CNTs as a starting material, is that the as-synthesized CNTs are always a mixture of various chiralities, with $\frac{1}{3}$ being metallic conductors. This means that regardless of the unzipping method, the edge chirality of the produced GNR will always be an uncontrolled mixture leading to inconsistent electronic properties. Furthermore, the width of the GNR will always be limited by the diameter of the CNT, leading to GNRs far larger than the desirable < 10 nm width (Figure 1.3D).

GNRs by Etching Graphene

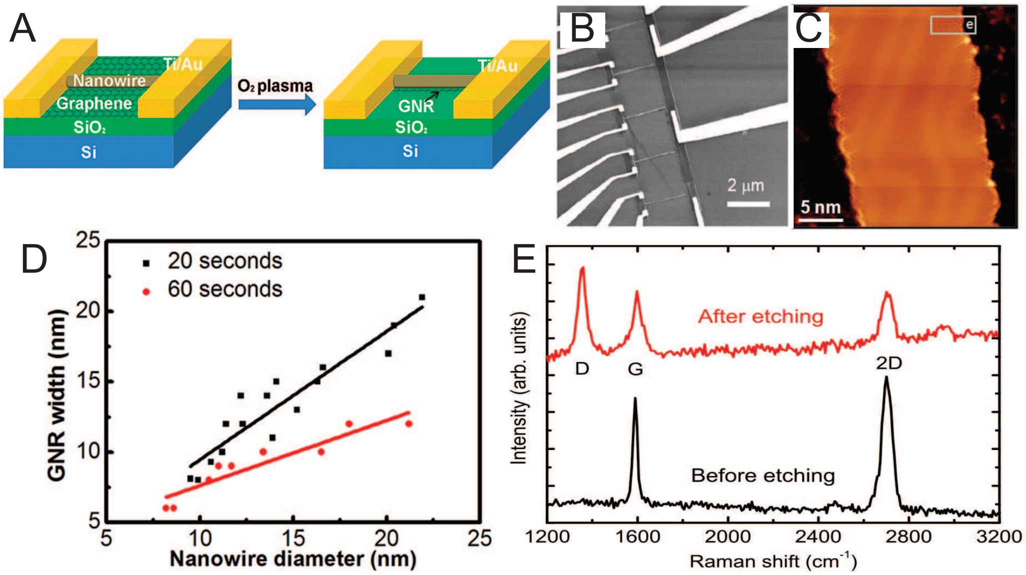

Figure 1.4: A) Schematic representation of a device based on GNRs etched from graphene with a nanowire mask. [Reproduced from reference[57]] B) SEM image of device with GNRs etched in a parallel arrangement. [Reproduced from reference[58]] C) STM topograph of GNRs made from chemically unzipped CNTs followed by H_2 plasma etching. [Reproduced from reference[59]] D) Scaling of GNR width with mask size under O_2 plasma treatment. [Reproduced from reference[57]] E) Comparison of Raman signal of a pristine graphene sheet and the GNR after etching. [Reproduced from reference[60]]

Fabrication of GNRs by etching graphene sheets is a synthetic method with advantages in both generating aligned GNRs (Figure 1.4B) and in making integrated interconnects by patterned cutting. This gives etched GNR devices an advantage over other methods with regards to avoiding the Schottky barrier dominated performance common in CNT devices due to the crystallographic continuity of the GNR and electronic connections.[57,58]

Most etch methods follow a scheme similar to that seen in Figure 1.4A, whereby metal electrodes are patterned onto a sheet of graphene using electron beam lithography (EBL), and a lithography resistant mask (commonly either a polymer or nanowire) is patterned onto the sheet to define the desired GNR. The extraneous, surrounding graphene is then etched away using O_2 plasma,[57,58,61] H_2 plasma,[59] or reactive ion etching (Ga^+, He^+, etc.).[60]

However, these harsh treatments cause significant defects along the edges of the GNRs, including oxidation from the O_2 plasma and roughness and disorder, as can be seen in the high resolution STM topograph in Figure 1.4C. In addition, while some methods have successfully produced GNRs in the sub-10 nm regime,[57] such examples are uncommon and still lack the control to generate such ribbons reproducibly (Figure 1.4D). Devices fabricated from etched GNRs of width > 20 nm tend to suffer from low transport gap values arising from the wide ribbons.[58,61,62] Transistors based on etched GNRs also suffer from low I_{on}/I_{off}, with ratios on the order of 10^2 being considered impressive.[57,63]

Bottom-Up Synthesis

In order to preserve the predicted properties of GNRs in a realized ribbon, complete atomic precision over the width and edge structure are required. Where the previous top-down fabrication methodologies all failed in this endeavor, bottom-up synthesis of molecular precursors succeeds. By utilizing a two step sequence of polymerization followed by cyclodehydrogenation starting from molecular precursors defined by organic synthesis, the precise width, edge structure, and doping pattern of a GNR can be controlled. This has been accomplished both on metal surfaces in UHV, as well as in solution. These two complementary methods have their own advantages with regards to available characterization, scale, and unique functionalization given the different reaction pathways.

On Surface Bottom-Up Synthesis of GNRs

The first example of on-surface bottom-up synthesis of atomically precise GNRs was published in 2010, when Cai et al. reported the synthesis of both $N = 7$ AGNRs (where N is the width of the ribbon in number of carbon atoms) and Chevron type GNRs as shown schematically in Figure 1.5.[64] In this precedent setting report, a dibrominated monomer was deposited on a Au(111) surface and annealed to enable a surface catalyzed homolytic bond cleavage, resulting in a diradical species that can diffuse about the surface and recombine to form the C-C bonds that make up the precursor polymer backbone. At an elevated annealing temperature, the precursor polymer is cyclodehydrogenated to planaraize and graphetize the material, resulting in a GNR whose width and edge structure are perfectly controlled. Due to the hermetic environment, issues such as incorporation of oxidation products or dangling bonds are excluded. This is confirmed by high resolution STM as well as XPS. Furthermore, single ribbon electronic characterization is possible with this technique, although the experimental results differ from those previously calculated due to an effect of screening and hybridization due to the gold surface. This can best be compensated for in calculations using an image charge model.

This biradical polymerization technique was then utilized in reports that expand upon the number and type of GNRs available. In 2013, the first example of a wider, controlled AGNR was published.[65] By modifying the bisanthracene core to include biphenyl substituents, the resulting GNR is instead 13 atoms across, lowering the observed bandgap by 1.2 eV from

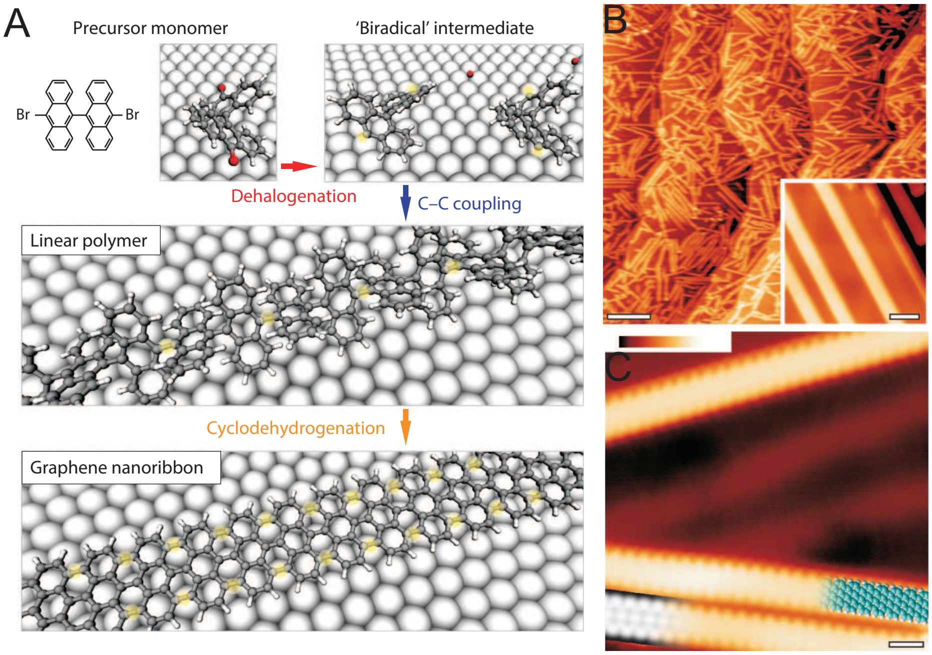

Figure 1.5: On-surface synthesis of $N = 7$ AGNRs from dibromobisanthracene monomer. [Reproduced from reference[64]] A)The dihalogenated monomer is deposited on a Au(111) surface under UHV and annealed to induce homolytic bond cleavage, resulting in a biradical intermediate. This diffuses about the surface and recombines to form the linear precursor polymer. At a higher annealing temperature, the precursor polymer is cyclodehydrogenated to produce the desired GNR. B) STM image of $N = 7$ AGNRs imaged at room temperature and C) High resolution STM of $N = 7$ AGNRs taken at 5 K.

the $N = 7$ case to 1.4 eV (Figure 1.6A and B). While in the case of $N = 7$ AGNRs the authors observe ribbon lengths of $\sim$ 30 nm,[64] in the case of $N = 13$ AGNRs the ribbons observed are significantly shorter (11 nm). The authors claim this length decrease is due to a length limiting quenching of the aryl radicals via hydrogen abstraction.[65] Additionally, it can be observed that there are electronic states associated with the ends of ribbons that extend $\sim$ 30 Å from the edges, at which point the bulk electronic structure is reached.

The first reported member of the lowest predicted bandgap $N = 3p + 2$ family came in 2015 when Zhang et al. synthesized $N = 5$ AGNRs starting from tetrabromonaphthalene.[66] An important insight into the mechanism of ribbon formation was found, when Au-organic hybrid polymers were observed that then collapse to the desired GNR at a higher temperature (Figure 1.6C and D). This is in contrast to the previous reports that claim the polymer formation step is carried out by free radicals recombining. However, while Cu- and Ag-organic hybrids are more commonly observed,[67–69] there have only been rare reports of Au-organic hybrids as observed here,[70] so it is currently unclear how general this mechanism is likely to be. An advantage of this particular monomer is that there is no cyclodehydrogenation step

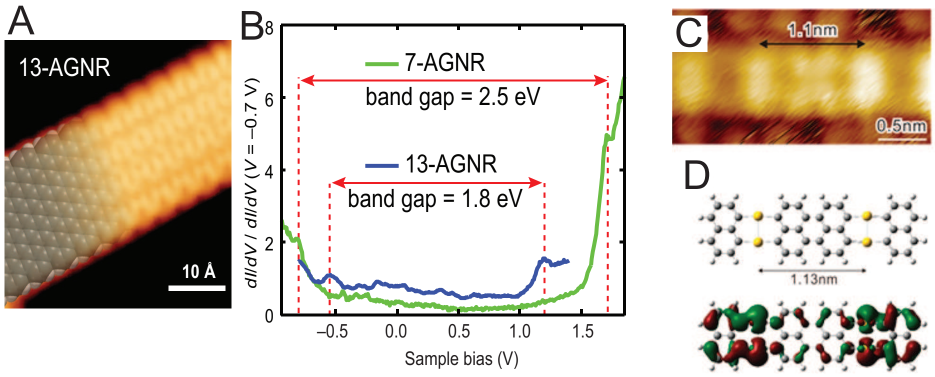

Figure 1.6: A) High resolution STM image of $N = 13$ AGNR on Au(111) with partial model overlay. B) STS of $N = 13$ AGNR compared to $N = 7$ AGNR. [Reproduced from reference[65]] C) High resolution STM image and D) DFT model of Au-organic hybrid polymer precursor to $N = 5$ AGNRs. [Reproduced from reference[66]]

required, thus allowing for milder temperatures to be used.

In addition to synthesizing AGNRs of different widths, surface assisted synthesis has been used to generate ribbons of varying edge construction, including chevron[64] and zig-zag (Figure 1.7).[71] ZGNRs are of particular interest due to the predicted spin-polarized edge states. This study produced ZGNRs of $\sim$ 50nm, paving the way for future research on the unique edge magnetic properties. The authors find that when the ZGNRs are directly on the Au surface, no edge states are observed due to strong interaction of the ribbon with the metal surface. However, when the ribbons are dragged onto islands of insulating NaCl, they become electronically decoupled from the surface, allowing for the observation of two different electronic edge states.

Further tuning of the electronic structure of GNRs beyond width and edge structure modifications has been accomplished through the site selective replacement of carbon atoms with heteroatom dopants, including N,[75–78] B,[72,73,79] and S (Figure 1.8).[74] The synthesis and characterization of chevron type GNRs incorporating 1,[76] 2,[76,77] and 4[78] nitrogen atoms replacing edge carbon atoms has shown that the effect of incorporating a pyridine-like nitrogen with the lone pair orthogonal to the π-system of the ribbon is to rigidly realign the bandgap to lower energies via inductive effects. This is in contrast to the cases where B atoms were incorporated in the center of the ribbon, with the empty p-orbital in conjugation with the π-system.[72,73,79] In this case, an effect more analogous to traditional semiconductor doping is observed, where new electronic dopant states are introduced into the bandgap.

More advanced modulation of GNR electronic structure has been accomplished through the fabrication of GNR heterostructures where a single ribbon contains varying size or dopant profiles along its axis. Heterostructures thus far reported include an all carbon type-I heterojunction made by copolymerizing monomers used for $N = 7$ and $N = 13$ AGNRs (Figure

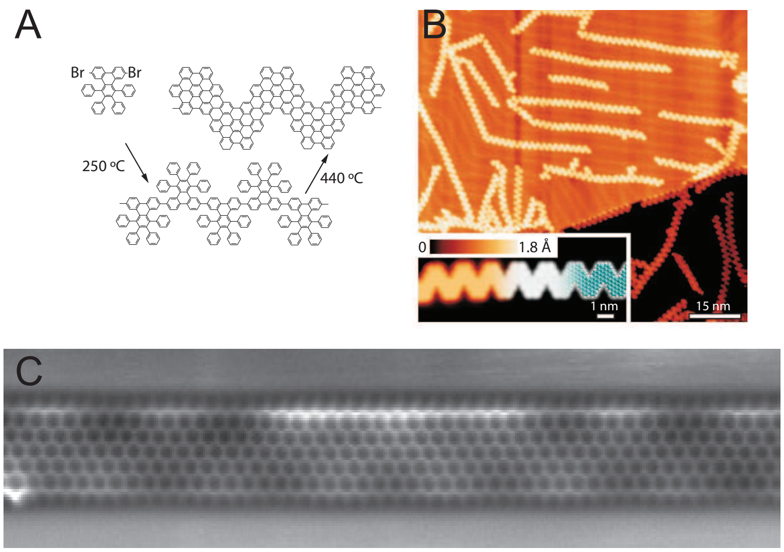

Figure 1.7: A) Chevron type GNR monomer and on surface synthesis and B)High resolution STM. [Reproduced from reference[64]] C) Atomic resoluion non-contact AFM of ZGNRs on Au(111).[Reproduced from reference[71]]

1.9A),[80] a type-II heterojunction made by combining chevron monomers of varied nitrogen incorporation (Figure 1.9B),[78] chevron type GNRs with interspersed electron rich and electron deficient heterocycles made from a single monomer with a divergent on-surface rearrangement,[75] and an embedded quantum dot system by copolymerization of $N = 7$ and B-doped $N = 7$ monomers.[79] Similar to the penetration of end states ~ 30Å into the ribbon noted previously,[65] it was observed through STS that in the case of the type-II heterojunction the band bending between segments occurs over a short distance (Figure 1.9B), being complete after ~ 2 nm, reaching the bulk electronic structure only one monomer away from the junction.[78] This sharp interface should lead to an electrostatic field about 2 orders of magnitude greater than in a traditional semiconductor $p-n$ junction which one would expect to lead to higher charge carrier separation efficiency in photovoltaic systems.

Solution Phase Bottom-Up Synthesis of GNRs

While surface assisted synthesis of GNRs gives access to atomically defined structural characterization and in depth single ribbon electronic characterization, solution phase synthesis of GNRs has the advantage of bulk production and does not require a metal surface, making it ideal for device fabrication. A notable disadvantage of solution phase processing of GNRs is the tendency to form large π-stacked aggregates, that need to be disrupted to perform any single ribbon characterization or device fabrication. As such, solution synthesized GNRs will commonly have alkyl side chains regularly decorating the periphery of the ribbon

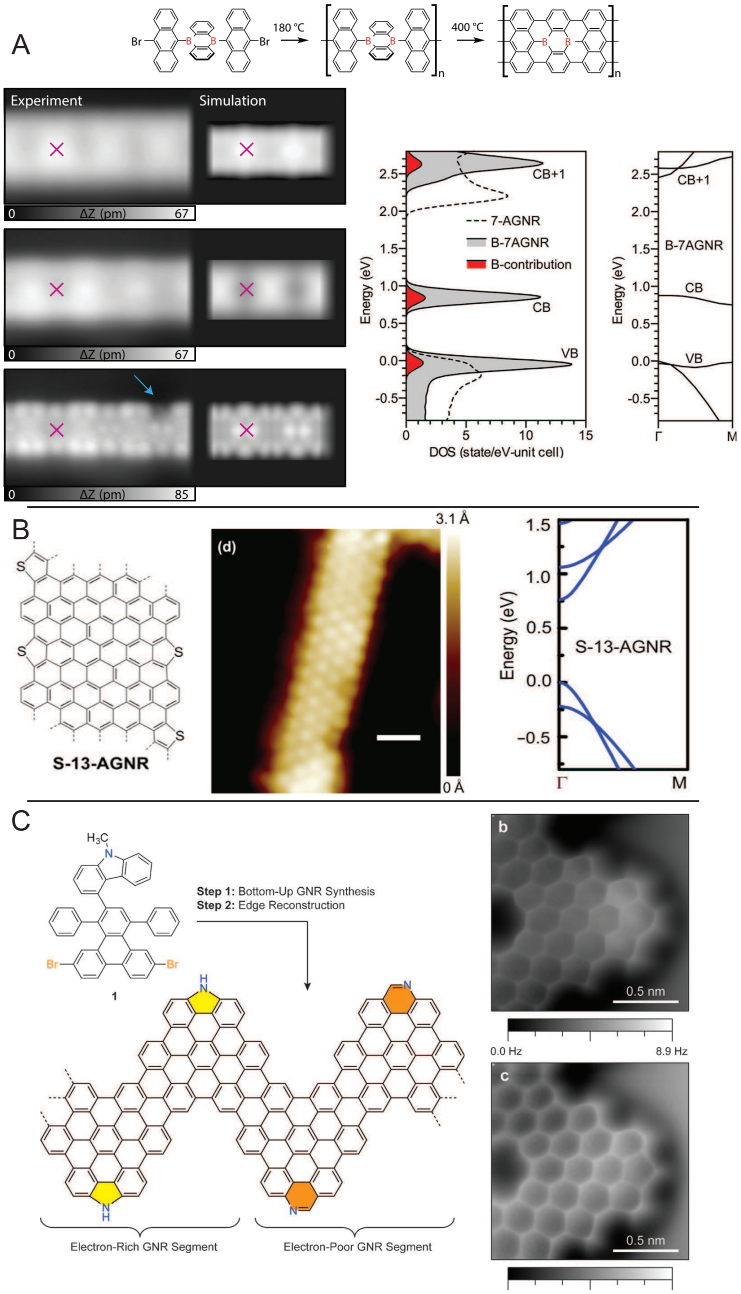

Figure 1.8: A) B atom dopants in $N = 7$ AGNRs produce localized mid-gap dopant states in the electronic structure. [Reproduced from references[72,73]] B) S doped GNR STM and calculated electronic structure. [Reproduced from reference[74]] C) Divergent N doping of chevron GNRs through a common precursor. [Reproduced from reference[75]]

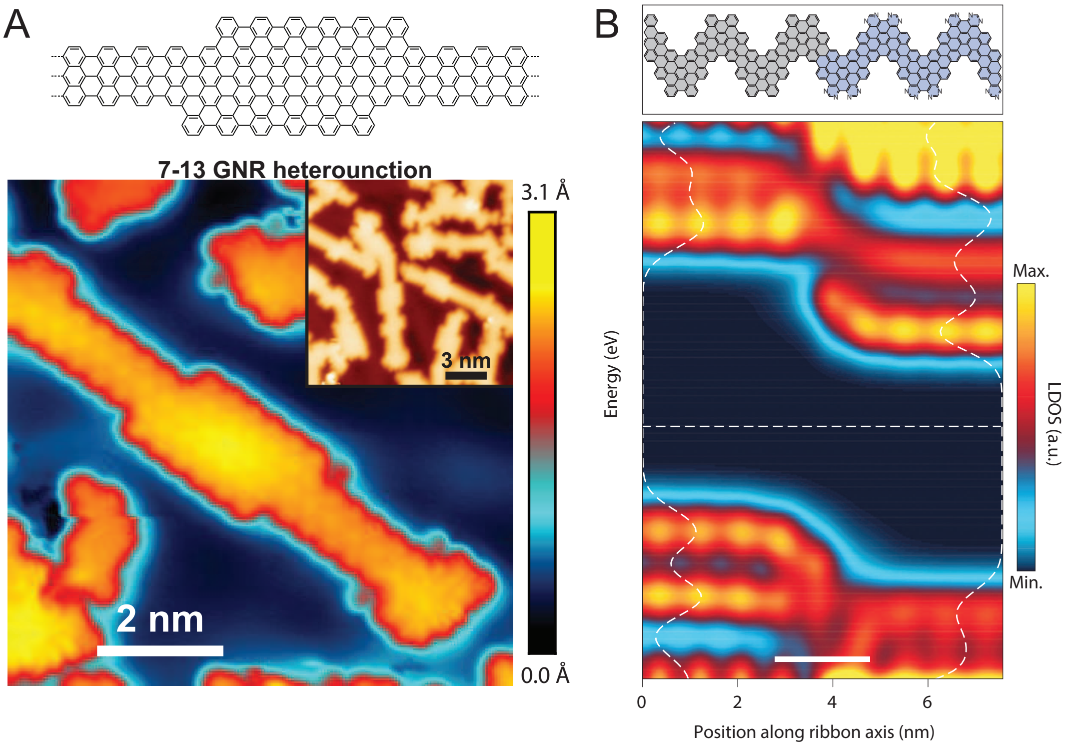

Figure 1.9: A) A type-I heterojunction made by fusing $N = 7$ and 13 AGNRs. [Reproduced from reference[80]] B) A type-II heterojunction made by combining chevron GNRs of different N doping and the observed sharp band bending. [Reproduced from reference[78]]

to interfere with ribbon-ribbon packing and allow for greater solution dispersability. Precursor polymers are formed through a variety of polymerization reactions including Suzuki copolymerization,[81,82] Yamamoto,[83–86] and Diels-Alder polymerization.[87,88]

Both 9-[81] and 18-AGNRs[83] have been synthesized in solution. Suzuki co-polymerization of appropriate monomers yielded the $N = 9$ AGNR precursor polymer with lengths of about 12 nm (Figure 1.10A). This polymerization has been found to suffer in length due to the extreme steric crowding around the reactive sites. By switching instead to a nickel mediated AA type Yamamoto homopolymerization, significantly longer precursor polymers were obtained for the $N = 18$ AGNRs (Figure 1.10B). In both cases, the precursor polymers were converted to the desired GNRs by $FeCl_3$ mediated Scholl reaction, which cyclodehydrogenates the polymers, graphitizing the material.

Chevron GNRs are also available via solution phase synthesis. Unique to chevron GNRs, the same monomer that is used in UHV on surface synthesis can be used in solution by utilizing the Yamamoto polymerization.[85,86] This has allowed for the production of gram quantities of chevron GNR, as well as the measurement of the optical band gap (1.33 eV). Scanning probe microscopy of samples prepared by dropcasting a suspension of the GNRs

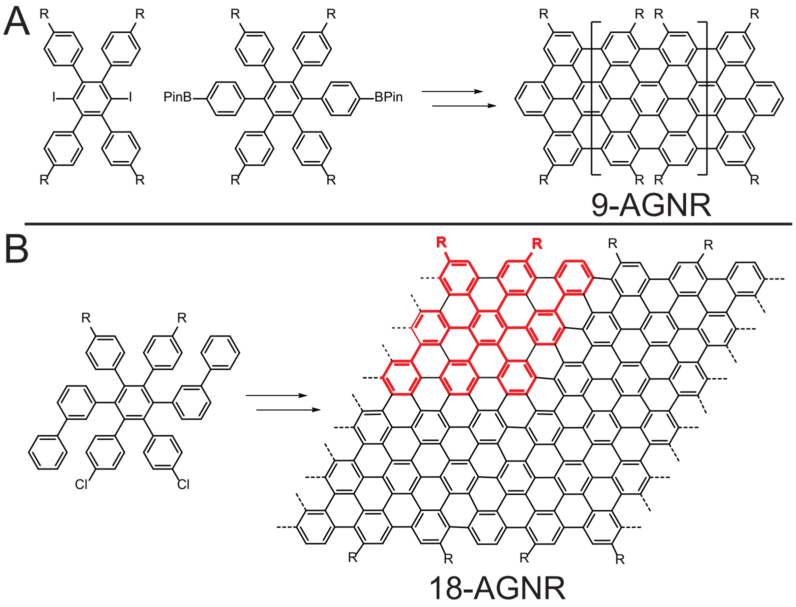

Figure 1.10: A) 9-AGNRs synthesized in solution by first palladium catalyzed Suzuki polymerization, followed by $FeCl_3$ mediated cyclodehydrogenation. R is a solublizing branched alkyl chain.[81] B) 18-AGNRs synthesized by first nickel mediated Yamamoto polymerization, followed by $FeCl_3$ mediated cyclodehydrogenation with one monomer unit highlighted in red for clarity. R=$C_{12}H_{25}$.[83]

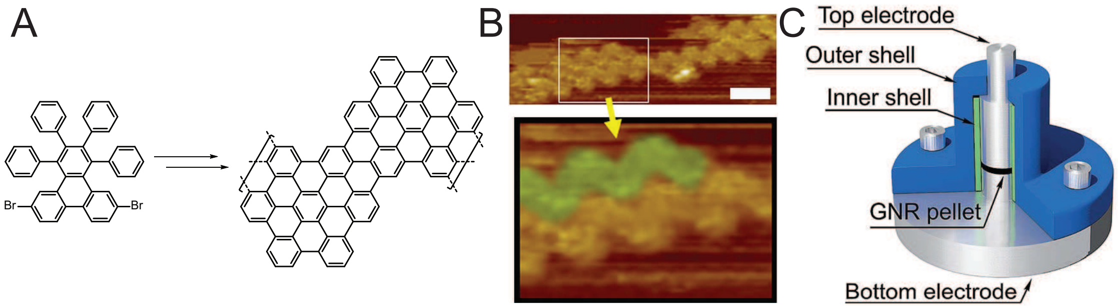

Figure 1.11: A) Solution synthesize of chevron GNRs by first nickel mediated Yamamoto polymerization followed by $FeCl_3$ mediated cyclodehydrogenation. B) STM image of chevron GNRs synthesized in solution and dropcast onto Au(111) showing preferred side-by-side alignment with one ribbon highlighted in green for clarity. [Reproduced from reference[86]] C) Experimental setup for measuring bulk conductance of chevron GNR powder compressed into a disk. [Reproduced from reference[85]]

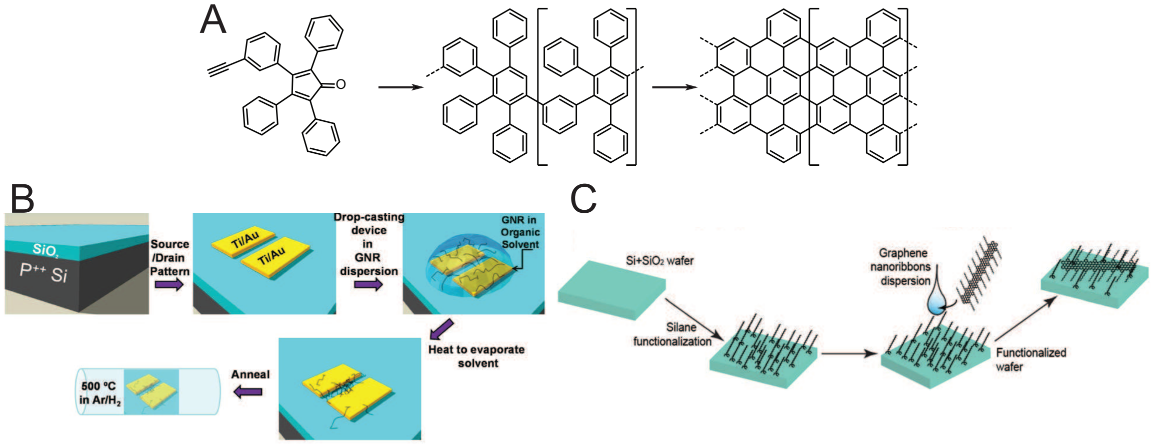

Figure 1.12: A) Schematic synthesis of cove-type GNRs via polymerization of a heteroditopic cyclopentadienone monomer and cyclodehydrogenation. B) Dropcasting a dispersion of cove GNRs onto prepatterned electrodes for a thin film device. [Reproduced from reference[89]] C) Hydrophobic surface functionalization of Si surfaces to tune single ribbon deposition density. [Reproduced from reference[90]]

in organic solvent reveal that ribbons, as when synthesized on surface, tend to have a preferential side-by-side alignment. Bulk conductivity measurements on a pellet of chevron GNRs between cylindrical aluminum contacts give values of $\sim 30\ \mu$A at ± 5 V.[85] This evidence of bulk conductivity is promising for future electronic applications, but does not indicate the conductivity of single ribbons and likely suffers from defects, such as inefficient ribbon-to-ribbon junctions and low packing density.

An edge structure that is more readily available from solution synthesis than on surfaces is the cove type GNR.[87,89–91] The polymer precursors for these ribbons are synthesized by using a heterobifunctional monomer that contains both a terminal alkyne and cyclopentadienone that undergo a thermal Diels-Alder cycloaddition followed by cheletropic extrusion of CO to yield new benzene rings (see Figure 1.12A). Because this reactivity is not known on metal surfaces, this method of producing cove-type GNRs is currently unique to the solution phase, preventing atomic resolution imaging or single ribbon spectroscopy. However, do to the ability to include long and/or branched alkyl chains regularly along the periphery of the ribbon, their solution processability is significantly higher than that of other ribbons. This development has allowed for characterization of charge carrier mobility by THz spectroscopy,[87,91] and has prompted studies on the most effective ways of depositing ribbons onto insulating surfaces both isolated and as thin films (Figure 1.12B and C).[89,90]

Starting Material	Method	Edge Control	Width	Scale	Defects
Graphite	Sonication	No	10–80 nm	multigram	yes
CNTs	Lasers	No	60 nm	Small	Vacancies
	Chemical Oxidation	No	80–120 nm	> 10 g	Oxidation, adsorbed ions
	Hydrogenation	No	2–10 nm	Multigram	Hydrogenation
	Electrochemical	No	70–110 nm	Multigram	Oxidation
Graphene	H_2 Plasma	No	> 10 nm	Wafer	Hydrogenation
	EBL	No	> 25 nm	Wafer	Edge disorder
	Reactive Ion	No	> 10 nm	Wafer	Vacancies
	O_2 Plasma	No	6–20 nm	Wafer	Oxidation
Small Molecules	Solution	Yes	< 2 nm	Multigram	None
	Surface	Yes	< 2 nm	Monolayer	None

Table 1.1: Summary of GNR synthetic methods.

Applications of Bottom-Up Synthesized GNRs

Once GNRs have been synthesized, there arises the further challenge of incorporating a single atom thick, 1 nm wide material into an electronic device. Among the primary issues associated with using surface synthesized GNRs is the need to transfer them from the metal surface to an insulating substrate such as SiO_2 or Al_2O_3, as well as the random alignment of the transfered ribbons. Devices fabrication using solution synthesized GNRs is likewise complicated by the need to overcome the strong $\pi-$stacking between ribbons to isolate and manipulate a single ribbon, guide its placement onto the substrate, and make contact with it.

The first reported use of bottom-up synthesized GNRs in a functioning FET made use of $N = 7$ AGNRs synthesized on a Au(111) surface.[92] The transfer process involved first coating the GNR on Au on mica stack with poly(methyl methacrylate) (PMMA), then delaminating the mica with an aqueous solution of 40% HF an removal of the gold with a gold etchant to leave GNRs on PMMA (Figure 1.13A). This was pressed onto a target SiO_2 on Si substrate and the PMMA was washed away with acetone and Pd contacts were fabricated onto the surface to yield a device shown schematically in Figure 1.13B. Raman spectroscopy was used to confirm the presence of GNRs on the substrate, however no further techniques were used to locate individual GNRs and, as such, the GNRs are arranged randomly under the contacts. This fact, along with the length of the ribbons (average 10–15 nm, up to 40 nm) being shorter than the contact channel length (20–30 nm), led to a low device yield. After annealing the devices under vacuum (300 °C, 3×10^{-7} Torr) to remove adsorbed oxygen and water, they show impressive I_{on}/I_{off} ratios of 3.6×10^3 at a source-drain voltage of $V_{sd} = 1$ V. However, transport through the device was dominated by Schottky junction contacts due in part to band alignment between the GNR and Pd, and in part to the short contact overlap

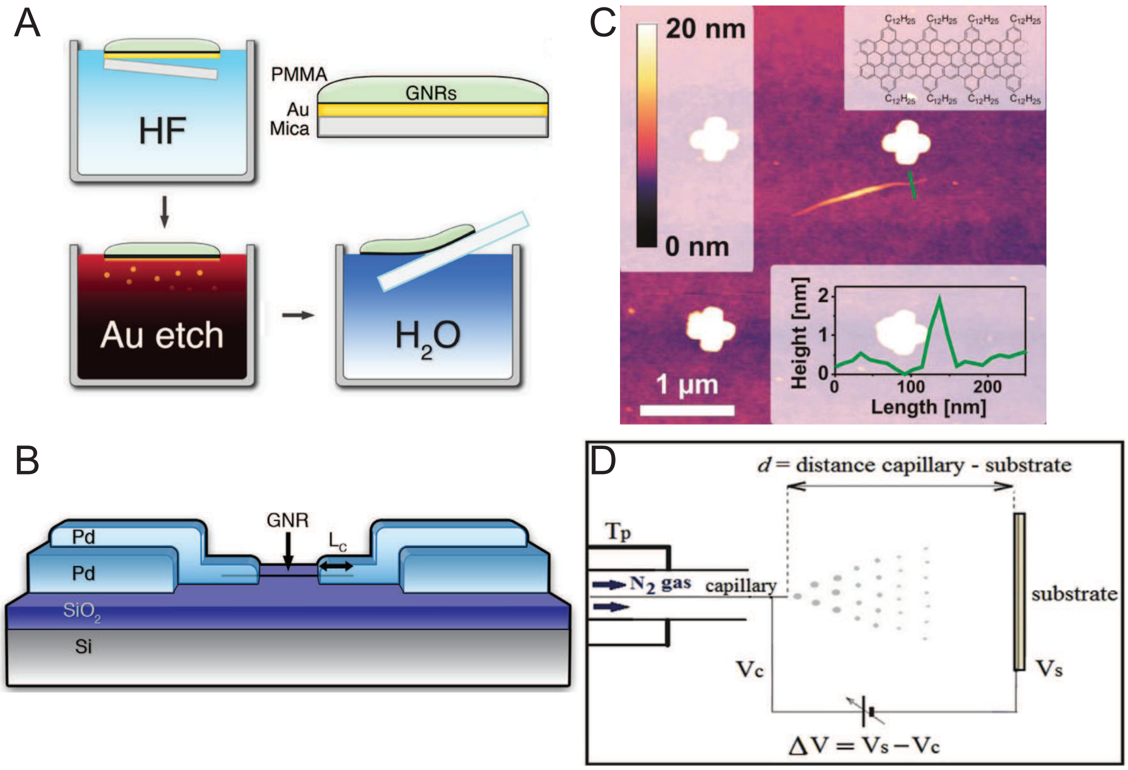

Figure 1.13: Methods of fabricating FETs from bottom-up synthesized GNRs include A) a wet transfer method off of Au on mica films for surface synthesized GNRs. B) A representative GNR FET schematic. [Reproduced from reference[92]] C) submersion of a SiO_2 surface with a hydrophobic SAM in a dispersion of GNRs with prepatterned markers used to locate GNRs during contact deposition. [Reproduced from reference[93]] D) electrospray deposition of a GNR dispersion to form a thin film on graphite electrodes. [Reproduced from reference[94]]

limiting charge injection.

Solution synthesized GNRs were integrated into a transistor two years later, when highly dispersible alkylated cove-type GNRs with a nominal length of $\sim$ 600 nm were deposited on an Al_2O_3 based substrate and contacted with Ti/AuPd electrodes.[93] In this case, the GNRs were suspended in an aqueous dispersion using 1% sodium dodecylsulfate (SDS) as a surfactant and the substrate (8 nm Al_2O_3 on 100 nm SiO_2 on doped silicon) was capped with a monolayer of tetradeecyl phosphonic acid before submersion in the GNR dispersion. The GNRs were then located using AFM with reference to prepatterned markers on the surface (shown in Figure 1.13C) and contacted with the Ti/AuPd electrodes with 100 nm channel length. While the authors claim that in their case the current is not limited by the metal contact junction, their I_{on}/I_{off} ratio suffers greatly when compared to the previous report, reaching only $I_{on}/I_{off} = 2$ with I_{on} up to 70 μA. The authors acknowledge that the low I_{on}/I_{off} ratio could be due to having contacted not one ribbon, but several in a bundle, which their calculations show could lower the band gap to as low as 30% of a single GNR.

A very different approach to solution phase GNR device fabrication designed to yield a transistor not consisting of a single ribbon, but of a thin film yielded devices with slightly better I_{on}/I_{off} up to 5, but only by reducing I_{on} to the nA range and at the very high V_G =40 V.[94] While the GNRs used both in this report and in the previous are the same, the fabrication methods are quite unique. Here, the authors prepattern graphite electrodes on a SiO_2 substrate and form a film of GNRs in the channel by an electrospray deposition method from a dispersion in THF/MeCN (Figure 1.13D). This results in the need for significant amounts of inter-ribbon charge transport, the inefficiency of which could be partially to blame for the low current passing through the device.

GNRs have also been used in chemical sensing applications. By dropcasting a thin film of cove GNRs from suspension onto prepatterned Ti/Au electrodes and annealing the device to 500 °C to thermally remove alkyl chains and improve ribbon-ribbon contact, a sensor that shows conductivity change on exposure to NO_2 was made that is sensitive down to 50 ppb.[89]

An alternative use of GNRs is not to use them as active device materials on their own, but to use them combined with another active material. Poly(3-hexylthiophene-2,5-diyl) (P3HT) is a conductive polymer commonly used in the development of organic field effect transistors (OFETs), among other organic electronic applications. By creating a blend of solution synthesized $N = 18$ AGNRs and P3HT, researchers were able to improve the charge carrier mobility by a factor of three over a pure P3HT device without sacrificing high I_{on}/I_{off} as happens when a similar blend is made with sheet graphene or CNTs instead.[83] The resultant device was also functional as an organic phototransistor (OPT) with increased photoresponse.

Characterization of GNRs by Raman Spectroscopy

While microscopies that provide atomic resolution imaging of GNRs (AFM, STM) are extremely valuable characterization tools, they are not immediately viable in many scenarios and do not provide any information on the electronic or vibronic nature of the materials. A spectroscopic technique that has become one of the most valuable and ubiquitous in the GNR literature is Raman spectroscopy.

Raman spectroscopy is a type of vibrational spectroscopy whereby the energies of vibrational modes in a molecule are probed by scattering light from the sample. Characterization by Raman spectroscopy has become a staple technique for all graphitic materials, including graphene, graphite, CNTs, and GNRs due to the ability to acquire information about phonons, electron-phonon, magneto-phonon, and electron-electron interactions, as well as strain, doping, disorder, and fucntional groups.[95] Vibrational characterization is particularly important in conjunction with optical and electronic characterization in graphitic systems, due to the strong electron-phonon coupling in graphene.[96]

A monochromatic laser is used to illuminate the sample with energy, typically below the energy of an electronic excitation, to a virtual excited state. In the majority of cases, this virtual excited state relaxes to its original ground state and emits a photon with the same wavelength as the incident photon. This elastic scattering is referred to as Rayleigh scattering. However, about $10^{-5}\%$ of the incident photons are scattered inelastically in a process referred to as Raman scattering. In this case, the virtual excited state relaxes not to the ground state, but to a vibrationally excited state due to interaction of the photon with the polarizability elipsoid of a vibrating molecule. This relaxation results in the emission of a photon of lower energy than the incident photon. All of the scattered light is detected and plotted as a difference in incident and detected light with the Raman shift defined as in Equation 1.1. This sets the elastically scattered light to 0 cm^{-1} and makes the resultant spectrum independent of excitation wavelength.

$$\bar{\nu} = \frac{1}{\lambda_{incident}} - \frac{1}{\lambda_{scattered}} \tag{1.1}$$

The first order Raman spectrum of graphitic materials is dominated by two signals resulting from in-plane vibrations.[97] The G peak ($\approx$1600 cm^{-1})corresponds to the primary transverse- and longitudinal-optical modes (TO and LO respectively) seen in Figure 1.14. In graphene these modes are degenerate, thus resulting in a single sharp peak. However, this is not the case in CNTs where the two modes are inequivalent resulting in a split G peak, or in GNRs where only one G peak is observed due to one of the two modes being inactive in backscattering depending on the edge chirality of the ribbon.[98 99] This makes the G peak a particularly diagnostic feature when distinguishing between allotropes.

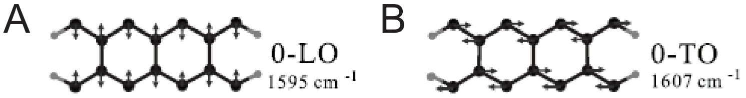

Figure 1.14: Primary in plane lateral (A) and transverse (B) optical vibrational modes in graphene. [Reproduced from reference[100]]

The other primary first order feature in the Raman spectrum of graphitic materials is the D peak, appearing around 1300 cm^{-1}. This is due to an in-plane double resonance where the electron is elastically scattered off of a lattice defect.[101] Because a lattice defect is necessary for this peak, it is not present in pristine single layer graphene. However, in GNRs it is multicomponent due again to the inequivalence of the TO and LO phonons.[99] Because the two primary subcomponents of the D peak show different responses at different λ_{ex}, it can appear as either broadened or bifurcated depending on instrument resolution and excitation wavelength.[102]

Finally, in the higher wavenumber region, primarily for GNRs and large PAHs, we have the overtone and combination peaks. The first is a broad feature around 2600 cm^{-1} corresponding to the 2D and D_j+D_k resonances. This multicomponent peak is the result of multiphonon processes combining the aforementioned D peak components. Around 2900 cm^{-1} is the D+G peak, a bifurcated peak arrising from multiphonon interactions between the G and D peak subcomponents. Finally, the sharper 2G resonance appears around 3200 cm^{-1}. In defective graphene, similar features can be seen that instead result from interaction with the D' peak not generally observed in GNRs.

1.3 Conclusion

Due to the extensive limitations of top-down methodology and the inherent advantages of bottom-up synthesis of GNRs, future GNR based technologies must be based on bottom-up synthesized GNRs to ensure quality and reproducibility. As such, new synthetic methods are required to expand the library of GNRs available through bottom-up synthesis. The remainder of this dissertation will focus on the synthesis and characterization of novel GNRs and GNR-heterostructures (requisite for the development of advanced device architectures), as well explore novel applications of bottom-up synthesized GNRs.

Chapter 2

Synthesis of Novel Armchair GNRs by Surface Assisted Synthesis

In this chapter the syntheses of novel organic small molecule precursors to graphene nanoribbons are shown. The on-surface behaviors of the precursors are then characterized using high resolution scanning tunneling and non-contact atomic force microscopies. Electronic structure calculations performed using density functional theory in the Quantum Espresso package are provided for two of the ribbons explored in this chapter.

2.1 $N = 9$ Armchair GNR and Derivatives

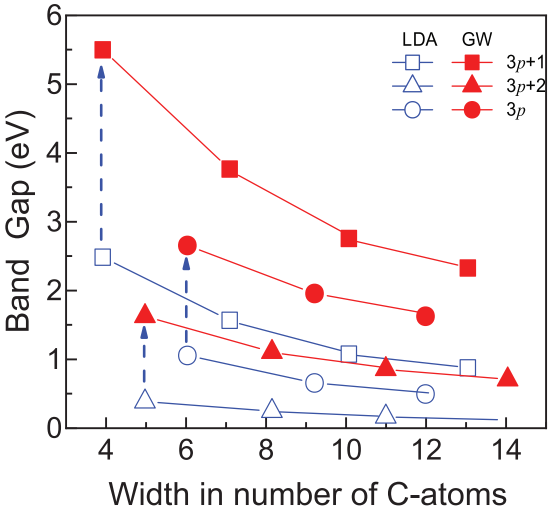

Figure 2.1: LDA and GW predictions of AGNR bandgap dependence on width of ribbon.[103]

First principles calculations on narrow armchair GNRs calculated at two different levels of theory, in the local density approximation (LDA) and with the GW approximation, predict a non-linear dependence of the bandgap on width of the ribbon. Instead, three distinct families exist with monotonically decreasing bandgap within them (Figure 2.1). In order to confirm the theoretical predictions and tune the bandgap of device materials, it is necessary to develop methods for the synthesis of GNRs that span the possible range of widths.

The first AGNR explored here is the $N = 9$ AGNR, a member of the middle bandgap $N = 3p$ family. To gain a better understanding of the electronic structure of the GNR beyond the published bandgap, first-principles calculations are performed. The synthesis of a novel monomer is then described, followed by characterization of the different methods of graphitization.

Calculations

First-principles calculations of $N = 9$ AGNRs were performed using DFT in the Quantum Espresso package.[104] The pseudopotentials used were norm-conserving with a plane wave energy cutoff of 70 Ry. The structure was relaxed until the force on each atom was smaller than 0.014 eV. The unit cell dimension along the ribbon axis was relaxed, and 20 Å in the two orthogonal directions to avoid ribbon-ribbon interactions. The Gaussian broadening used in plotting the DOS was 0.04 eV. The resultant band structure and density of states (DOS) can be seen in Figure 2.2A and B respectively. The calculated bandgap of 0.675 eV is consistent with calculations performed at the same level of theory,[105] giving credence to

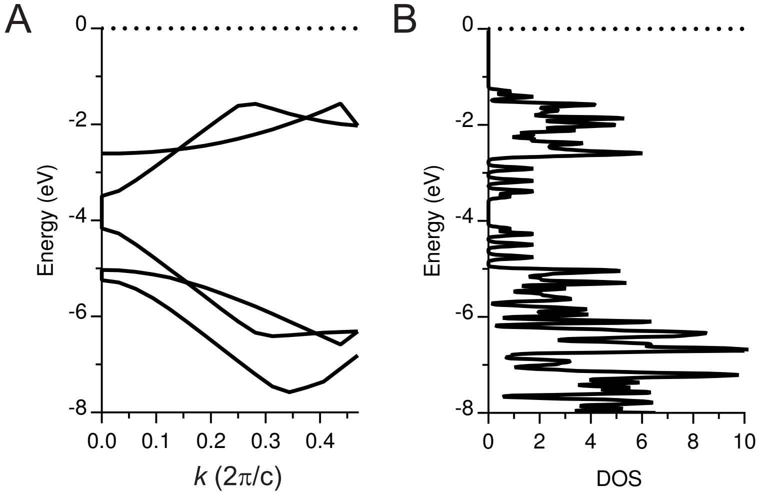

Figure 2.2: A) Band structure with bandgap = 0.675 eV, consistent with previous calculations at the same level of theory,[105] but not calculations utilizing GW correction[103] and B) densities of states of $N = 9$ AGNR.

the validity of the results. In addition to the value of the bandgap, the clear dispersion of the valence and conduction bands indicates facile transport through the ribbon.

Synthesis

The synthesis of diiodosexiphenyl **4** was accomplished in four steps from 4,4'-dinitrobiphenyl as in Scheme 2.1. Selective 2,2' diiodination by first forming a bridged iodonium intermediate with $NaIO_3$ in H_2SO_4, then ring opening with CuI and NaI yielded **1** in 50% yield. Reduction of the nitro groups with $SnCl_2$ under acidic conditions followed by recrystallization from EtOH yielded **5** in 50% yield. Installation of the biphenyl substituents onto the diaminobiphenyl core was accomplished using Suzuki-Miyaura cross coupling, and final installation of the requisite halogens was done using a modified Sandmeyer reaction to yield **4** in 25% yield from **3**.

Surface Characterization

Monomer **4** was sublimed under UHV onto a room temperature Au(111) surface. Initial characterization of **4** on Au(111) (Figure 2.3 A and B) showed amorphous coverage of the surface. An important observation is that even at sub-monolayer coverage of **4**, the molecules tended to form multilayer islands, indicating a preferential adsorption of new monomers onto already deposited monomers instead of onto clean Au(111). Annealing the islands to 150 °C (Figure 2.3C and D) and higher did not lead to any appreciable change in the coverage

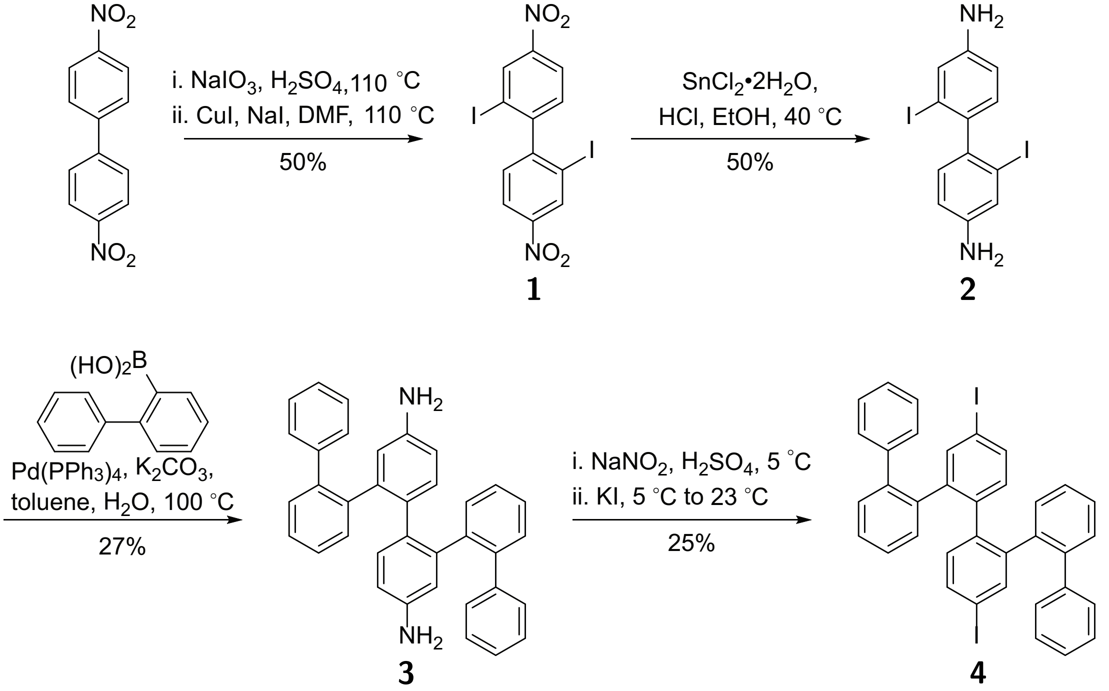

Scheme 2.1: Synthesis of **4**.

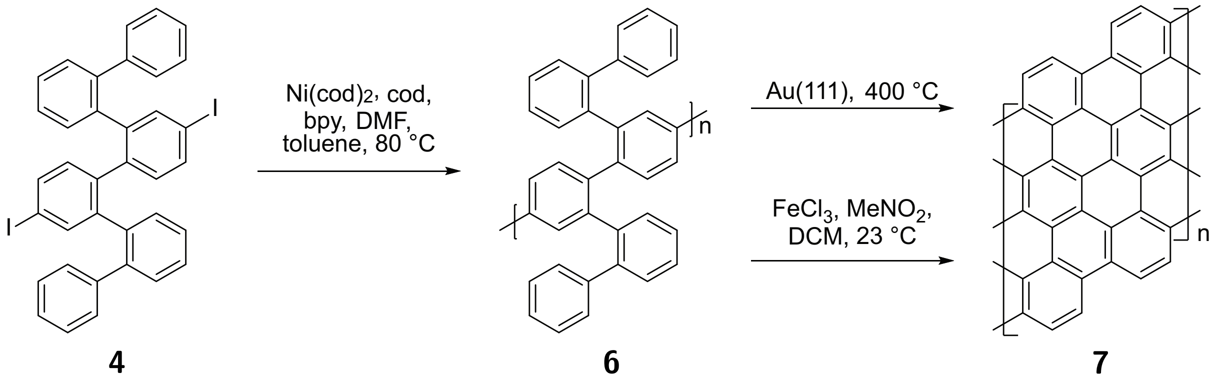

Scheme 2.2: Divergent syntheses of **7**.

or morphology of the sample. We attribute this apparent lack of polymerization to the aforementioned lack of Au-monomer interaction.

In an attempt to circumvent the apparently difficult surface assisted polymerization of **4**, a hybrid route utilizing solution phase polymerization and surface cyclodehydrogenation was devised (Scheme 2.2). The precursor polymer **6** was synthesized in solution by Yamamoto polymerization of **4** with Ni . MALDI-MS of **6** (Figure 2.4B) clearly showed one family of

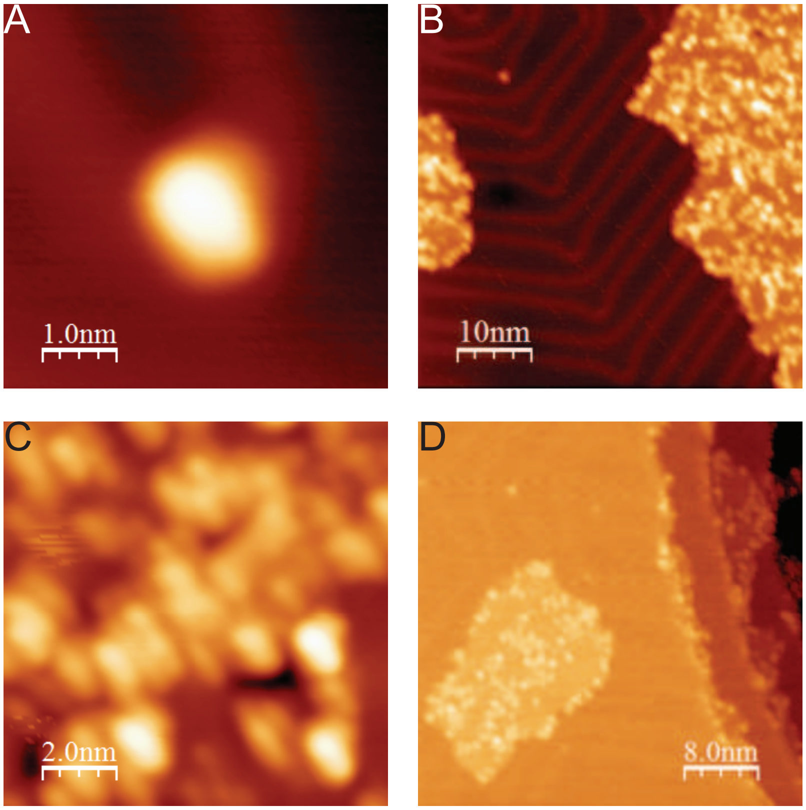

Figure 2.3: A and B) STM images of **4** as deposited on Au(111) at room temperature. C and D) **4** after annealing to 150 °C.

peaks separated by the expected repeat unit (456 D). GPC of the sample produced with these conditions (Figure 2.4A) showed the presence of lower molecular weight oligomers at higher retention time that appear as sharp individual peaks, as well as longer polymers that form a more even distribution.

We then synthesized 9AGNR **7** in two ways. The first is the all solution route, in which the Scholl oxidation with $FeCl_3$ is used. Analysis of this sample by Raman spectroscopy (Figure 2.4D) showed the characteristic D and G peaks, as well as the expected overtones. We then dropcast a solution of **6** in DCM onto a freshly cleaned Au(111) surface, which was rapidly reintroduced to UHV. Annealing the sample to 400 °C both helped remove contaminants introduced by exposing the sample to air, and enabled the surface assisted cyclodehydrogenation to yield 9AGNR **7**. Figure 2.4C shows an STM topography image, wherein several extended structures of uniform height and width consistent with **7** can be readily identified. Performing Raman spectroscopy on this sample and comparing it to the solution prepared sample (Figure 2.4D) showed that the two samples match nicely with regard to peak positioning, with differences arising mostly in the intensity of the higher order peaks and FWHM of the D and G peaks.

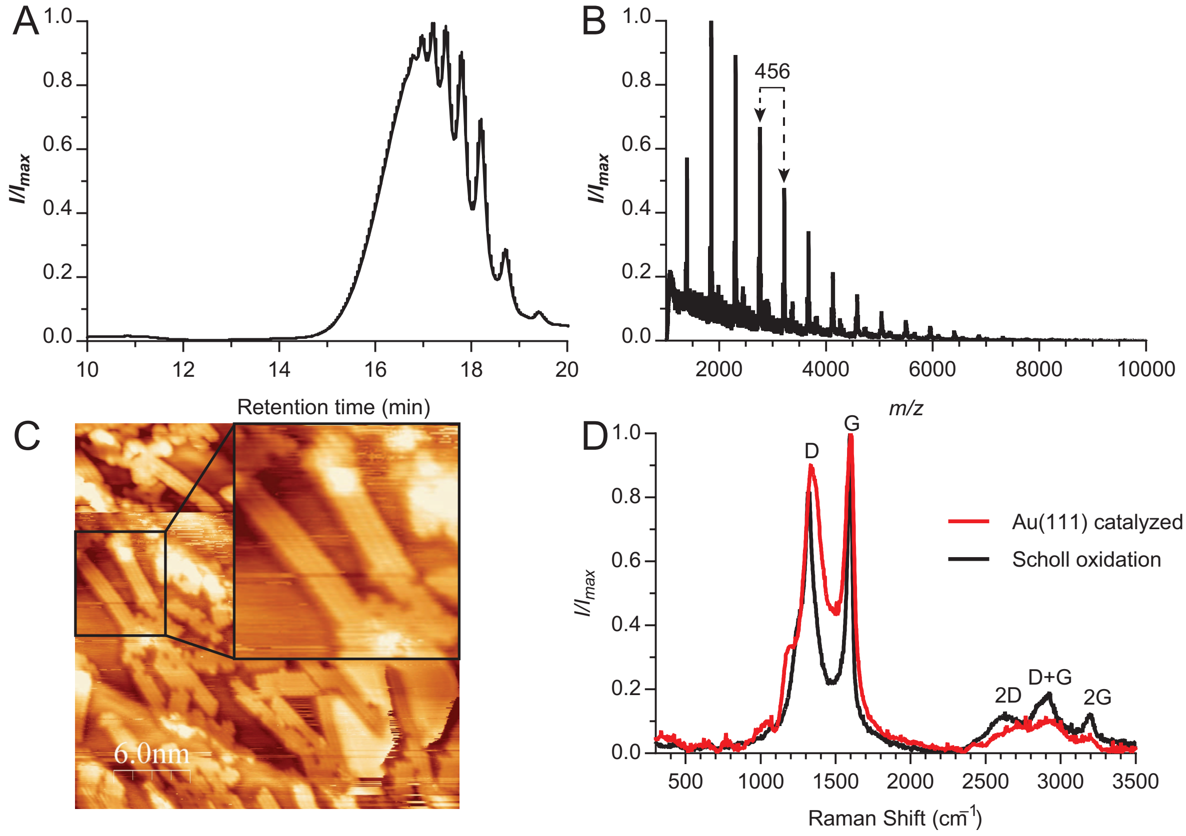

Figure 2.4: A) GPC trace of **6** B) Raman spectrum of **6** C) STM image of $N = 9$ AGNR obtained by dropcasting a solution of **6** in CH_2Cl_2 onto a freshly cleaned Au(111) surface and annealing to 400 °C in UHV, inset: close up of two $N = 9$ AGNRs. B) Raman spectra obtained for **7** prepared both by solution synthesis with the Scholl oxidation and by surface assisted cyclodehydrogenation.

The modularity of the synthesis of $N = 9$ AGNR monomer **4** creates the possibility of generating a variety of different GNRs from monomers that can be made by cross coupling of intermediate **2** with the appropriate substituent instead of biphenyl boronic acid as was used in the synthesis of **4**. Monomers for which synthetic progress has been made are depicted in Figure 2.5. This allows access to GNRs of different width (**8**), edge construction (**9**), doping patterns (**10**, **11**, **12**), and solubility (**13**, R = alkyl). The syntheses of these monomers were stalled at the difficult, highly stericly crowded cross coupling needed to create the full backbone, and at the time of writing require further optimization.

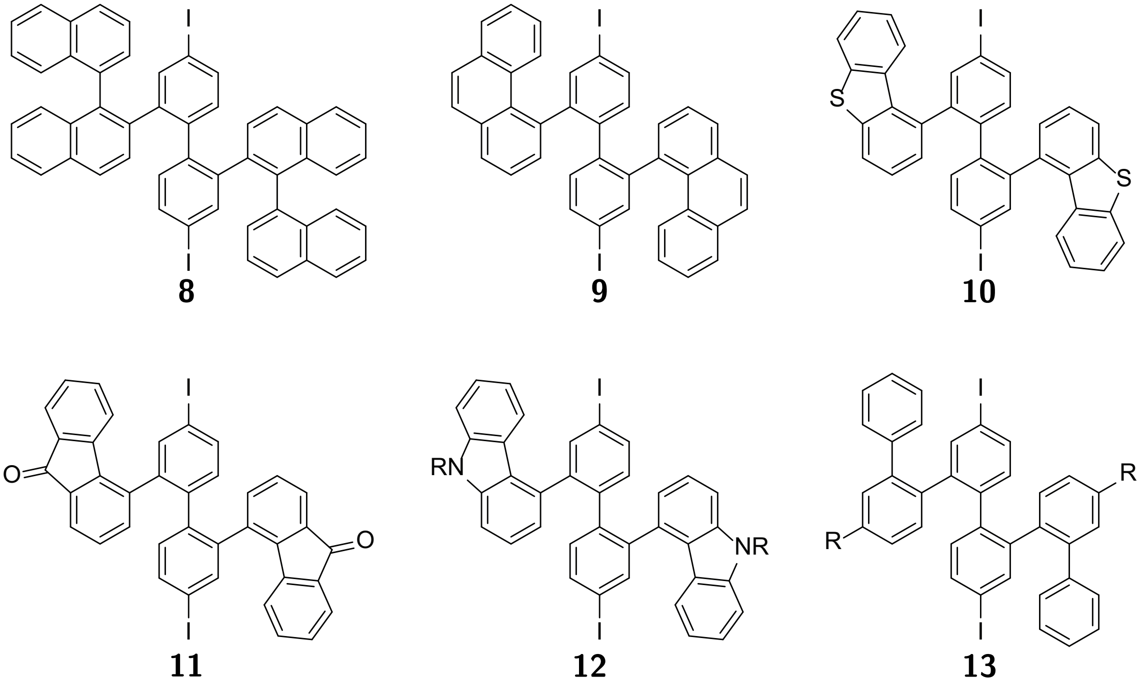

8 **9** **10**

11 **12** **13**

Figure 2.5: Alternative monomers considered to make use of modularity of synthesis for **4**, available via cross coupling of **2** with the appropriate substituent.

2.2 $N = 11$ Armchair GNR

As a member of the lowest predicted bandgap $N = 3p + 2$ family, $N = 11$ AGNR is an attractive target for expanding the available toolbox. To date, only one member of the $3p + 2$ family has been reported,[66] and the bandgap observed by STS was significantly higher than that predicted by first-principles calculations.

Calculations

First-principles calculations of $N = 11$ AGNRs were performed using DFT in the Quantum Espresso package.[104] The pseudopotentials used were norm-conserving with a plane wave energy cutoff of 70 Ry. The structure was relaxed until the force on each atom was smaller than 0.014 eV. The unit cell dimension along the ribbon axis was relaxed, and 20 Åin the two orthogonal directions to avoid ribbon-ribbon interactions. The Gaussian broadening used in plotting the DOS was 0.01 eV.

Synthesis

The synthesis of **20** was accomplished in seven steps from commercially available 1,3-dicyano benzene (Scheme 2.3). The starting material was selectively iodinated by directed ortho

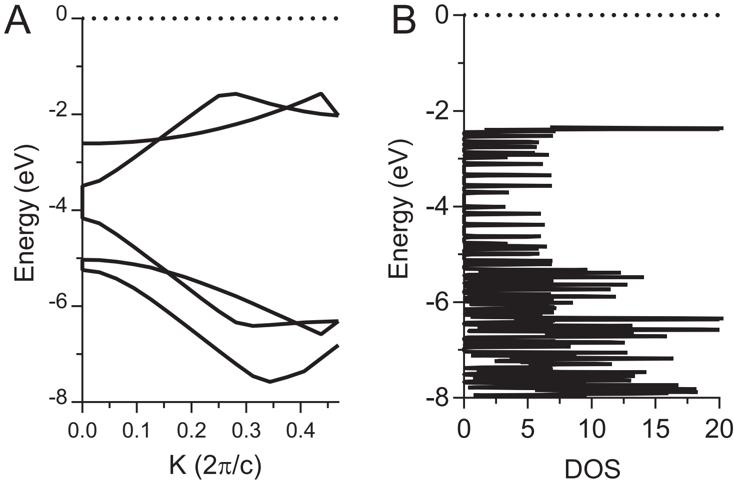

Figure 2.6: A)Band structure and B) DOS of **14**.

metallation using LDA, followed by quenching with I_2 to give **15** in moderate yield, followed by bromination with NBS under acidic conditions to produce **16**. A double reduction of the cyano groups to aldehydes using Raney-Nickel yielded **17**. Ortho-tolyl groups were installed by nucleophilic addition of an *o*-tolyl Grignard reagent to the aldehydes, followed by PCC oxidation of the resulting diol intermediate to give **18** in 94% over two steps. Isolation of the intermediate diols was found to result in lower overall yield. Dimerization of **18** using Ullman coupling was directed both by known increased activity of iodine over bromine, as well as the direction afforded by having electron withdrawing groups ortho to the desired halogen, yielding **19** in good yield. Final cyclization of **19** to produce the desired monomer **20** was accomplished by heating with P_2S_5, which proceeds through the tetrathione analogue of **19**.

Surface Characterization

The results of surface studies of monomer **20** on Au(111) are shown in Figures 2.7 and 2.8. In Figure 2.7 A and B we see that at room temperature, **20** forms well ordered monolayer islands at submonolayer coverage. This is in stark contrast to the formation of amorphous, thick islands formed by **4**. We attribute this to the larger planar π-system present in **20** due to the pyrene core that can interact more strongly with the surface, as well as the decreased flexibility of the monomer, allowing for efficient on-surface packing. We anticipate that this preorganization is likely to positively influence the polymerization. After annealing the sample to 150 °C (Figure 2.7C), we continue to observe the presence of well ordered islands with apparent striations. Annealing to 250 °C results in the breaking up of the islands (Figure 2.7D), leaving isolated extended segments that can be attributed to precursor polymer **21**.

Further annealing of the precursor polymers to 400 °C efficiently planarized the observable

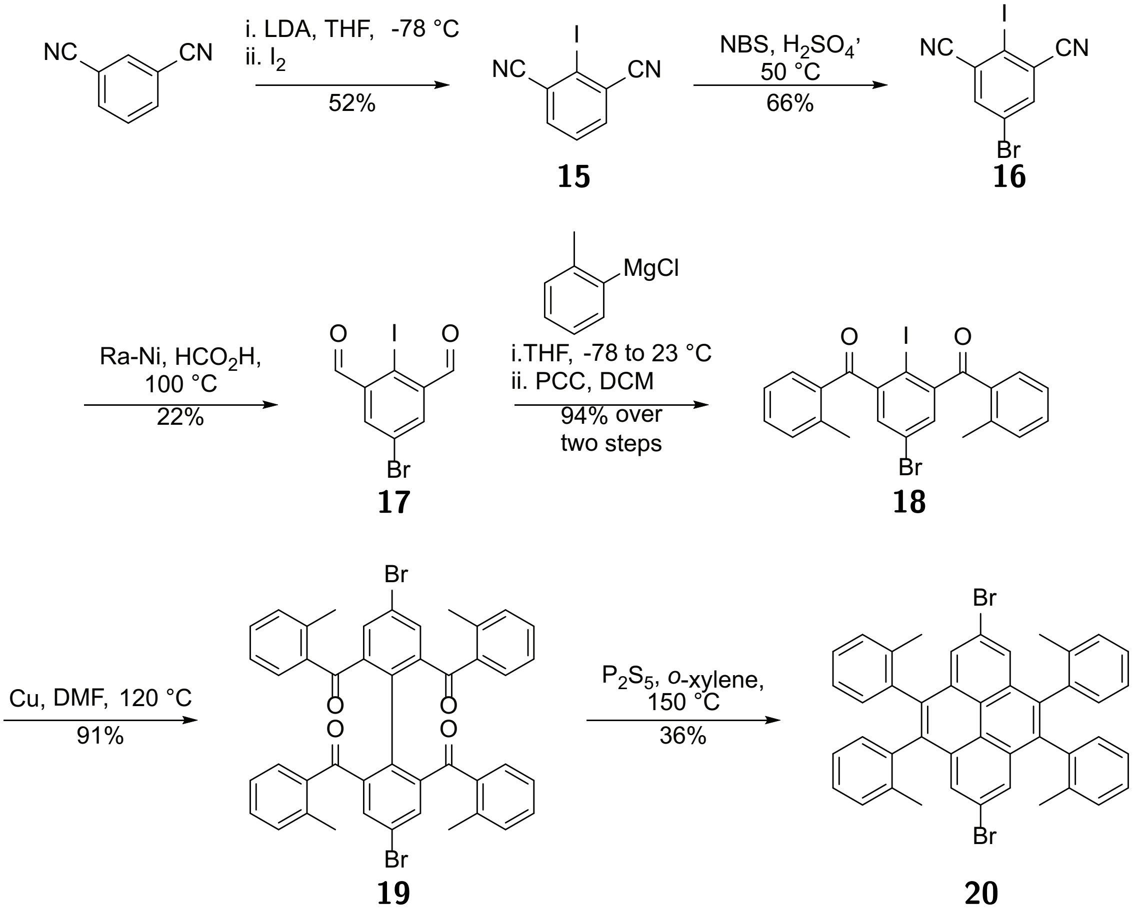

Scheme 2.3: Synthesis of **20**.

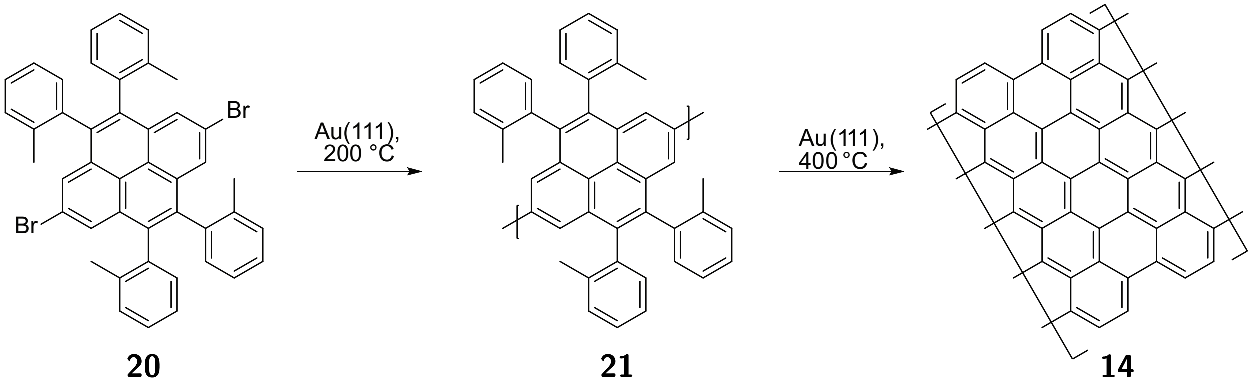

Scheme 2.4: Surface assisted synthesis of **14**.

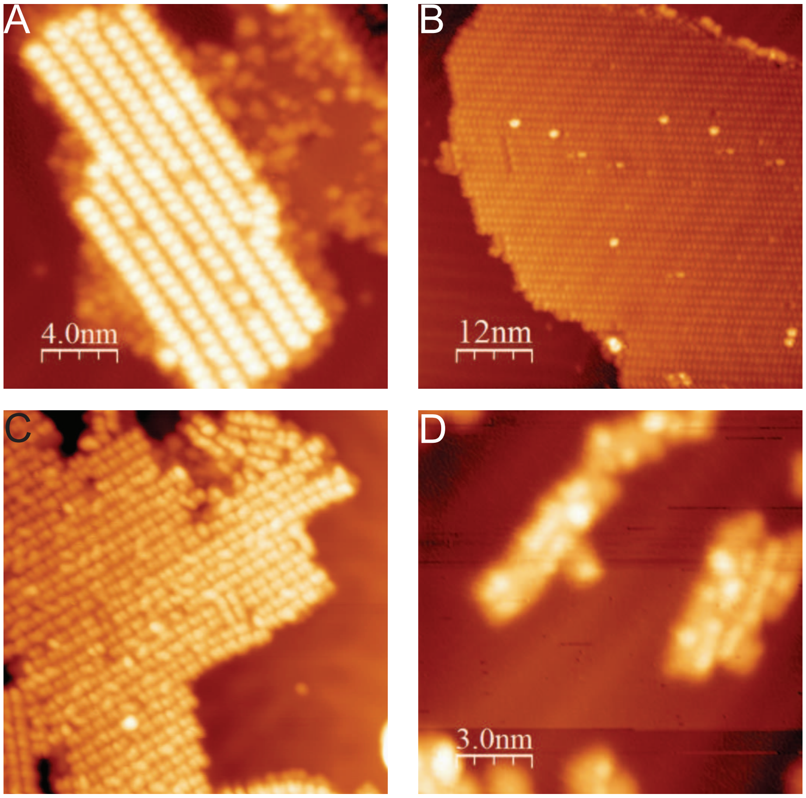

Figure 2.7: STM of **20** as deposited at room temperature on Au(111) (A and B), after annealing to 150 °C (C), and after annealing to 250 °C (D).

features (Figure 2.8). In Figure 2.8A we note the presence of fairly long, planar features of constant width and height consistent with 11AGNR **14**. Zooming in on one such structure as seen in Figure 2.8B reveals that sections of the observed features are indeed the desired GNRs. However, also observable at the end of the shown ribbon are segments that appear to be more defective. Focusing on a section of material that appears to be very defect rich in both STM (Figure 2.8C) and NC-AFM (D) reveals that the defect sites appear to be the result of unwanted side reactivity at the site of the methyl groups.

2.3 N-Doped $N = 7$ Armchair GNR

Syntheses

The synthesis of dibromophenazine **25** was accomplished in three isolated steps (Scheme 2.5). Bromination of benzothiadiazole with NBS under acidic conditions to yield **22**, followed by $NaBH_4$ reduction of the heterocycle yielded diamine **23** in good yield. Condensation of diamine **23** with quinone **24** generated by $K_2Cr_2O_7$ oxidation of catechol yielded the target

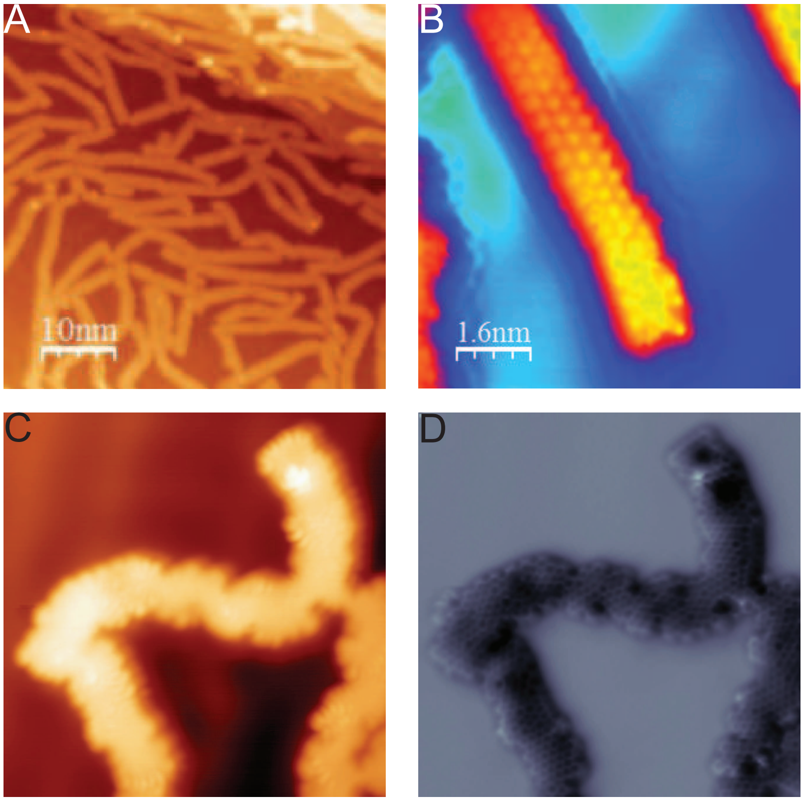

Figure 2.8: STM of **20** after annealing to 400 °C (A-C), and NC-AFM of the same sample (D).

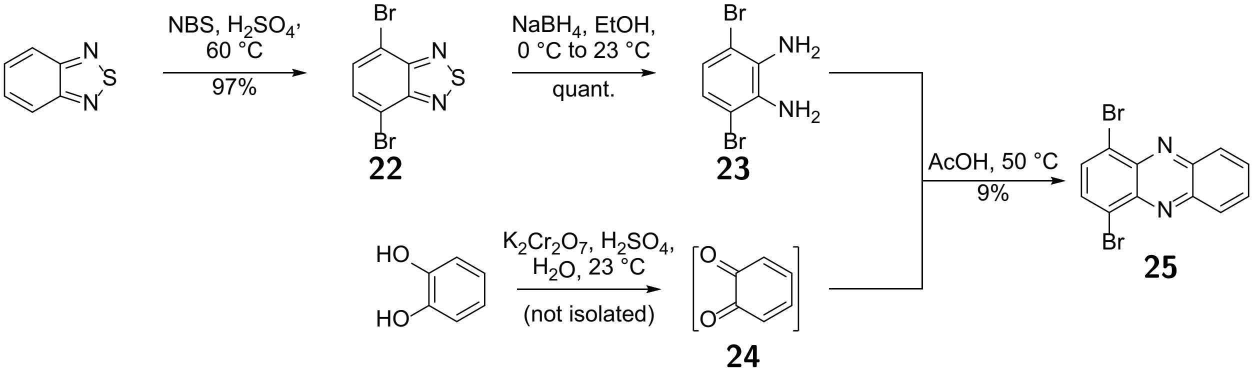

Scheme 2.5: Synthesis of **25**.

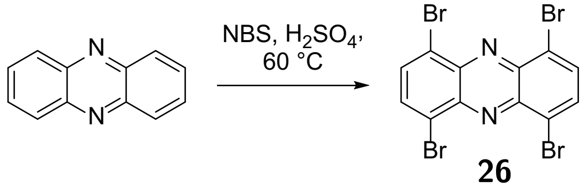

Scheme 2.6: Synthesis of **26**.

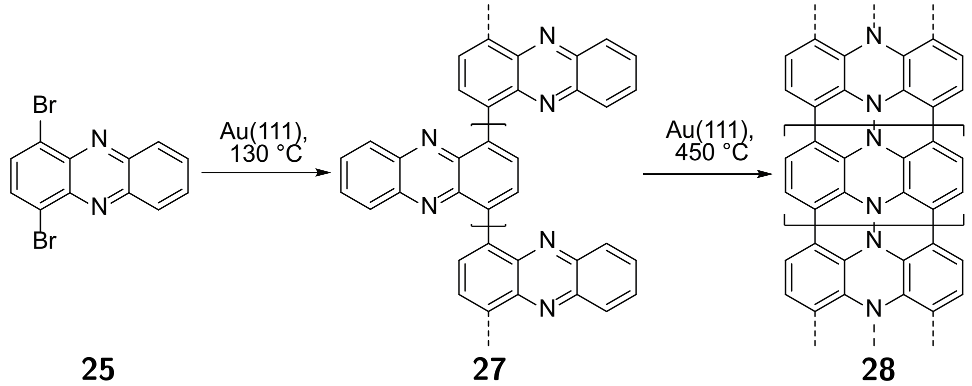

Scheme 2.7: Proposed synthesis of **28**.

25. Tetrabromophenazine **26** was synthesized by extensive bromination of phenazine under acidic conditions.

Surface Characterizations

Sublimation of **25** onto a Au(111) surface at room temperature resulted in the planar, lacy pattern observable in Figure 2.9A and B. Annealing the sample to 130 °C at a rate of 5 °C/min to induce homolytic dehalogenation and polymerization to **27**, followed by further annealing to 450 °C at the same rate to induce graphitization to GNR **28**, yields the structures seen in Figure 2.9C and D. From the larger area scan in Figure 2.9C it is immediately clear that the initial self-assembled structure is gone, replaced by extended high aspect ratio structures as would be expected from successful polymerization. Upon closer inspection (Figure 2.9D), we can see that we do not have the smooth edge structure that would be associated with successful graphitization to GNR **28**, but rather a regularly spaced saw-tooth type structure. We attribute this to precursor polymer **27**, indicating successful polymerization of **25** to **27** without further reaction. This result indicates that the planarity of **27** on Au(111) allows for strong interaction of each subunit with the surface and prevents the necessary rotation of every other unit that would allow for cyclodehydrogenation.

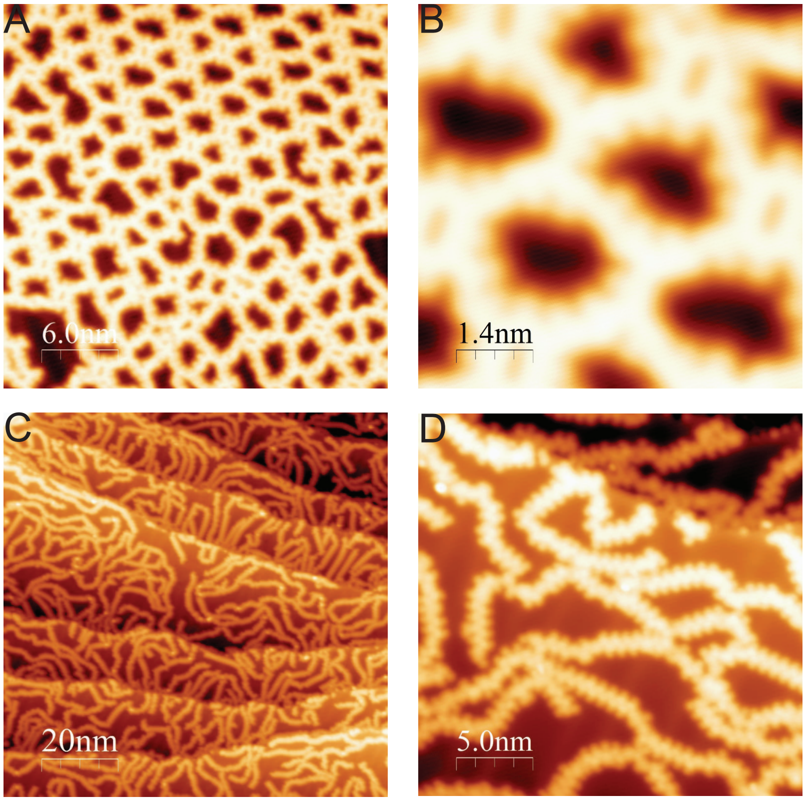

Figure 2.9: A and B) **25** as deposited on a Au(111) surface held at room temperature. C and D) After annealing to 130 °C at a rate of 5 °C/min, holding for 30 min, then ramping again at the same rate to 450 °C and holding for 10 min.

2.4 Heavily N-Doped $N = 7$ Armchair GNR

Synthesis

To further modify the electronic structure of $N = 7$ AGNR, heavily N-doped GNR **31** was designed, expected to be synthesizable from monomer **29**. Polymerization of **29** to yield precursor polymer **30** is expected to occur at temperatures typical of other monomers, <200 °C. However, unique to this case, the final graphitization step required is not a cyclodehydrogenation reaction, but rather a cyclic N-N bond forming reaction along both sides of the polymer. This reactivity is less understood, and as such the temperature required to effect it is currently unknown.

The synthesis of monomer **29** was performed in five steps from previously synthesized dibromobenzothiadiazole **22**. First, dinitration with fuming nitric acid in triflic acid gave **32**. Attempts to perform complete reduction of both nitro groups as well as the thiadiazole ring with Zn in AcOH to produce the free tetraamine and condensation with glyoxal to yield

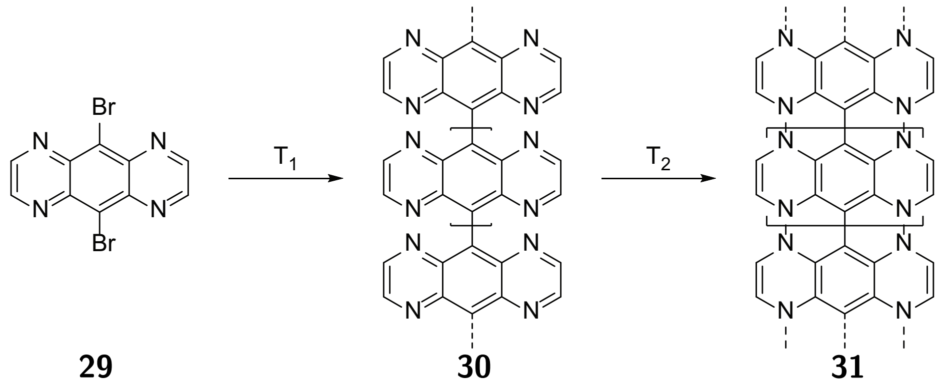

Scheme 2.8: Proposed surface synthesis of heavily N-doped $N = 7$ AGNR **31** to proceed in two steps. First, surface assisted homolytic cleavage of C-Br bonds and diffusion to allow for formation of polymer **30**, then further annealing to fully conjugate the polymer to yield GNR **31**.

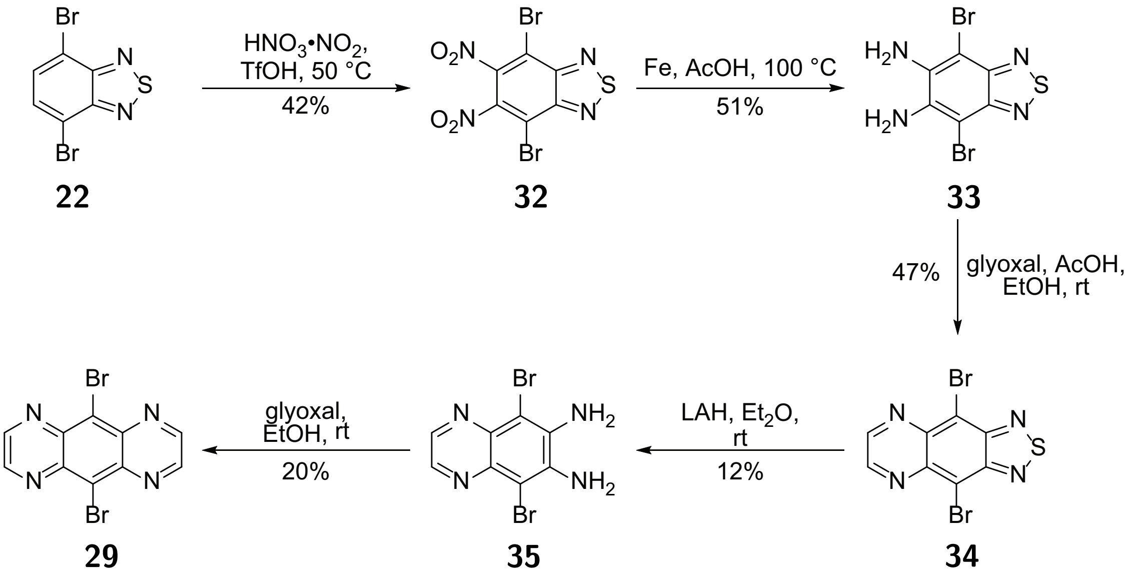

Scheme 2.9: Synthesis of heavily N-doped GNR monomer **29**

29 in one sequence were unsuccessful. Instead, the reduction and condensation steps had to be separated and performed in sequence. Reduction of the nitro groups with Fe powder yielded the free diamine **33** in moderate yield, which was then condensed with glyoxal to yield quinoxaline derivative **34**. A similar two-step reduction-condensation was performed on the thiadiazole ring by reaction first with $LiAlH_4$ to yield the diaminoquinoxaline **35**, then condensation with glyoxal to yield monomer **29**.

Chapter 3

Embedding Porphyrin Quantum Dots in Bottom-Up Synthesized GNRs

Quantum dots (QDs) embedded within semiconducting graphene nanoribbons (GNRs) represent a promising class of material for the realization of solid-state quantum computing. In this chapter, the synthesis of an atomically defined and highly tunable GNR-QD-GNR heterostructure is explored. The inclusion and control over the QD placement are confirmed by mass spectrometry and ^{13}C-NMR, and electronic communication and charge transfer between subunits are investigated using UV-Vis and EEM fluorescence spectroscopies. Site selective deposition of the GNR-QD-GNRs onto insulating surfaces is accomplished through coordination of the QDs to amine functionalized sites on the surface, crucial for further device fabrication studies.

3.1 Introduction

GNR-QDs

Semiconducting quantum dots (QDs) are considered attractive candidates for solid-state qubits, the fundamental building block of quantum computing. In particular, the use of spin in QDs to be the holder of quantum information has been investigated.[106] For this application, carbon based QDs are most highly desirable because the low spin-orbit coupling and weak hyperfine interaction in carbon leads to significantly longer spin coherence lifetimes than in other semiconducting QD systems (i.e. GaAs).[107] Among carbon-based materials, graphene's two-dimensional nature suits it well for integrated quantum nanodevice systems, however the gapless nature of graphene prevents its use directly.[108] For these reasons, quasi one-dimensional semiconducting GNRs are prime candidates for investigating semiconducting QDs.

Experimentally, however, the lithographic methods used to define these confined QDs in GNRs introduce sufficient defect density that the performance of the device is dominated by roughness, obscuring the materials intrinsic properties.[109] Recent progress in the bottom-up synthesis of GNRs allows for the generation of GNRs with atomic control over the width, edge structure, and heteroatom dopants.[65,66,72,80,83,87,91] The extension of the bottom-up synthesis of GNRs to include in-line QDs requires the ability to form atomically controlled heterojunctions within the ribbon. Experimental realizations of this technique have been accomplished by the randomized copolymerization of compatible monomers,[79,80] meaning that while each junction is well defined, the placement and number of junctions within the ribbon are not. Therefore, extending the control over atomic placement that bottom-up synthesis affords to include control over QD incorporation, new strategies are required.

To ensure perfect control over the number and placement of QDs incorporated into any GNR, a strategy involving heteroditopic monomer **36** and a series of homoditopic linker molecules was developed (Figure 3.1). By utilizing a dialkyne linker unit, the Diels-Alder polymerization guarantees that the active ends of the growing polymer chain express alkynes, thus allowing only the incorporation of more monomer and preventing the incorporation of more linkers.

Cove GNR Synthesis

Alkylated cove-type precursor monomer **36** was synthesized in a modification of a previous literature report (Scheme 3.1).[87] The synthesis is centered on the Knövenagel condensation between diphenylacetone **38**, synthesized in two steps from hexadecylbenzene, and 3-bromobenzil to yield the key tetraphenyl cyclopentadienenone core **39**. Installation of the terminal alkyne used in polymerization was accomplished by first Sonogashira cross coupling of **39** and TMS-acetylene, followed by silyl deprotection with KF to yield the monomer **36**.

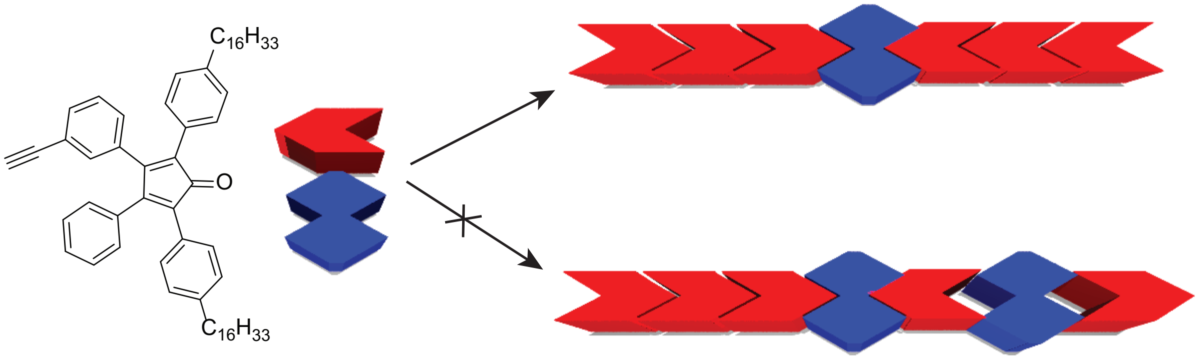

Figure 3.1: Due to the heteroditopic nature of the monomer containing both a terminal alkyne and cyclopentadieneone moiety, use of a homoditopic dialkyne linker ensures that exactly one unit will be incorporated into the polymer, preventing unwanted poly-incorporation.

3.2 Pyrene Based QD Linker

Synthesis

Synthesis of ^{13}C labelled dipropynyl pyrene linker molecule **45**, shown in Scheme 3.2 begins with dibromination of pyrene and separation of the 1,4- and 1,6-dibromopyrene isomers. Installation of the two terminal triple bonds is accomplished in two steps from **42** by first Sonogashira cross coupling with TMS-acetylene to yield **43**, followed by silyl deprotection with K_2CO_3 in MeOH to yield diyne **44**. Finally, introduction of the ^{13}C methyl group by deprotonation of the terminal alkynes with BuLi and quenching with ^{13}C-MeI to give **45**.

Incorporation of **45** into the desired polymer **46** was attempted in two ways. First, in the hopes of incorporating **45** between two pre-formed polymer chains, polymerization of **36** was conducted in the absence of **45** for three hours, followed by addition of **45** and further polymerization for 24 h. However, more significant incorporation was achieved by beginning the polymerization in the presence of **47** as in Scheme 3.3 to yield polymer **46** (M_n=17,000, PDI=1.3 by GPC). Notable in Figure 3.2B is the presence of a second feature in the GPC trace at higher retention time. This feature has been noted in previous reports of AB type Diels-Alder polymerizations and has been attributed to the formation of cyclic oligomers due to intramolecular head-tail reactivity.[87 91]

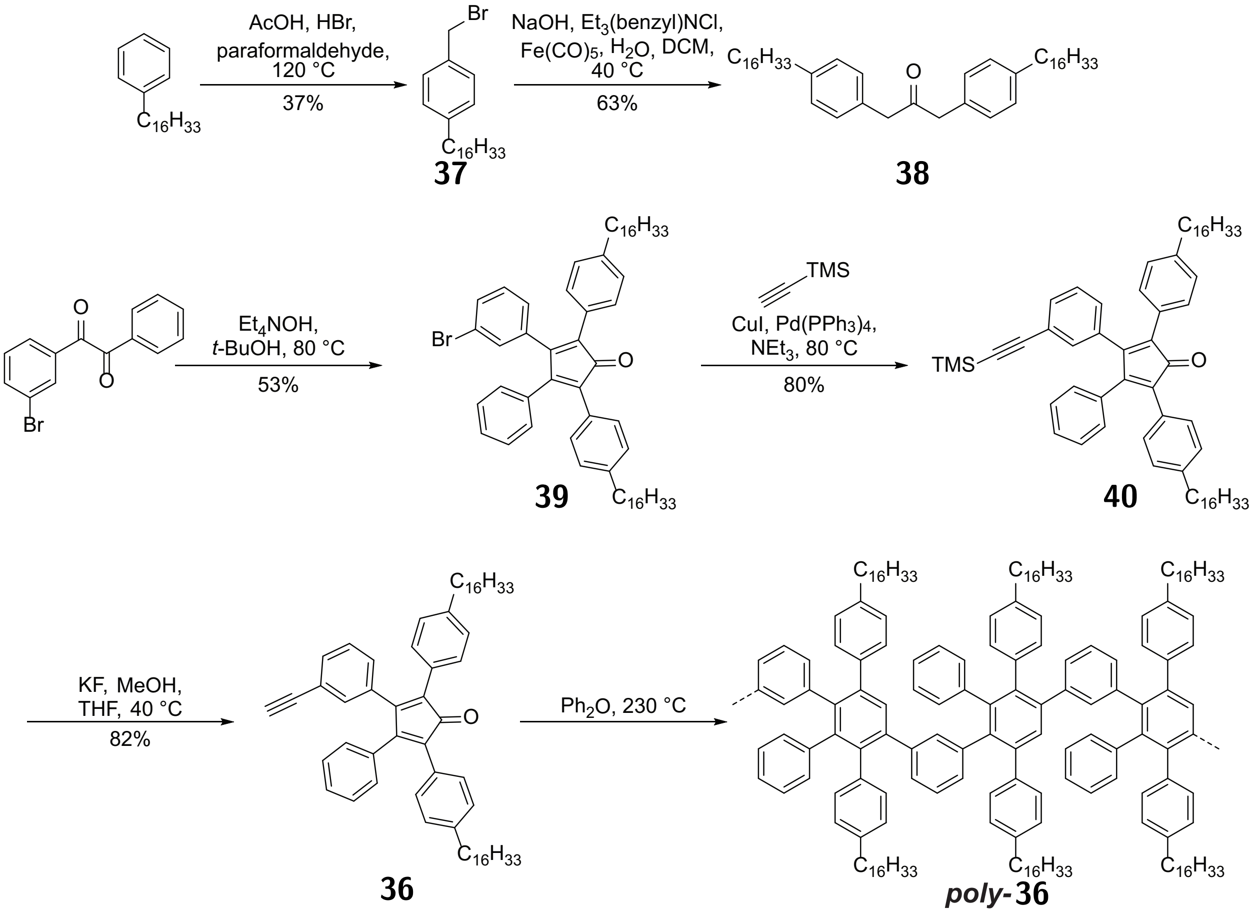

Scheme 3.1: Synthesis of cove type GNR precursor monomer **36**.

UV-Vis

Incorporation of **45** into polymer **46** is evidenced by comparison of distinctive features in the UV-Vis absorption spectra of **45**, **46**, and ***poly*-36** (Figure 3.2A). The distinctive three peak structure of **45** (red) is mirrored in **46**. However, while the features are similar they are notably blue shifted, indicating that the absorption is not due to unreacted **45** present in the mixture, but rather to a reaction of the unit. While this evidence does support the introduction of **45** into the polymer, it does not immediately prove that we have achieved the desired central location. To prove centrality, we turn to ^{13}C-NMR spectroscopy.

Quantitative ^{13}C-NMR

Figure 3.3, shows the alkyl region of the ^{13}C-NMR spectrum of labeled **45** (red) displaying a clear isolated signal at $\delta \approx 5$ ppm. When comparing ***poly*-36** to **46**, in the ideal case we

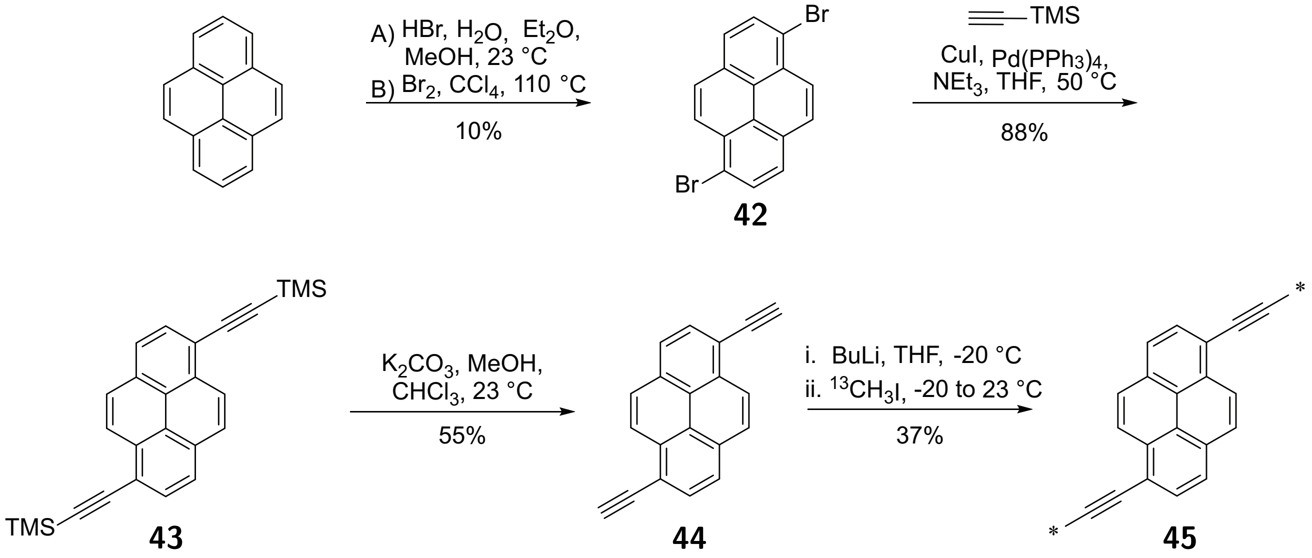

Scheme 3.2: Synthesis of ^{13}C-labelled pyrene linker **45**.

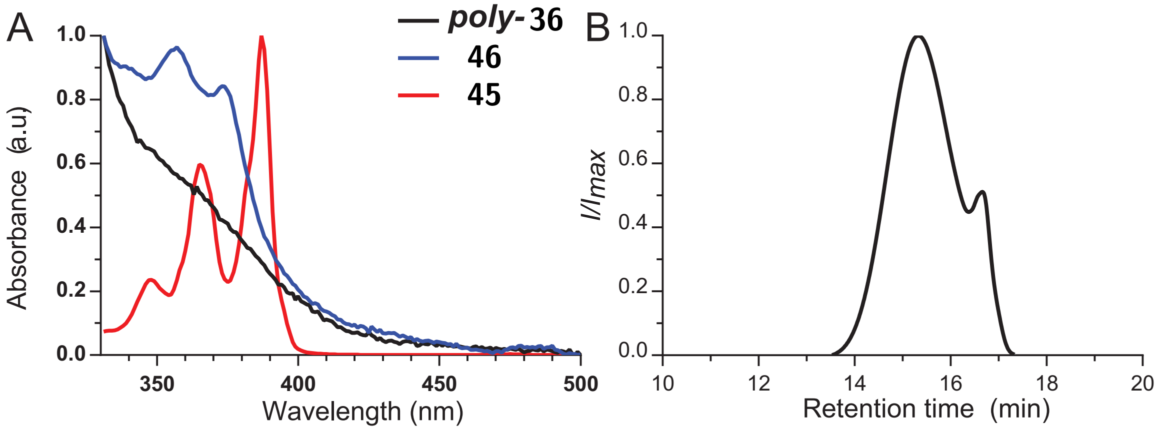

Figure 3.2: A) UV-Vis absorption spectroscopy of **45** (red), **46** (blue), and ***poly*-36** confirming incorporation of the pyrene unit into the polymer. B) GPC trace of **46** (M_n=17,000, PDI = 1.3), displaying a smaller, higher retention peak due to cyclic oligomers (M_n=5,400, PDI=1.0).

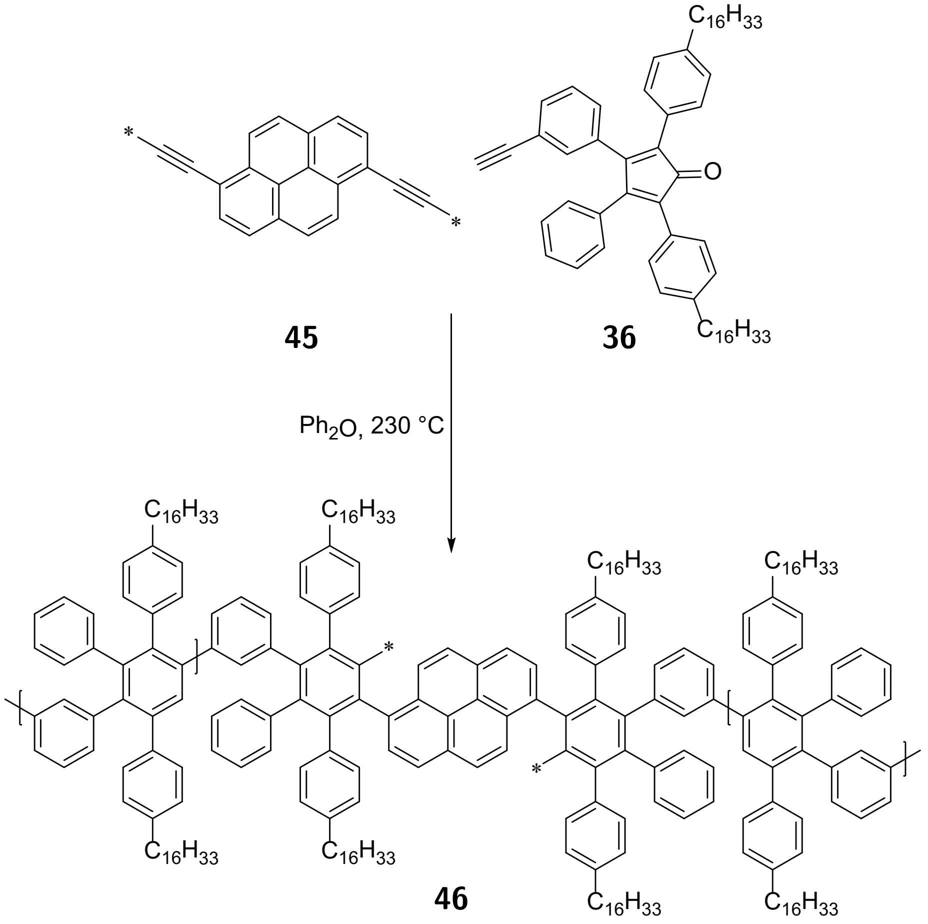

Scheme 3.3: Synthesis of ^{13}C-labelled **46**.

would note the complete disappearance of the resonance associated with the propyne methyl group, and appearance of a downshifted benzyl methyl resonance. However, instead, it is obvious that we see incomplete conversion of peak A to B. This would indicate that the produced structure is not the intended, symmetrically functionalized **46**, but rather a mono-functionalized **45** acting as a capping agent on ***poly*-36**. Quantitative ^{13}C-NMR analysis reveals that the ratio of symmetrically functionalized **36** to mono functionalized **36** is 15:1.

This low degree of incorporation at the propyne groups indicates that the internal triple bonds are not kinetically competitive during the polymerization. This is likely due to the increased steric hindrance surrounding the triple bonds of **45** when compared to the triple bonds of monomer **36** (Figure 3.4). This results from two structural changes: replacing a terminal hydrogen with a methyl group, and the added bulk of the fused pyrene ring. Because of this congestion the rate of reaction of the monomer is so much greater than that of the linker that while inclusion is not completely excluded, it is low enough to prevent its use in this system. To explore this hypothesis and remedy the problem, tetraphenyl linker

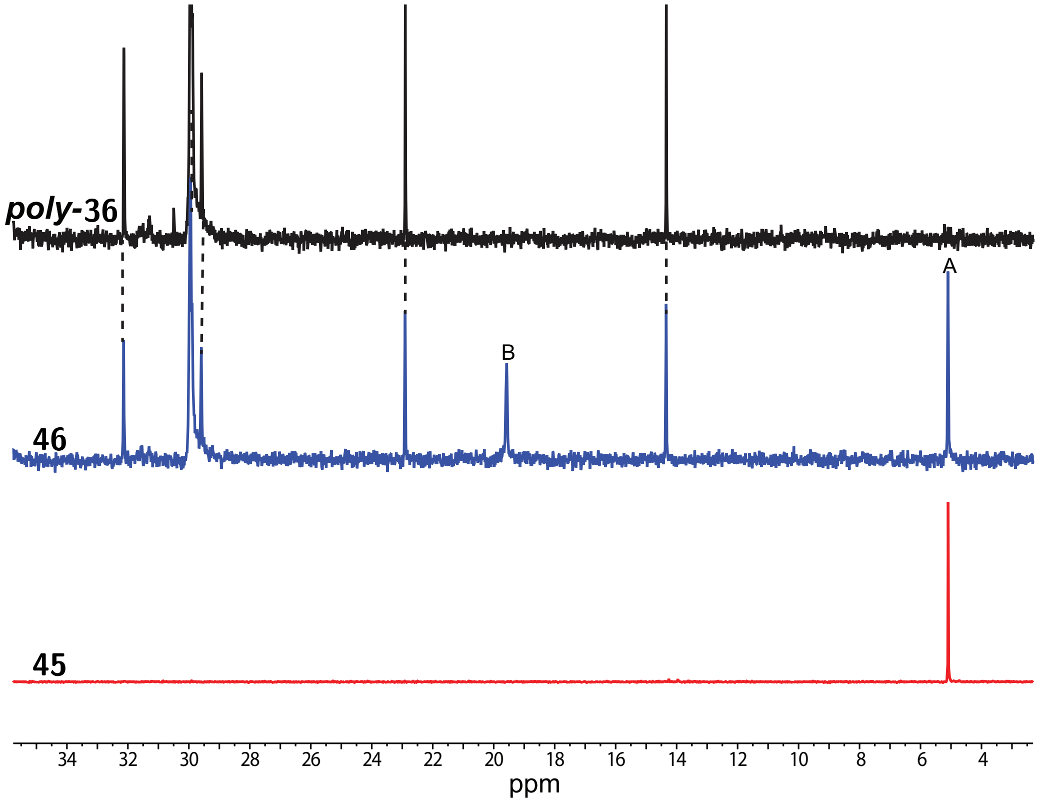

Figure 3.3: ^{13}C-NMR of **45** (red), **46** (blue), and ***poly*-36** (black) demonstrating incomplete, asymmetric reactivity of linker **45**.

48 was designed to have terminal triple bonds with steric bulk more comparable to that of **36**.

3.3 Tetraphenyl Based QD Linker

Synthesis

Tetraphenyl linker candidate **48** was designed to have more kinetically competetive triple bonds than the predecessor **45**. To increase steric bulk while maintaining the analytical handle that ^{13}C labeling affords, the isotopic enrichment was moved from a methyl group to the terminal triple bond carbon. Synthesis begins with **2** (Scheme 3.4), which was previously synthesized for the production of $N = 9$ AGNR monomer **4**. Suzuki-Miyaura cross coupling of **2** with phenylboronic acid yielded tetraphenyl core **49**. Conversion of the amines to labelled alkynes was accomplished in four steps. First, a modified Sandmeyer reaction replaced the amines with iodine atoms yielding **50**. Lithium-halogen exchange, followed by quenching with DMF then afforded dialdehyde **51**. Installation of the isotopically en-

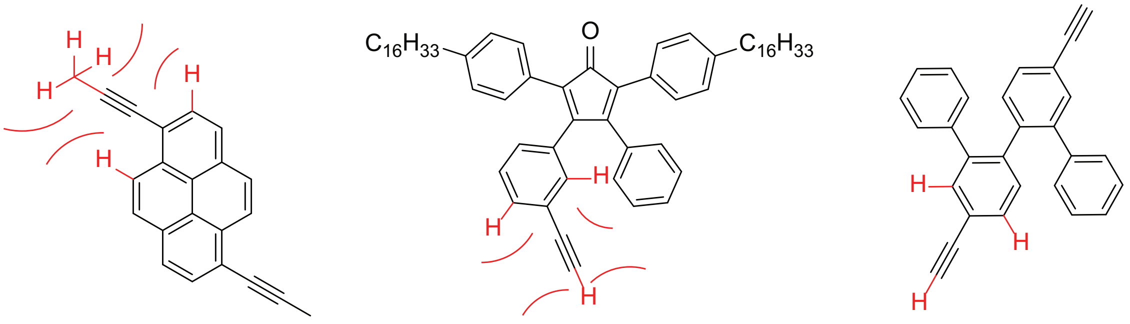

45 **36** **48**

Figure 3.4: Increased steric bulk around the internal alkynes of **45** as compared to monomer **36** results in lower inclusion. Tetraphenyl linker **48** is designed to be more kinetically competitive.

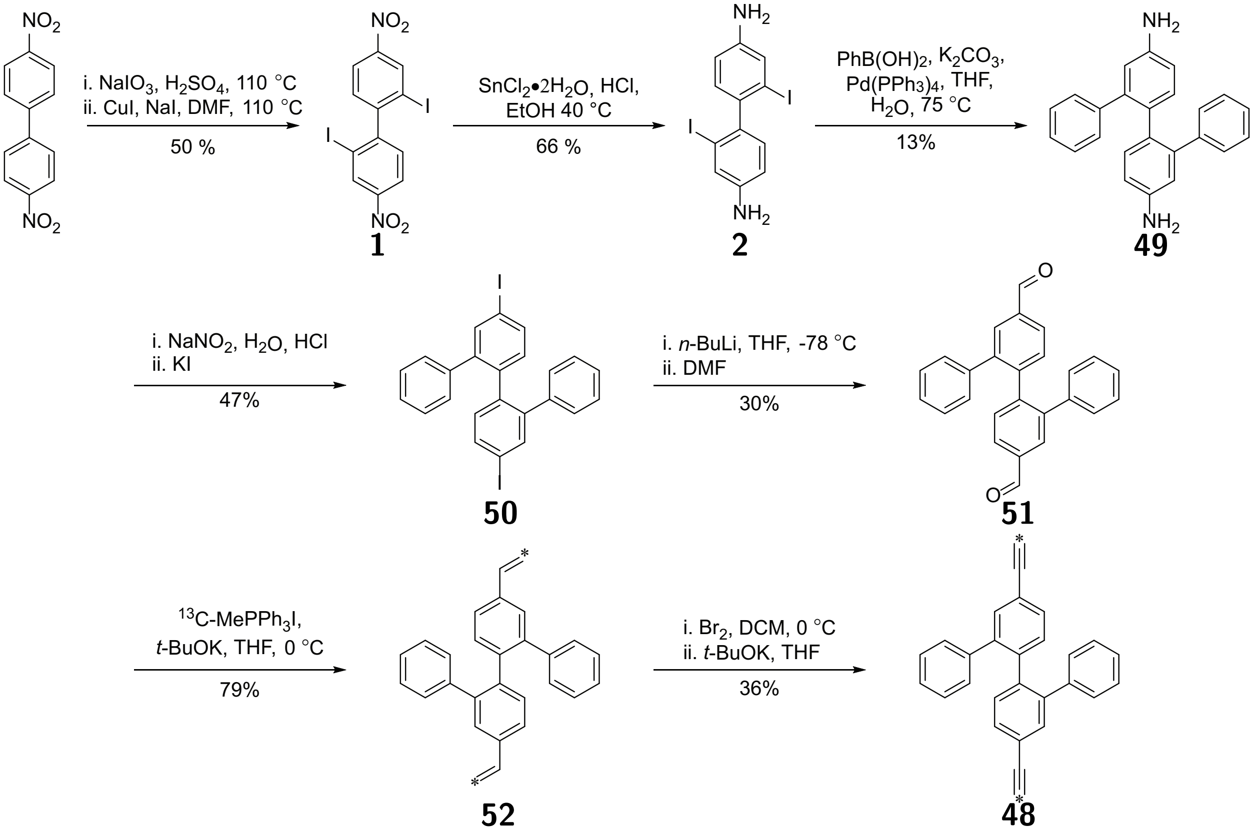

Scheme 3.4: Synthesis of ^{13}C-labelled tetraphenyl linker **48**.

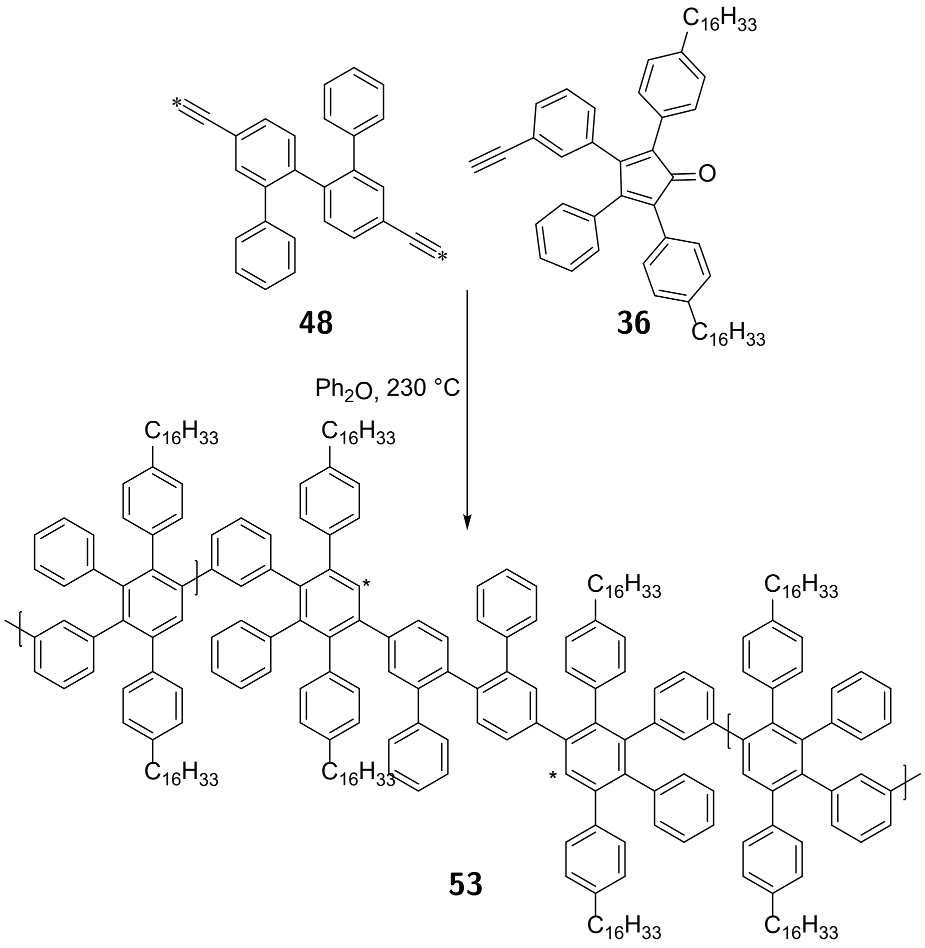

Scheme 3.5: Synthesis of ^{13}C-labelled **53**.

riched carbons was then achieved *via* Wittig reaction with ^{13}C-MePPh$_3$I, followed by one-pot tetrabromination-elimination to yield labelled diyne **48**. Incorporation of **48** into polymer **53** was accomplished analogously to **46** (Scheme 3.5). Analysis by GPC (Figure 3.5B) shows a main peak (M$_n$=11,000, PDI=1.3), with the secondary peak noted in Figure 3.2B appearing as a shoulder instead of an isolated peak due to greater overlap.

^{13}C-NMR

Figure 3.5A shows a comparison of the aryl regions in the ^{13}C-NMR spectra of ***poly*-36** and **53**. As in the case of the ^{13}C-NMR analysis of **46**, all of the resonances present in the aryl region of ***poly*-36** find matches in **53**. The important distinction to be made between this system and the previous one is the complete disappearance of the alkyne resonance associated with **48**, indicating that the decreased steric hindrance of **48** has indeed made

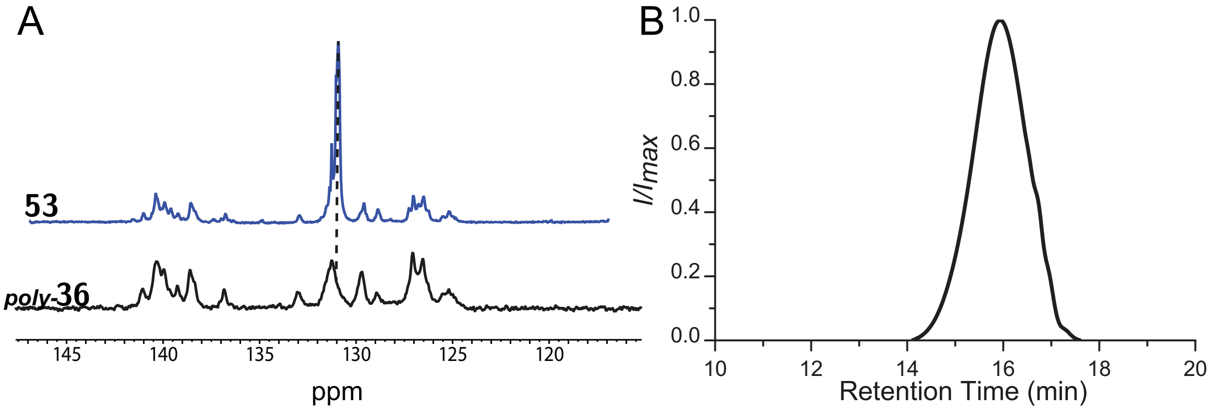

Figure 3.5: A)^{13}C-NMR comparison between ***poly*-36** and **53**, displaying a prominent new peak corresponding to the isotopically enriched carbons. B)GPC trace of **53**, M_n=11,000; PDI=1.3.

the alkynes more kinetically competitive, enabling symmetric placement of the linker within the polymer.

3.4 Porphyrin Based QD Linker

With this information regarding effective design of the linking moieties, a more electronically interesting and tunable system was designed for inclusion in the GNR-QD-GNR architecture. Porphyrins have been the subject of many molecular electronics studies, due in part to their propensity for electronic communication both in plane and, in the case of various metalloporphyrins, axially. Their highly tunable metal centers allow for fine tuning their magnetic and electronic properties, as well as their interaction with axially coordinated ligands. For these reasons, porphyrins are an attractive candidate for incorporation into a GNR-QD-GNR system.

Synthesis

To ensure symmetric, approximately linear incorporation into the precursor polymer, as well as to allow for continued monitoring by ^{13}C-NMR, A_2B_2 tetraaryl porphyrin **57** was chosen as a QD candidate. Synthesis of **57** is best accomplished by coupling aldehyde **56** with presynthesized *meso*-phenyldipyrromethane to reduce scrambling and formation of other, undesired porphyrin species as in Scheme 3.6. Aldehyde **56** was synthesized in three steps from monoprotected *para*-phthalaldehyde by first the two-step conversion of the aryl aldehyde to isotopically enriched alkyne **55** by Wittig reaction with ^{13}C-MePPh$_3$I, followed by bromination and elimination. Deprotection of the remaining acetal yields the requisite coupling partner **56**. Macrocyclization yields A_2B_2 porpyrin **57** in 11% yield.

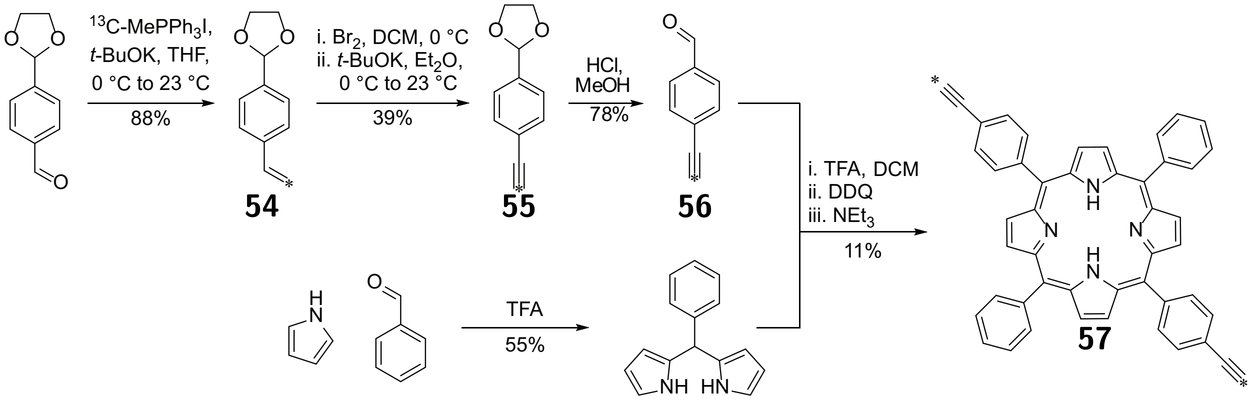

Scheme 3.6: Synthesis of ^{13}C-labelled porphyrin linker **57**.

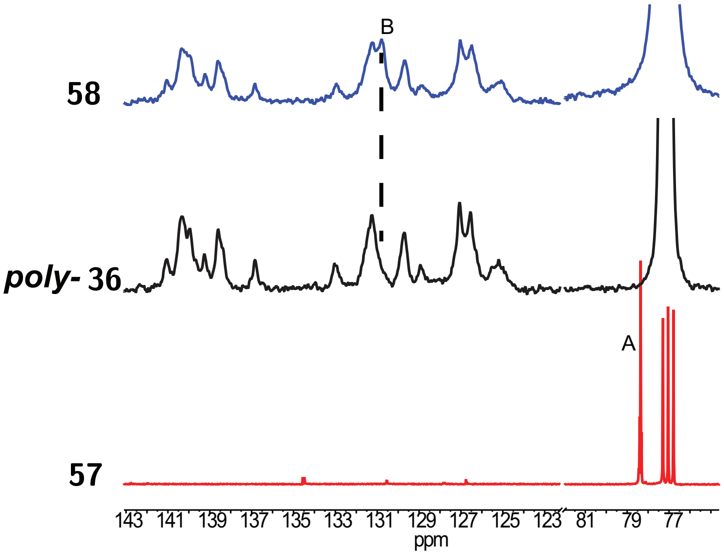

Figure 3.6: ^{13}C NMR of **57** showing clear ^{13}C enrichment of the terminal alkyne carbon, ***poly*-36**, and **58**, demonstrating clear consumption of labeled alkynes and replacement by a new aromatic peak B.

Synthesis of **58** was performed analogous to **53** and **46** by copolymerization of **36** and **57** in Ph_2O at 230 °C (Scheme 3.7). ^{13}C-NMR (Figure 3.6) confirms that the sterically unhindered terminal triple bonds of **57** are as kinetically competent as those of **36** and **48**. Complete disappearance of the isotopically enriched terminal alkyne carbon labelled A in **57** and the presence of peak B at $\delta = 130$ ppm supports complete, symmetric incorporation.

An unavoidable side product of the polymerization is homopolymer ***poly*-36**. While not readily detectable by analytical techniques like NMR or GPC, this impurity can be detected

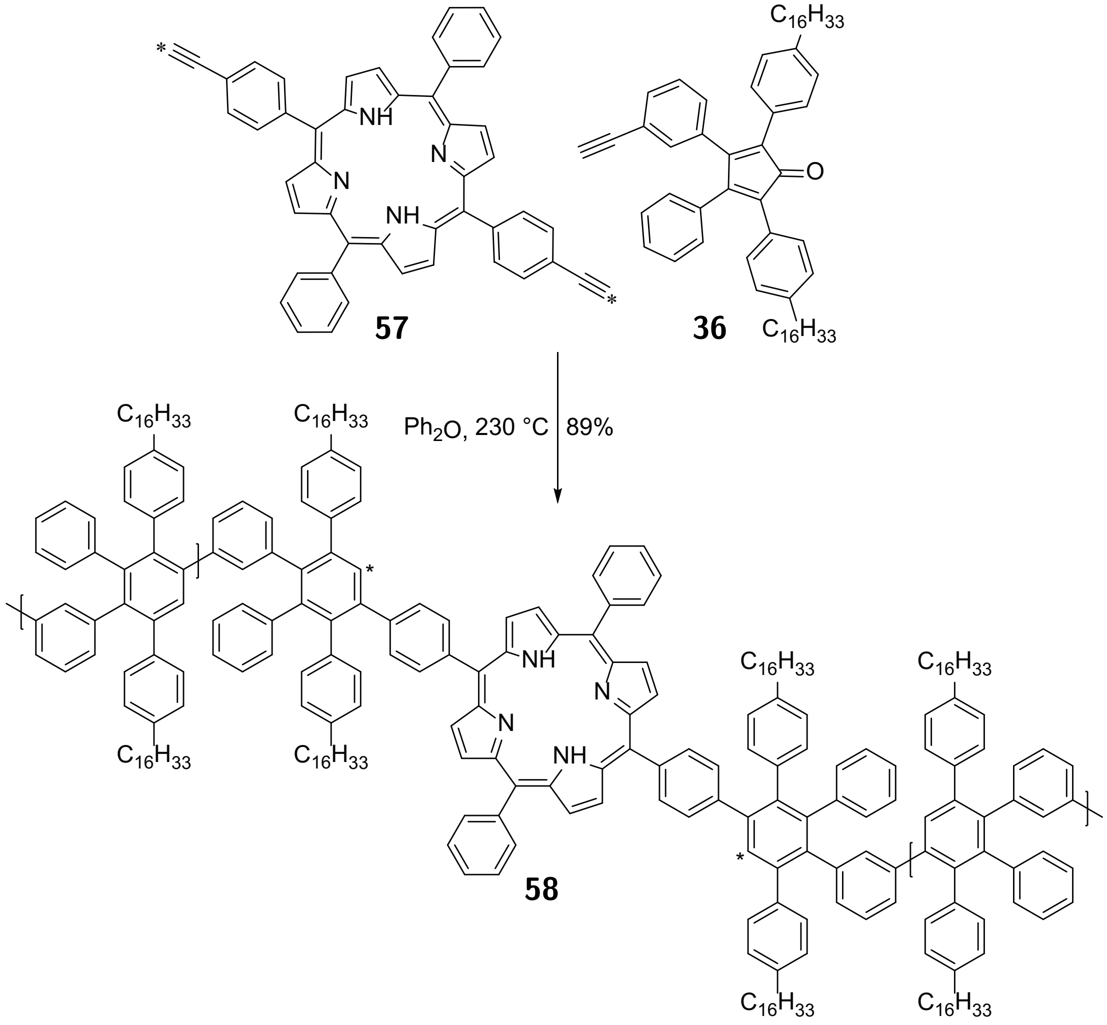

Scheme 3.7: Synthesis of ^{13}C-labelled **58**.

with MALDI-MS as shown in Figure 3.7A. The spectrum shows two clear families of peaks that have the repeat unit of the monomer (829 D), separated from each other by the mass of the porphyrin (662 D). Fractionation of the polymer mixture was accomplished *via* silica gel chromatography, eluting with 10% DCM in hexanes. With this, isolated samples of **58** and ***poly*-36** were obtained, as evidenced by MALDI-MS in Figure 3.7C and 3.7E respectively. This technique is most effective for smaller lengths of functionalized polymer, due to the increased contribution of the porphyrin to the overall polarity of the polymer, which can be seen when comparing the GPC traces of the resulting samples (Figure 3.7B, D, F). While the fractionated sample of ***poly*-36** (Figure 3.7F) is similar in length to the crude mixture (B), the isolated sample of **58** is notably shorter (D).

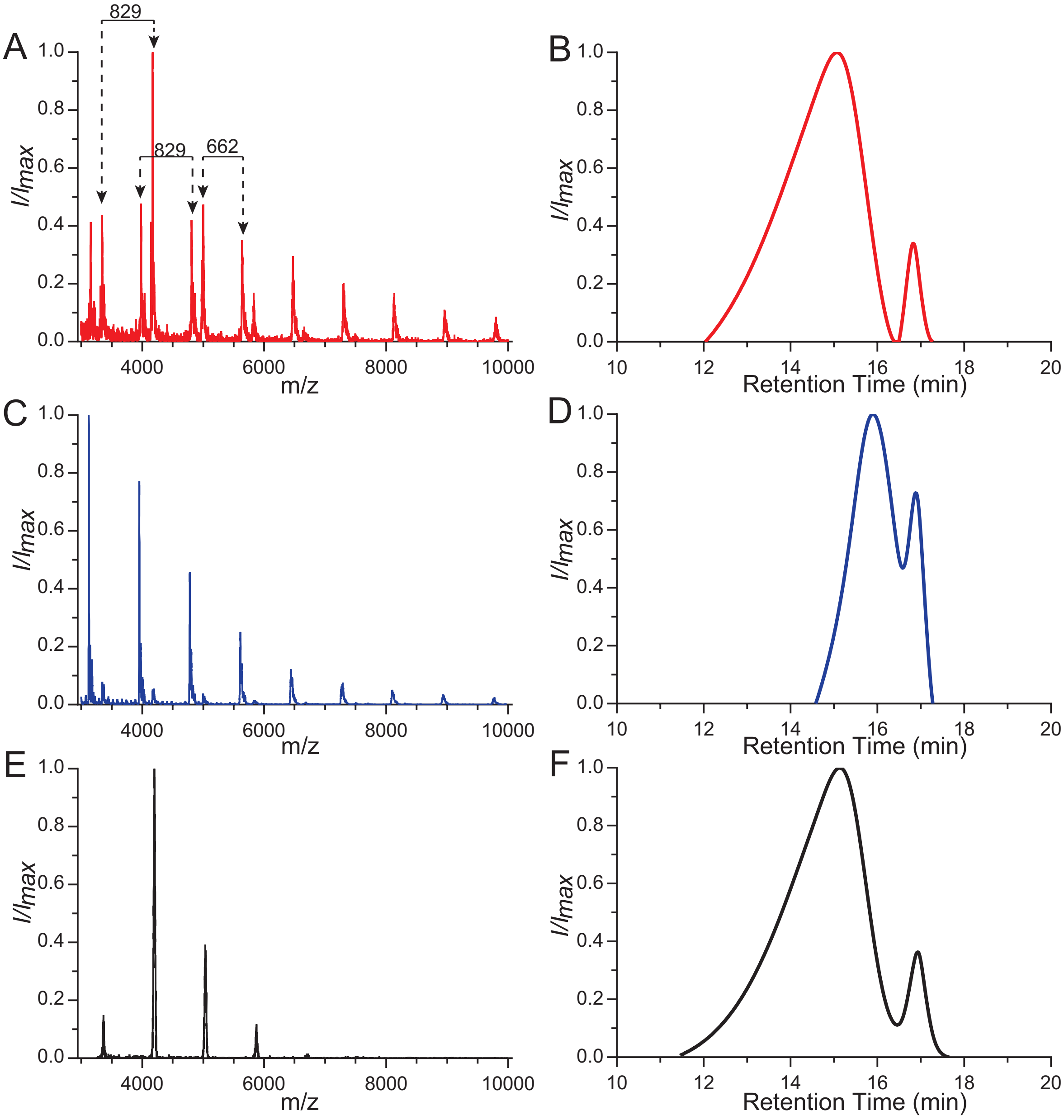

Figure 3.7: A) MALDI-MS and (B) GPC trace of crude mixture of **58** and ***poly*-36** (C) MALDI-MS and (D) GPC trace of fractionally isolated **58** (E) MALDI-MS and (F) GPC trace of the remaining, fractionally isolated ***poly*-36**.

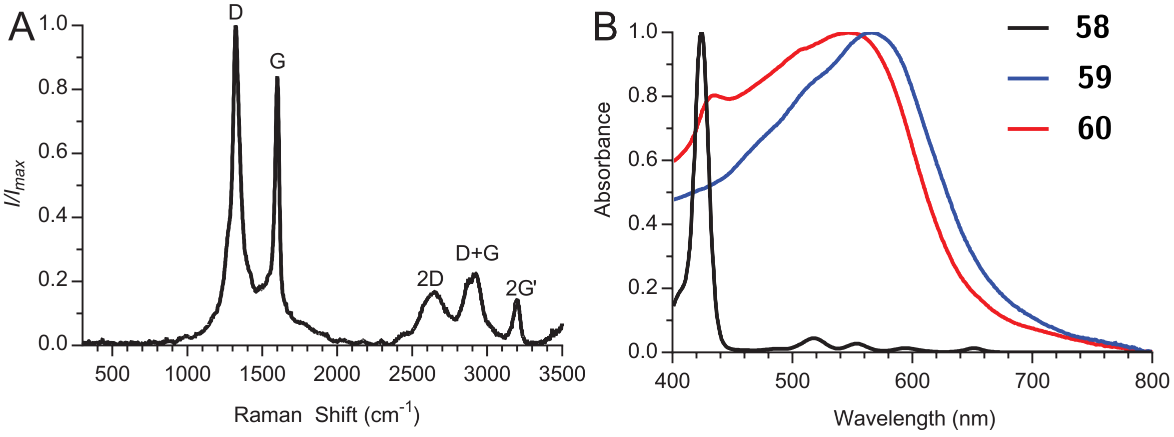

Figure 3.8: A) Raman spectrum of GNR-QD-GNR **60**. B) UV-Vis absorption spectra of precursor polymer **58** (black), cove type GNR **59** (blue), and GNR-QD-GNR **60** (red).

Graphetization and Raman

Porphyrin functionalized precursor polymer **58** was converted to GNR-QD-GNR **60** using Scholl oxidation conditions with $FeCl_3$ in DCM and $MeNO_2$. The resulting black powder was characterized by Raman spectroscopy (Figure 3.8A), which displays features consistent with unfunctionalized cove type GNRs, with notably narrow G band and well defined higher order peaks, indicating an efficient conversion.

UV-Vis

Both cGRNs **59** and GNR-QD-GNR heterostructures **60** featuring solubilizing hexadecyl side chains form stable dispersions after sonication and centrifugation in THF. The respective UV-vis absorption spectra are depicted in Figure 3.8B. A broad absorption at $\lambda_{max} = 556$ nm characteristic for cove-type GNRs dominates the spectrum of **60**. The λ_{max} of GNR-QD-GNR heterostructures **60** is only slightly shifted (≈ 6 nm) to shorter wavelength when compared to the absorption of pristine cGNRs. A second prominent absorption at $\lambda = 433$ nm in the spectrum of **60** can be attributed to the corresponding $S_0 \rightarrow S_2$ transition (Soret band) in the porphyrin core, while the characteristic Q-bands are obscured by the dominant absorption of the cove-type GNR segments. The bathochromic shift (≈ 10 nm) of the Soret band in **60**, compared to the A_2B_2 precursor **57** ($\lambda_{max} = 423$ nm), can be attributed to an efficient electronic coupling with the extended π-system of the adjacent cove-type GNRs.

Fluorescence

Figure 3.9A,B shows the excitation emission matrix (EEM) fluorescence spectra for cGNRs **59** and GNR-QD-GNR heterostructures **60**, respectively. Excitation of both pristine cGNRs

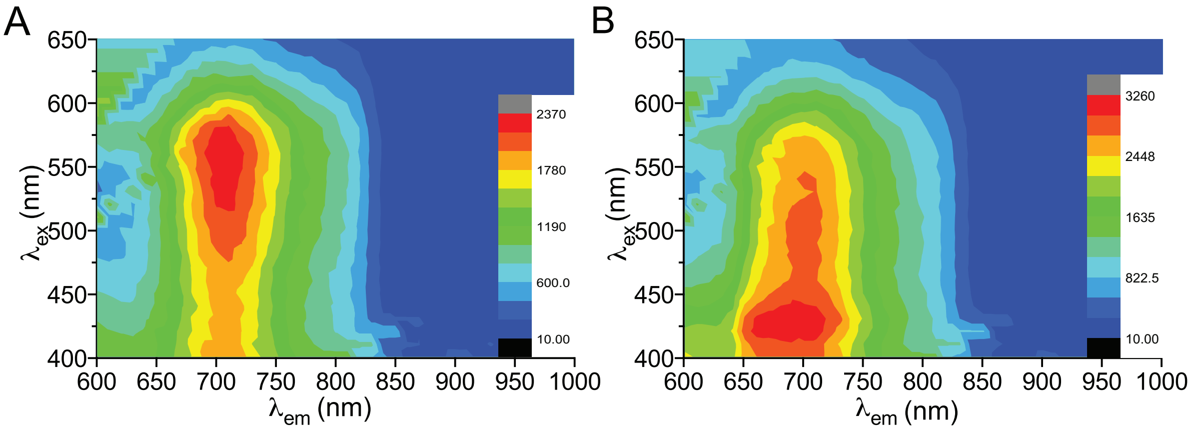

Figure 3.9: EEM fluorescence spectra of **59** (A) and **60** (B).

and **60** at $\lambda_{Ex} = 560$ nm leads to a broad fluorescence centered around $\lambda_{Em} = 705$ nm. If however the GNR-QD-GNR heterostructure **60** is excited at $\lambda_{Ex} = 425$ nm, close to the Soret band of the porphyrin core, a very broad emission $\lambda_{Em} = 650$–720 nm featuring characteristics of both the porphyrin and cove-type GNRs is observed. This indicates that the porphyrin S_2 excited state is able to relax either by fluorescing, or by transfering the excited state energy to the GNRs, which then fluoresce. The exchange between excited states in the porphyrin and the GNR further support a limited electronic communication between the central porphyrin quantum dot and the extended GNR segments.

Surface Functionalization and Raman Mapping

Fabrication of devices from isolated GNRs has been a major difficulty due to non-selective deposition and the tendency to form bundles.[83,85–87,89–91,94] An ideal deposition technique would utilize a means of increasing the strength of the interaction between the substrate surface being deposited onto and individual GNRs. The open axial coordination sites of **Zn@60** provide just such an opportunity. By functionalizing the target metal oxide surface with a self assembled monolayer (SAM) containing a coordinating group (in this case amines) as shown in Figure 3.10, deposition of **Zn@60** followed by removal of non-adhered material can yield even coverage without bundling.

Samples were prepared by patterning an Al_2O_3 on Si surface with Pt strips. After cleaning the exposed Al_2O_3 with O_2 plasma, the wafers were functionalized with aminated silane $(MeO)_3Si(CH_2)_3NH(CH_2)_6NH_2$ in refluxing toluene. The now aminated surfaces were submerged in a well dispersed sample of **Zn@60**, and then thoroughly rinsed to remove any non-adhered material. Mapping the intensity of the G peak in the Raman spectra on the resultant surface shows clear differentiation between areas that did and did not contain the coordinating SAM (Figure 3.11B), mirroring the same pattern seen in the optical image

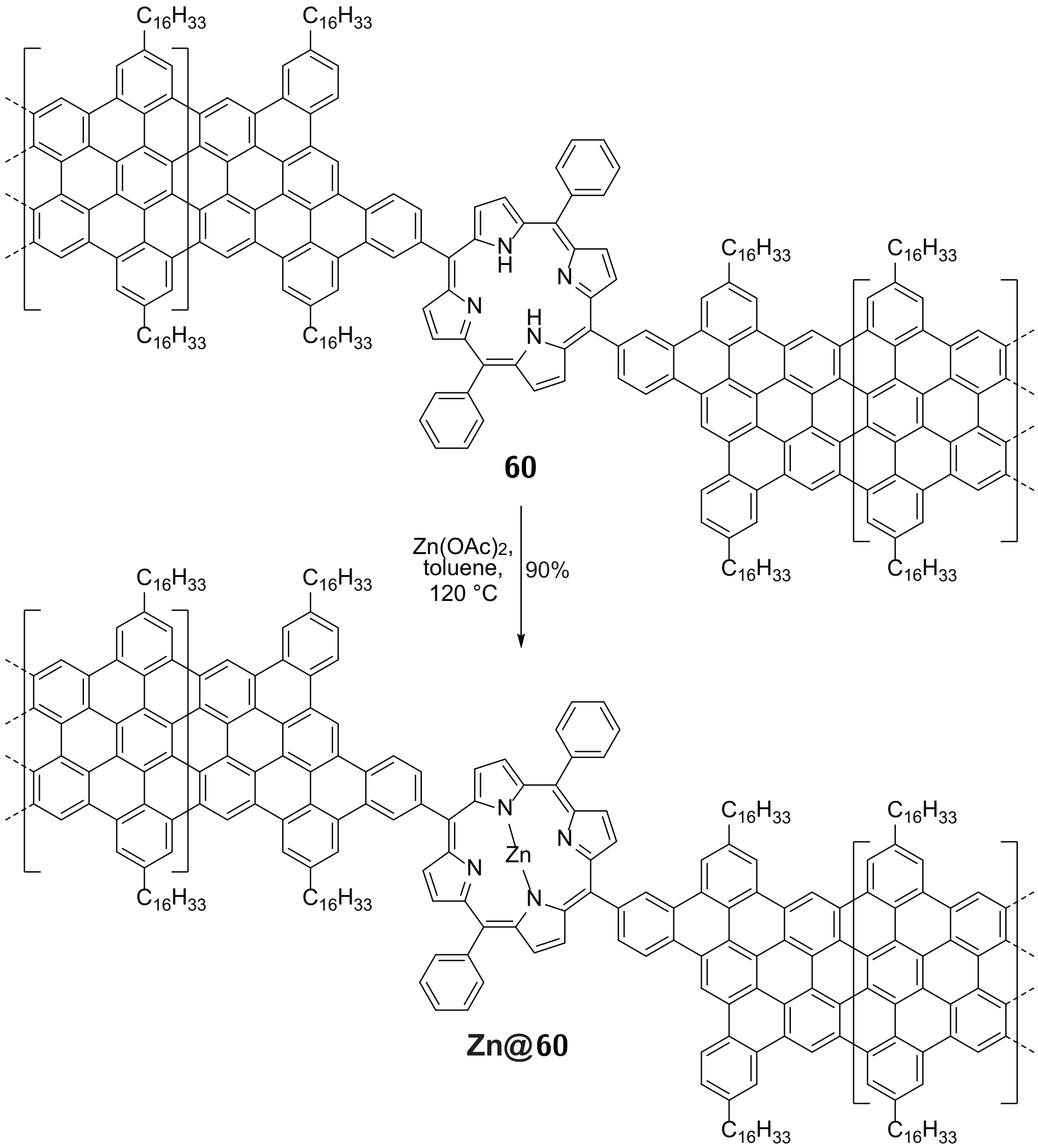

Scheme 3.8: Metallation of **60** to form metalloporphyrin GNR-QD-GNR heterostructure **Zn@60**.

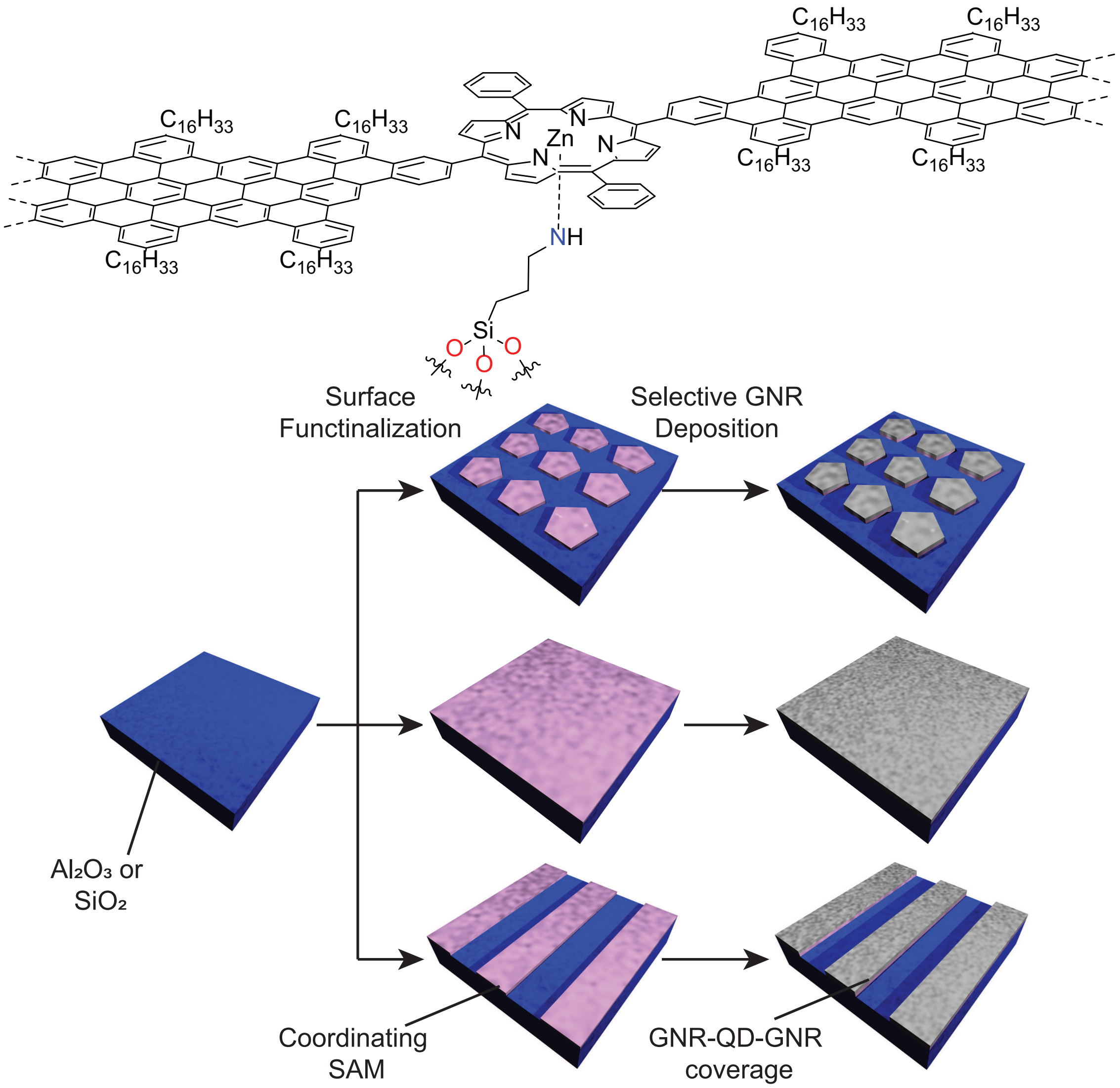

Figure 3.10: Functionalization of insulating surfaces (SiO_2 or Al_2O_3) with a coordinating aminosilane guides selective deposition of **Zn@60**.

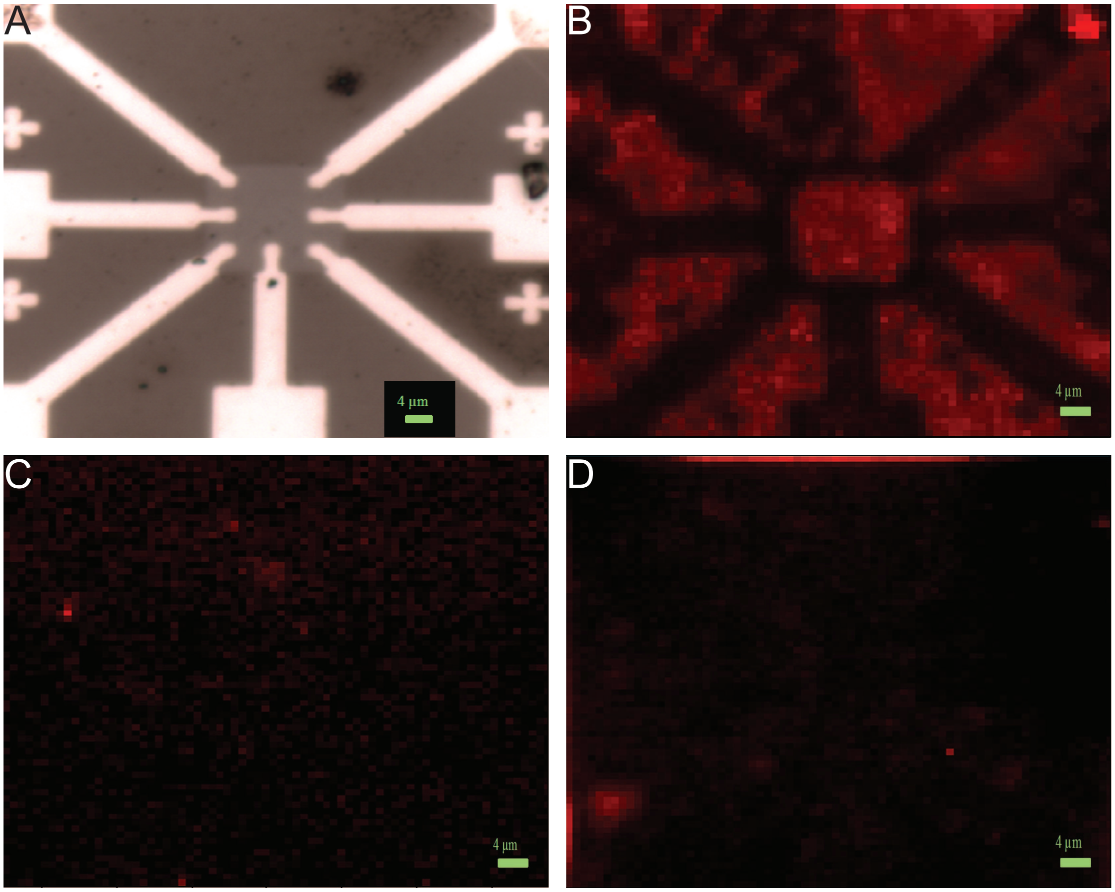

Figure 3.11: Optical microscopy image of Pt patterns on functionalized Al_2O_3 and Raman mapping of the G band of substrates after B) amine functionalization and **Zn@60** C) hydrocarbon functionalization and **Zn@60** D) amine functionalization and **59**.

(Figure 3.11A). In order to ensure that the selectivity seen is a result of axial coordination to the Zn metalloporphyrin, control experiments were undertaken. In the case of using **Zn@60** and a strictly non-coordinating hydrocarbon SAM, as well as in the case of the coordinating SAM with unfunctionalized cGNR, no contrast was observed in the Raman maps (Figure 3.11C and D respectively). It is worth noting that any minor features seen in Figure 3.11C or D are the result of inconsistent baseline, and not from observable G peaks (Figure 5.1).

Conclusion

In conclusion, a novel GNR-QD-GNR heterostructure with well defined stoichiometry and connectivity has been synthesized. Electronic characterization by UV-Vis absorption and EEM fluorescence spectroscopies reveals electronic communication between the constituent moieties. Selective, site specific deposition of the metal functionalized GNR-QD-GNR onto insulating surfaces functionalized with a coordinating SAM was performed and confirmed by mapping the G peak intensity in the Raman spectra. Future efforts will focus on device fabrication and characterization.

Chapter 4

GNRs as a Support Material for Inorganic Nanoparticles

In this chapter, bulk solution synthesized graphene nanoribbons are explored as conductive support materials for inorganic nanoparticles of two different applications: Au nanoparticles for electrocatalytic reduction of CO_2 to CO and SnO_2 nanoparticles as an anode material in lithium ion batteries. In both cases it is demonstrated that the GNRs form a flexible conductive matrix that stabilize the nanoparticles while allowing efficient electron and mass transport through the composite. Composite materials are additionally characterized by SEM, TEM, STEM, and Raman spectroscopy.

Parts of this chapter have been published in:
Rogers, C.; Perkins, W. S.; Veber, G.; Williams, T. E.; Cloke, R. R.; Fischer F. R. *J. Am. Chem. Soc.*, **2017**,*139*, 4052-4061.

While previous chapters have focused on the development of synthetic methods for novel GNRs and GNR heterostructures intended for single ribbon devices and applications, this chapter focuses on use of GNRs as a bulk material. The inherent tunability, conductivity, and tendency to form porous aggregates make GNRs an attractive replacement for other graphitic materials commonly used in the support of inorganic nanoparticles. two types of nanoparticles in particular will be explored here: Au nanoparticles used in the electrocatalytic reduction of CO_2 to CO, and SnO_2 nanoparticles used in potential next-generation lithium ion batteries.

4.1 Au Nanoparticles for CO_2 Reduction

Inorganic nanostructured materials, primarily realized in the form of nanoparticles (NPs), have emerged as competent heterogeneous catalysts for challenging chemical transformations.[110–113] While nanostructured catalysts promote the industrial scale production of value added chemicals, more recently their characteristics have inspired NP-based water splitting, fuel cell, and carbon dioxide (CO_2) reduction catalysts, relevant to a sustainable clean energy cycle.[114,115] While traditional catalyst design has focused on intrinsic structural parameters like size, shape, and composition of NPs,[116–122] the more complex variables of the nanostructured catalytic environment and the dynamic mass- and energy-transport processes at the solid/liquid or solid/gas interface remain insufficiently understood.[123] A more inclusive model that embraces the multifaceted role of the support along with the demonstrated tunability of NPs themselves offers new opportunities for the design and performance optimization of heterogeneous catalyst systems.[124] Indeed, the structural diversity of chemical environments surrounding catalytically active sites at the surface of NPs are typically described by ensemble measurements,[59,125,126] and this analytical challenge is further convoluted by the inherent inhomogeneity of common support materials such as carbon black (C_{black}), reduced graphene oxide (rGO), carbon nanotubes (CNTs), or inorganic metal oxides (MO_x) at the nanometer scale, preventing the development of instructive structureperformance relationships. By rational bottom-up design of a functional GNR support material it is possible to boost key performance parameters such as stability, selectivity, and activity, thereby enhancing the electrocatalytic reduction of CO_2 by gold nanoparticles (AuNPs) in aqueous solution. Electrochemical measurements further reveal that this molecular-materials support can influence the mechanism for CO_2 reduction at the nanoparticle interface.

AuNPs are appealing CO_2 reduction electrocatalysts as they offer aqueous compatibility and reasonable selectivity for CO_2 reduction to CO, together with the high surface area inherent to metal nanoparticles.[117,127] As electrocatalytic reduction of CO_2 at the surface of metal NPs follows a proton-coupled mechanism, it necessarily faces competing proton reduction, limiting the Faraday efficiency (FE) for CO production.[128,129] Moreover, competent nanoparticle catalysts frequently contend with low activity or prohibitively high overpotential for bulk applications.[115,119,130,131] Most pressing, however, is the issue of catalyst stability, as many nanoparticle electrocatalyst systems deliver strong performance for only minutes

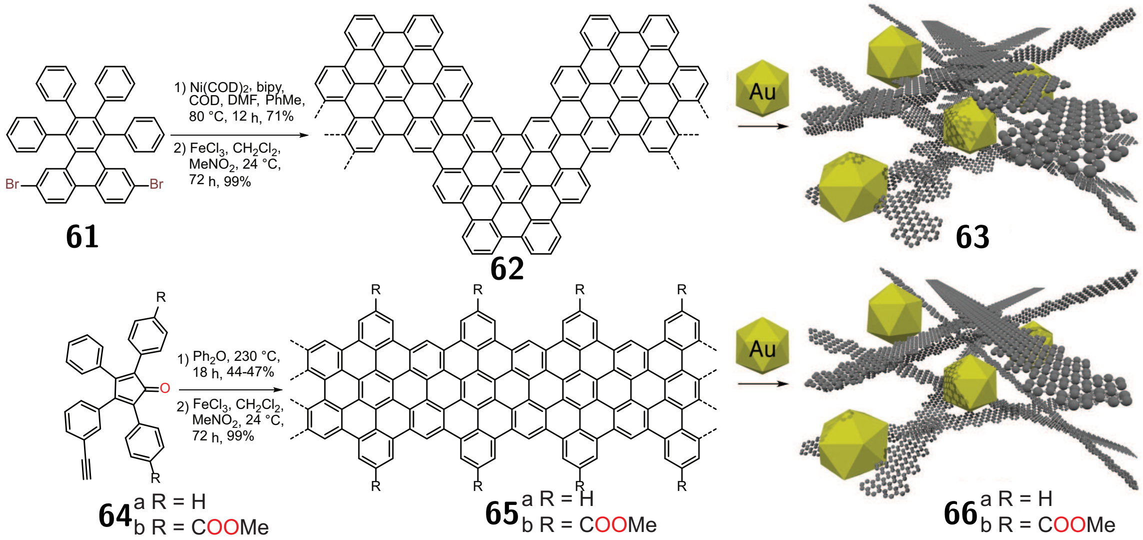

Figure 4.1: Design and bottom-up synthesis of GNR-AuNP composite materials. (A) Synthesis of chevron GNRs from molecular precursors. (B) Synthesis of cove GNRs from molecular precursors. Schematic representation of **63**, and **66** composite materials is not to scale.

before degrading under harsh electrocatalytic conditions.[130,132–135] Efforts to mitigate premature catalyst deactivation have highlighted the role of the support material in stabilizing nanodispersed metals.[133–138] Graphitic support materials in particular have drawn significant interest, largely because their structure and electronics facilitate strong interaction between the carbon support and metal nanoparticles.[139–143] These strong d-π interactions[140,144,145] lead to enhanced dispersion and stabilization of metal NPs and can serve to modulate the electronic structure at the NP surface.[138,146,147] As such, graphene,[142,148,149] GO,[150] rGO,[151] and CNTs[152–154] have been investigated as nanoparticle support materials, particularly in the contexts of fuel cells[136,152,154,155] and thermal catalysis.[140] While each of these graphitic materials carries certain inherent strengths and limitations, all of them notably lack rational tunability and structural homogeneity on the nanometer scale.

GNRs offer structural precision and tunability unrivaled among graphitic materials, since their structure follows deterministically from small-molecule precursors readily modified through organic synthesis. Electronic homogeneity follows from structural homogeneity, and as such, bottom-up GNRs do not contend with the variable band gaps and metallicity found in CNTs as previously discussed. With the combination of structural and electronic tunability with mechanical flexibility and a high aspect ratio graphitic topology, bottom-up GNRs are appealing materials for enhancing support-NP interaction and thereby exerting control over catalytic performance and stability. The potential enhancement is not restricted to the mechanical immobilization of metallic NPs within an inert matrix, but takes advantage of charge transfer at the GNR-metal NP interface, a Mott-Schottky heterojunction, that can

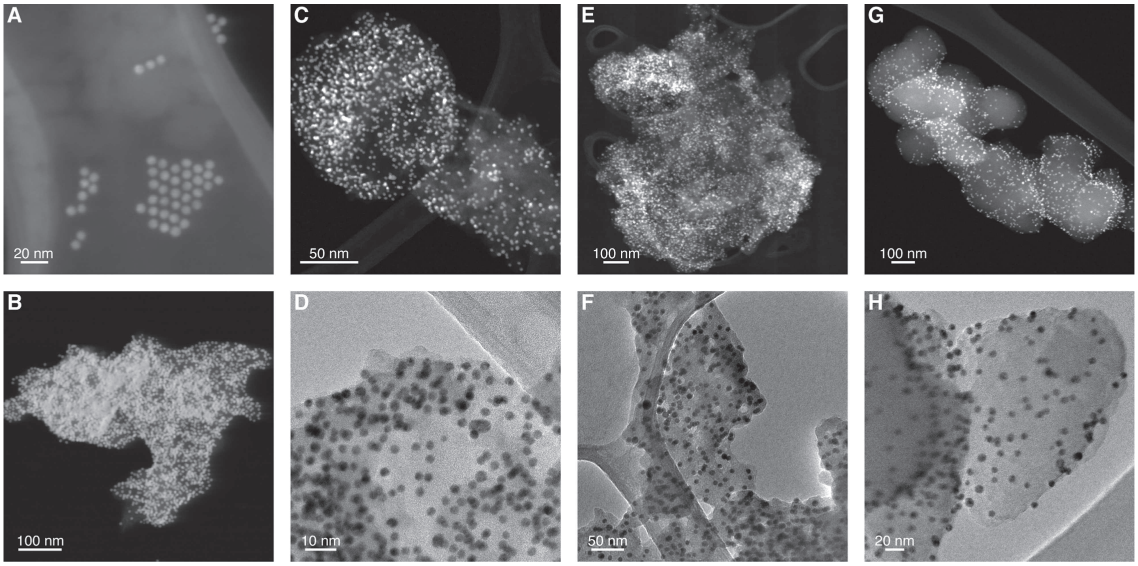

Figure 4.2: Electron microscopy of AuNPs and AuNP-GNR composites. (A) HAADF-STEM images of oleylamine-capped AuNPs show a narrow size distribution centered around an average NP diameter of 8 nm. (B) HAADF-STEM of unannealed **66a** composite shows the uptake of a high density of AuNPs into the GNR aggregate. (C) HAADF-STEM and (D) TEM images of **63** composite after annealing. (E) HAADF-STEM and (F) TEM images of **66a** composite after annealing. (G) HAADF-STEM and (H) TEM images of **66b** composite after annealing.

give rise to superior catalytic performance.[156–164] Inspired by the use of graphitic support materials (e.g., graphene, rGO, CNTs, mesoporous carbon), we explored structurally defined bottom-up synthesized GNRs as a functional support for AuNP electrocatalysis.

Chevron GNRs (**62**)[85] and cove GNRs (**65**a)[88,89] were synthesized following the bottom-up strategy outlined in Figure 4.1. While chevron GNR precursor **61** was prepared following a reported procedure,[165] the synthesis of molecular precursors for cove GNRs **64a** and **64b** is depicted in Scheme 4.1, following a general structure similar to the alkylated cove GNR precursor **36** discussed in previous chapters. Knoevenagel condensation of **67** with 1,3-diphenylpropan-2-one yielded the brominated cyclopentadienone **68**. Sonogashira cross-coupling of **68** with ethynyltrimethylsilane followed by deprotection of the TMS group gave the heterobifunctional molecular building block **64a**. The inherent flexibility of a rational bottom-up synthesis of graphene nanoribbons from molecular precursors is illustrated by the synthesis of a **64b**, a derivative of **64a** featuring methyl esters along its edges (Scheme 4.1). Knoevenagel condensation of **69** with 1,3-bis(4-bromophenyl)propan-2-one gave cyclopentadienone **70**, featuring both iodide and bromide substituents on the aromatic rings. Selective Sonogashira crosscoupling of **70** with ethynyltriisopropylsilane yielded the dibromocyclopentadienone **71**. Pd-catalyzed carbonylation of **71** in MeOH followed by deprotection

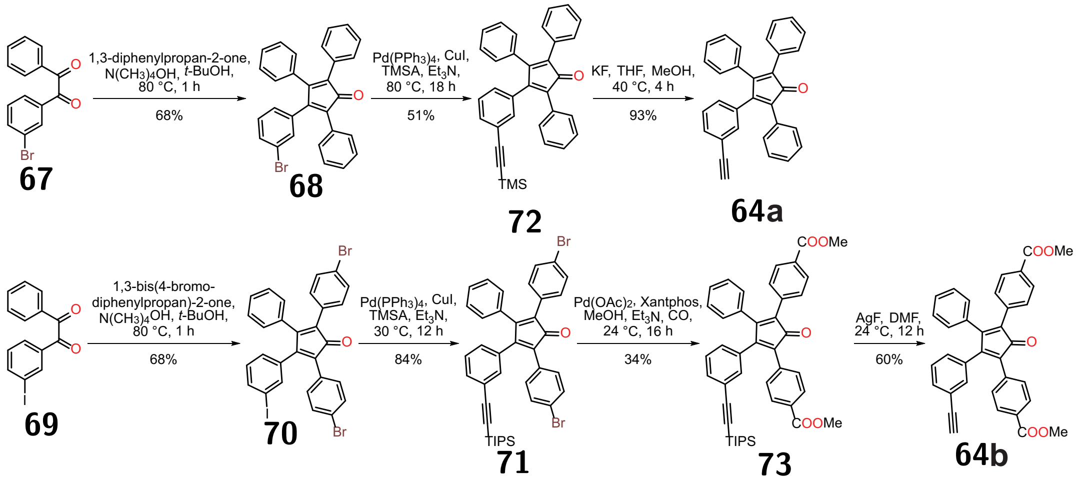

Scheme 4.1: Synthesis of Cove-Type GNR Precursor Monomer **64a** and Ester-Functionalized Cove-Type GNR Precursor Monomer **64b**.

of the TIPS group with AgF gave the molecular precursor for methyl-ester-functionalized cove GNRs **64b**.[166,167]

Step-growth polymerization of 2,7-dibromophenanthrene **61** or cyclopentadienone **64a**, followed by oxidative cyclodehydrogenation, yields structurally homogeneous samples of GNRs **62** and **65a**, respectively.[84,89,168] Notably, these syntheses are scalable, and can afford grams of GNR at a time. Raman spectroscopy of **62** and **65a** shows the characteristic signatures for D, G, and radial breathing like modes (RBLM) that are consistent with the formation of extended GNRs (Figure 5.2).[86,88,99] The successful removal of trace metals (Fe, Ni) used in the bottom-up synthesis of GNRs was confirmed by X-ray photoelectron spectroscopy (XPS) (Figure 5.3).

	BET Surface area[a] (m^2g^{-1})	AuNP electrochemically active SA[b] (cm^2mg^{-1} AuNP)	onset potential[c] (mV vs RHE)	CO_2 reduction activity[d] j_{CO}($A\ g^{-1}$)	ECSA-normalized CO_2 reduction activity[d] j_{CO} ($mA\ cm^{-2}$)
63	19.8	2.87	-0.36	22.6	7.87
66a	5.9	4.60	-0.14	36.8	8.00
C_{black}-AuNP	26.8	1.70	-0.54	6.4 g	3.76

Table 4.1: **Physical and Electrocatalytic Characterization of AuNP Composites.** [a]Measured by N_2 sorption at 77 K. [b]Measured by lead underpotential deposition. [c]Potential at which total CV activity exceeded 0.5 mA cm^2, measured in 0.5 M aqueous $KHCO_3$ saturated with CO_2 (pH 7.3). [d]Total CV activity at -0.87 V vs RHE, measured in 0.5 M aqueous $KHCO_3$ saturated with CO_2 (pH 7.3).

Oleylamine-capped monodisperse AuNPs were synthesized following a procedure derived from a previously reported method.[130,169] High-angle annular dark field scanning transmis-

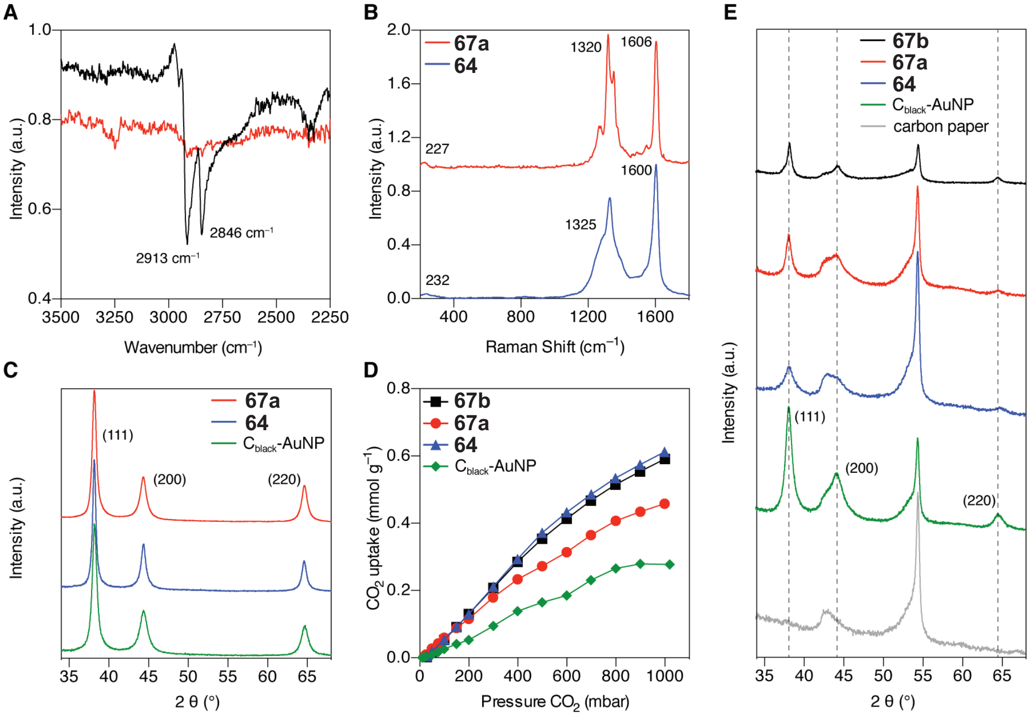

Figure 4.3: Characterization of AuNP-GNR composite materials. (A) IR spectroscopy of **63** composite materials prior to (black) and after (red) annealing. The characteristic vibronic signature associated with the oleylamine capping ligand is absent after the annealing at 185 °C for 10 h. (B) Raman spectra of **63** (blue) and **66a** (red) exhibit unaltered characteristic GNR peaks. (C) PXRD patterns of GNR- and C_{black}-AuNP composite powders exhibit the characteristic signals of AuNPs. (D) 298 K CO_2 adsorption experiment for GNR- and C_{black}-AuNP composites. Despite having lower BET surface areas, GNR composites uptake more CO_2 than the comparable C_{black} composite, reflecting their greater microporosity. (E) PXRD of composite AuNP electrodes prepared by depositing **66b** (black), **66a** (red), **63** (blue), and C_{black}-AuNP (green) on conductive carbon paper (gray) followed by annealing at 185 °C for 10 h.

sion electron microscopy (HAADF-STEM) of AuNPs shows the expected narrow size distribution centered around an average NP diameter of 8 nm (Figure 4.2A). GNR-AuNP composite materials were prepared by sonicating a dispersion of equal mass of AuNPs and the respective GNRs **62** or **65a** in hexane. The high affinity of AuNPs for the GNR support is immediately evident as the red AuNP solution loses its characteristic color upon sonication with GNRs, becoming a dark suspension. HAADF-STEM of the isolated black powder,rinsed with hexane and drop cast onto TEM grids, shows the uptake of the AuNPs into large nanoribbon aggregates (Figure 4.2B). GNR-AuNP composites commonly range in size from 0.2 to 1.0 μm and feature a substantial concentration of nanoparticles; STEM images of GNR samples prepared without AuNPs show aggregates of comparable size and morphology (Figure 5.4). The high density of AuNPs and the lateral overlap observed in transmission mode images suggest the AuNPs are embedded within a threedimensional GNR network, rather than perched on its surface.

Following incorporation of AuNPs into the GNR matrix, the oleylamine capping ligands decorating the surface of AuNPs were removed by annealing GNR-AuNP composites in air at 185 °C for 10 h.[127] STEM and TEM images of annealed samples show that composite aggregates remain intact and are comparable in size and morphology to those observed prior to annealing (Figure 4.2C–F). IR spectra of samples prior to and immediately after annealing confirm that the oleylamine ligands have been removed, leaving pristine AuNPs behind (Figure 4.3A).[169] Raman spectra of annealed GNR-AuNP composites show no shift or broadening of the diagnostic D, G, and RBLM modes (Figure 4.3B), indicating that the integral structure of the GNRs remains unaltered. Powder X-ray diffraction (PXRD) of the black GNR-AuNP composite shows the characteristic broadened signals of AuNPs (Figure 4.3C).[130,170] Although the NPs have been stripped of their stabilizing ligand shell, only minimal coalescence of the nanoparticles during the annealing process is observed by STEM, indicating an efficient stabilization of uncapped AuNPs through dispersion interactions with the GNR matrix.

Traditionally, NP support materials emphasize high surface area as a crucial factor to dynamic mass transport to and from the catalytically active surface.[114,171,172] However, surface area measurements derived from N_2 adsorption at 77 K (BET model, Table 4.1 showed that both **66a** (5.9 m^2 g^{-1}) and **63** (19.8 m^2 g^{-1}) composites present lower surface areas than a reference composite prepared from C_{black}-AuNP (26.8 m^2 g^{-1}). This behavior is not unexpected in aggregates of a graphitic material, for which strong dispersion interactions between graphene planes lead to stacking and low BET surface area.[173] Furthermore, it has been shown that N_2 adsorption at 77 K does not appreciably capture ultramicroporosity (pore size $<$ 0.7 nm) due to restricted diffusion of N_2 into micropores at low temperature.[174–178] CO_2 absorption at 298 K is not restricted by micropore diffusion and provides a better approximation for the transport of small gas molecules through the GNR matrix.[179,180] AuNP composites of **62** and **65a** show more than twice the CO_2 uptake measured for the C_{black}-AuNP reference (Figure 4.3D), reversing the trend in BET surface area observed for N_2 adsorption. These results suggest a significant microporosity for the GNR aggregates in comparison to the C_{black} composite, and is an indication that GNRs, despite their inherently

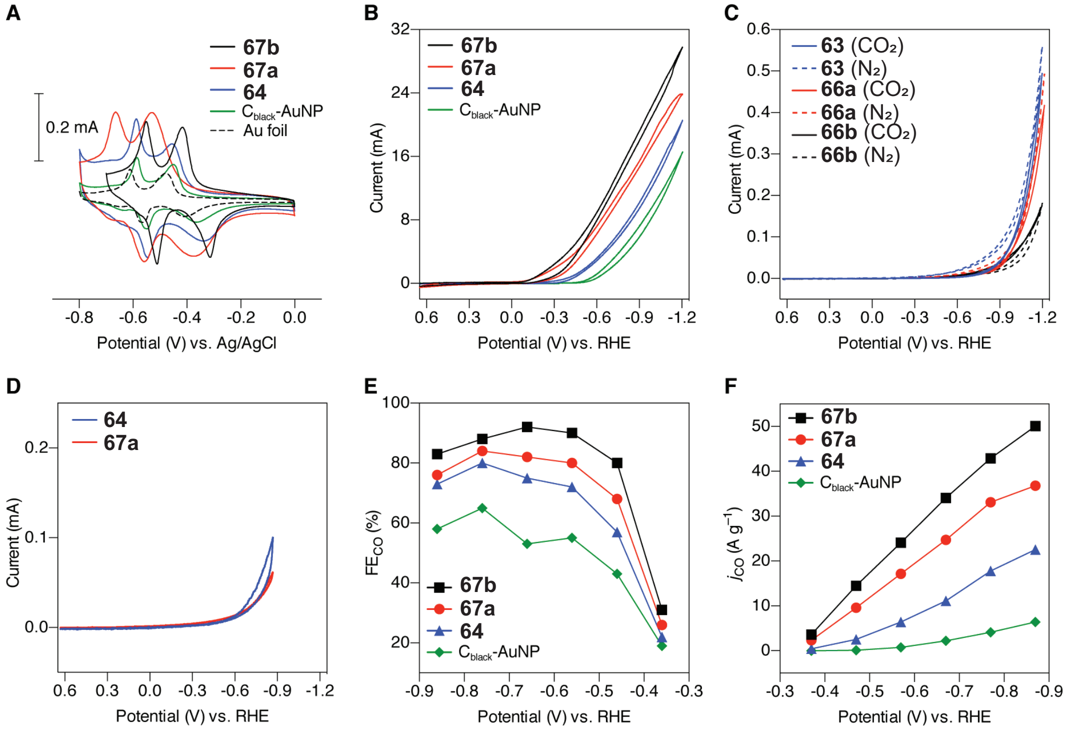

Figure 4.4: (A) Lead underpotential deposition experiments to determine the AuNP electrochemically active surface area (ECSA) of AuNP composite electrodes. Pb-UPD experiments for **63** composite electrodes (blue), **66a** composite electrodes (red), and **66b** composite electrodes (black) indicate much higher ECSA for the GNR composites than for C_{black}-AuNP composite electrodes (green). The active surface area was determined on the basis of a reference Au foil electrode (black). (B) Cyclic voltammograms of **63** (blue), **66a** (red), and **66b** (black) composite materials in 0.5 M aqueous $KHCO_3$ saturated with CO_2 (pH 7.3). The performance of C_{black}-AuNP (green) serves as a standard reference. (C) Cyclic voltammograms of **62** (blue), **65a** (red), and **65b** (black) electrodes, prepared without AuNPs, in 0.5 M aqueous $KHCO_3$ (pH 7.3) saturated with CO_2 (full lines) and N_2 (dotted lines). (D) Cyclic voltammograms of **63** composite electrodes (blue) and **66a** composite electrodes (red) in 0.5 M aqueous $KHCO_3$ (pH 7.3) saturated with Ar. (E) Faradaic efficiencies for CO production (FE_{CO}) by **63** (blue triangles), **66a** (red circles), **66b** (black squares), and C_{black}-AuNP (green diamonds) composite electrodes. Electrolysis performed at potentials from -0.37 to -0.87 V vs RHE in 0.5 M aqueous $KHCO_3$ saturated with CO_2 (pH 7.3). (F) Partial current for CO production (j_{CO}) by **63** (blue triangles), **66a** (red circles), **66b** (black squares), and C_{black}-AuNP (green diamonds) composite electrodes. Electrolysis performed at regular potentials from -0.37 to -0.87 V vs RHE in 0.5 M aqueous $KHCO_3$ saturated with CO_2 (pH 7.3).

low surface area, can facilitate mass transport within NP composite aggregates.

We determined the electrochemically active surface area (ECSA) of AuNP composites using lead underpotential deposition experiments (Pb-UPD) (Figure 4.4A and Table 4.1.[122,169,181,182] All samples display two characteristic signals in the Pb-UPD voltammograms, corresponding to lead deposition on the Au(111) and Au(110) faces, respectively. Integration of the peaks in comparison to a Au foil standard provides a quantitative measure of the accessible surface area of the AuNPs. Electrodes fabricated from GNR-AuNP composites have greater ECSA values (2.87 and 4.60 cm^2/mg AuNP for **63** and **66a** composites, respectively) than the corresponding C_{black}-AuNP reference (1.70 cm^2/mg AuNP) at the same nanoparticle loading. ECSA is a direct quantitative measure for the ability of a support material to disperse and immobilize nanoparticles without obstructing the transport of reactants and products to and from the nanoparticle surface.[137,138,151,152] The significantly higher ECSA measured for GNR-AuNP composites indicates that GNRs, and in particular GNR **65a**, facilitate the dispersion of AuNPs and do not obstruct access to the catalytically active metal surface.

In an effort to benchmark the performance of GNR-AuNP composite materials with respect to traditional supports like C_{black},[127] we studied the electrocatalytic reduction of CO_2 in aqueous $KHCO_3$ buffered solution. AuNP composites withsingle-walled carbon nanotubes (SWCNTs) were examined as a second point of reference, but the comparatively poor performance of the SWCNT composites made them an unsuitable standard (Figure 5.5). GNR-AuNP composite electrodes were fabricated by drop casting a sonicated dispersion of AuNPs and the respective GNRs (1:1 by mass with either **62** or **65a**; composites made using GNR **65b** are discussed later) in hexane onto conductive carbon paper, followed by thermal annealing in air at 185 °C for 10 h. The characteristic PXRD pattern of AuNPs in these annealed electrodes matches that of the composite bulk powders characterized above (Figure 4.3E). Cyclic voltammetry of the resulting composite electrodes (Figure 4.4B) in 0.5 M aqueous $KHCO_3$ saturated with CO_2 (pH 7.3) reveals a strong synergistic effect between nanoparticles and GNRs. Composite electrodes formed from GNRs **62** or **65a** and AuNPs deliver significantly more current than corresponding electrodes made from AuNPs alone, or AuNPs supported by a C_{black} matrix. Notably, electrodes fabricated from GNRs without any added AuNPs produce minimal current across the entire examined potential window (Figure 4.4C), indicating that the GNRs themselves are not electrochemically active. The current enhancement observed in GNR-AuNP composite electrodes disappears in the absence of CO_2 (Figure 4.4D), suggesting the excess current drives CO_2 reduction.

When compared to a C_{black}-AuNP reference, GNR composites exhibit a catalytic onset (defined here as the potential at which current density exceeds 0.5 mA cm^2) at significantly positively shifted potentials (0.36 V for **63** and 0.14 V for **66a** composites, versus 0.54 V for C_{black}- AuNP, all potentials versus reversible hydrogen electrode (RHE), Table 4.1, indicating the catalytic environment created by the GNR support significantly lowers the required overpotential for CO_2 reduction on AuNPs. This shift in catalytic onset is consistent with the formation of a Mott Schottky heterojunction at the GNR-AuNP interface.[69,156,157,160,162] Lower work function materials promote charge migration across the semiconductorNP inter-

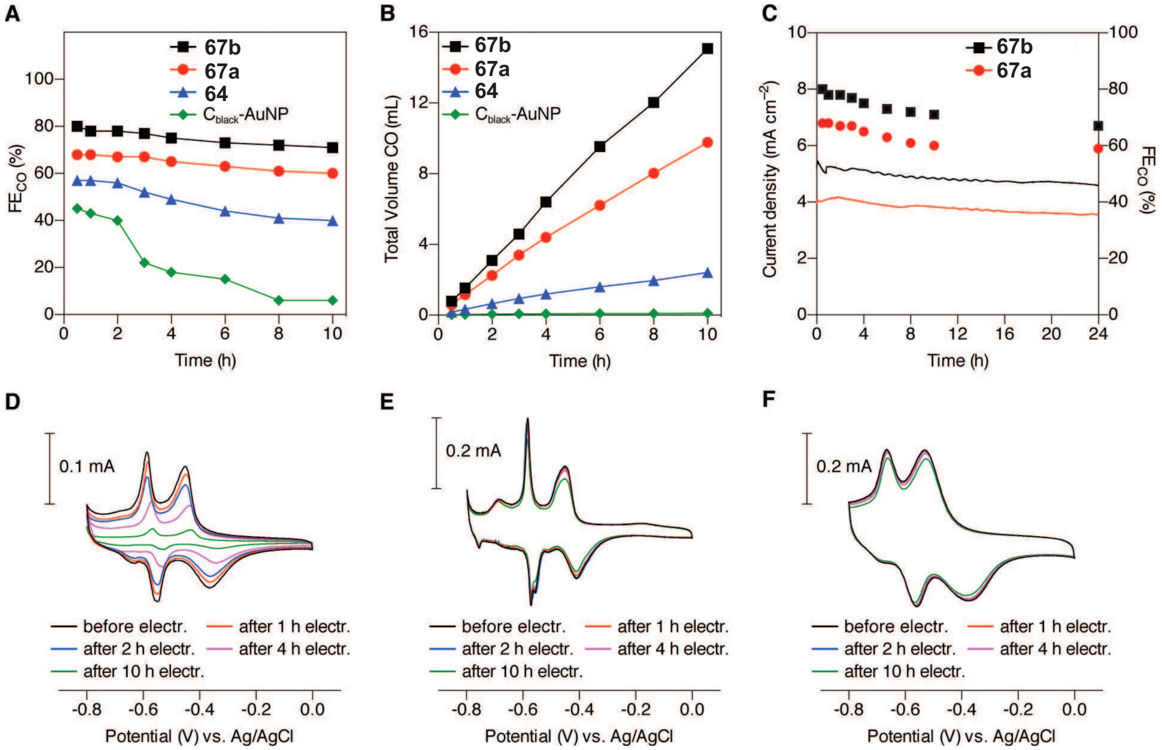

Figure 4.5: (A) Faraday efficiencies for CO production (FE_{CO}) by **63** (blue triangles), **66a** (red circles), **66b** (black squares), and C_{black}-AuNP (green diamonds) composite electrodes. Electrolysis performed in 0.5 M aqueous $KHCO_3$ saturated with CO_2 (pH 7.3). (B) Total volume (at STP) of CO produced by **63** (blue triangles), **66a** (red circles), **66b** (black squares), and C_{black}-AuNP (green diamonds) composite electrodes. Electrolysis performed in 0.5 M aqueous $KHCO_3$ saturated with CO_2 (pH 7.3). (C) Total current density for **66a** (red line) and **66b** (black line) over 24 h. Faraday efficiency for CO production with **66a** (red circles) and **66b** (black squares) over 24 h. Both current density and Faraday efficiency show little change between 10 and 24 h of fixed potential electrolysis at -0.47 V vs RHE. (D–F) Cyclic voltammograms for lead underpotential deposition experiments on AuNP composite electrodes following extended controlled-potential electrolysis at -0.47 V vs RHE, to measure the change in AuNP ECSA. Cyclic voltammetry was performed in 0.1 M aqueous KOH containing 1 mM $Pb(OAc)_2$ and purged with Ar. (D) C_{black}-AuNP composite electrodes exhibit a significant decline in ECSA following fixed potential electrolysis experiments. (E) **63** composites and (F) **66a** composites retain almost all of their ECSA following fixed potential electrolysis experiments.

face toward the high work function AuNPs, increasing electron density at the metal surface and shifting the catalytic onset.[139,150,152,153,183–188] Theory and experiment indicate that the semiconducting GNRs employed here, and particularly cove-type GNRs, feature appreciably lower work functions than other carbon supports like graphene or C_{black}, consistent with the positively shifted onset potentials observed Table 4.1.[86,145,154,187,189–193]

One hour controlled-potential electrolysis experiments over a potential range from 0.87 to 0.37 V underline the synergybetween AuNPs and GNRs. Both Faraday efficiency (FE_{CO}, Figure 4.4E) and partial current (j_{CO}, Figure 4.4F) for CO_2 reduction to CO by GNR-AuNP composites dramatically exceed those of C_{black}-AuNP across a broad potential window. Selectivity in particular was starkly improved for GNR composites, with increased j_{CO} leading to FE_{CO} values exceeding 80%, as much as 29 percentage points higher thanthose of C_{black}-AuNP composites across the entire potential window. **66a** composites deliver the highest activity and selectivity, consistent with a larger ECSA and lower CO_2 reduction onset potential.

Notably, at potentials distant from their catalytic onsets, the activity of GNR composites is closely proportional to their measured ECSAs (Table 4.1). While GNRAuNP composites do not suppress hydrogen evolution, as the partial current for proton reduction (j_{H_2}) is comparable to C_{black}-AuNP composites (Tables 5.1–5.4), the observed increase in selectivity reflects a greatly enhanced activity of GNR-AuNPs toward CO_2 reduction.

We performed bulk electrolysis experiments to evaluate the ability of GNRs to stabilize AuNPs overextended reaction times (Figure 4.5A). AuNPs supported by C_{black} degrade rapidly, delivering only 22% FE_{CO} after 3 h. Electrodes instead fabricated from GNR-AuNP composites maintain superior performance for more than 10 h of continuous electrolysis. At -0.47 V, **66a** composites retained 88% of their original FE_{CO} after 10 h of catalysis, and produced more than 33 mL CO/mg of AuNP, compared with only 0.4 mL CO/mg AuNP for the C_{black} composite electrodes prepared from the same AuNPs (Figure 4.5B). Longer controlled-potential experiments indicated that the **66a** composite in particular had reached a plateau of stability; with over 24 h of uninterrupted catalysis at -0.47 V, the composite delivered 87% of its original FE_{CO}, nearly unchanged from the 10 h experiment (Figure 4.5C).

We interrogated the origin of nanoparticle stabilization in GNR-AuNP composites. Pb-UPD experiments at selected time points during bulk electrolysis reveal the change in the ECSA of the AuNPs. During the electrolysis with C_{black}-AuNP composites (-0.47 V), a significant reduction in active Au surface area, that correlates with the loss of catalytic activity, can be observed within hours (Figure 5D). After 4 h of catalysis, only 48% of the original Au surface area remains, and only 15% is retained after 10 h. TEM images of C_{black}-AuNP composites recorded following 3 h of bulk electrolysis suggest that a plausible mechanism of deactivation relies on the coalescence of AuNPs to form larger aggregates with significantly reduced active surface area (Figure 5.6).[132] **63** (Figure 4.5E) and **66a** (Figure 4.5F) composites effectively prevent NP coalescence and the associated reduction in ECSA. **66a** composites in particular lose only 4% of their active Au surface area over 4 h of catalysis (10% over 10 h). We suggest that the effective immobilization of the NPs through strong dispersion interactions with the matrix of narrow, flexible GNRs effectively precludes NP mobility and prevents coalescence into larger structures.

A unique advantage of bottom-up synthesized GNRs as functional nanoparticle supports, unmatched by other graphitic support materials, lies in their inherent molecular-level tunability. The rational synthesis from small-molecule precursors provides an absolute control over key functional parameters such as shape, dimension, and electronic structure, and enables the deterministic introduction of functional groups. GNR **65b**, a cove-type GNR bearing methyl carboxylate groups along its edges, was synthesized from the ester-functionalized cyclopentadienone **73b** (Scheme 4.1). Raman spectroscopy of **65b** shows characteristic peaks for the D, G, and RBLM peaks reminiscent of the unsubstituted **65a**, while IR spectroscopy confirms the presence of methyl carboxylate groups in the fully cyclized GNR (Figure 5.7). AuNP composites prepared from the ester-modified **65b** resembled those of **65a** by STEM and TEM (Figure 4.2G,H), and displayed a similar low surface area (12.6 m^2 g^{-1}) and CO_2 uptake behavior at 298 K (Figure 4.3D). The ECSA of **66b** as measured by Pb-UPD (4.4 cm^2/mg AuNP) was very similar to that of the parent **66a** composite (Figure 4.4A). The electrocatalytic performance of **66b** composites, however, was found to be strikingly different from that of the unfunctionalized composite (Figure 4.4E,F). A significantly increased CO_2 reduction activity is reflected in both an increased j_{CO} and a higher FE_{CO}, and can only be attributed to the functionalization of the GNR support. A 1 h controlledpotential experiment at −0.66 V revealed a 92% FE_{CO} for the **66b** composite, a remarkable improvement over the 53% FE_{CO} observed for the C_{black}-AuNP composite under the same conditions. In comparison to composites of the unfunctionalized GNR **65a**, the rate of hydrogen production is nearly unchanged, but FE_{CO} is improved across the potential window owing to an approximately 50% increase in the rate of CO production (Tables 5.1–5.4).

The improved performance is retained throughout long-term experiments; for a 10 h experiment at −0.47 V, **66b** electrodes deliver an overall FE_{CO} of 71%, retaining 91% of the FE_{CO} performance (78%) exhibited in the first hour at that potential (Figure 4.5A). A 24 h experiment at the same potential delivered a total FE_{CO} of 67% (86% of the FE_{CO} recorded for the first hour), with the composites characteristic increased activity remaining nearly constant for the duration (Figure 4.5C). Over the course of 10 h, the ester-functionalized composite produced more than 50 mL of CO/mg AuNP, representing a 137-fold increase in total catalytic output over the same nanoparticles embedded in a C_{black} matrix (Figure 4.5B). The overall efficiency performance of **65b** composite after 10 h of electrocatalysis is comparable to the first hour of composite **65a**, and exceeds the initial performance of any other material tested.

To better understand the source of the marked increase in performance exhibited by **66b** composites, the kinetics of CO_2 reduction for each composite were studied using Tafel analysis. Figure 4.6 shows that the functionalization of cove GNRs with methyl carboxylates alters the mechanistic pathway for CO_2 reduction at the Au nanoparticle surface. A Tafel slope of 141 mV/decade for C_{black}-AuNP is consistent with the expected value for a rate-limiting single-electron transfer to adsorbed CO_2 to generate the radical anion.[131,191,192] This observation and proposed mechanism conform with previous studies of aqueous CO_2 reduc-

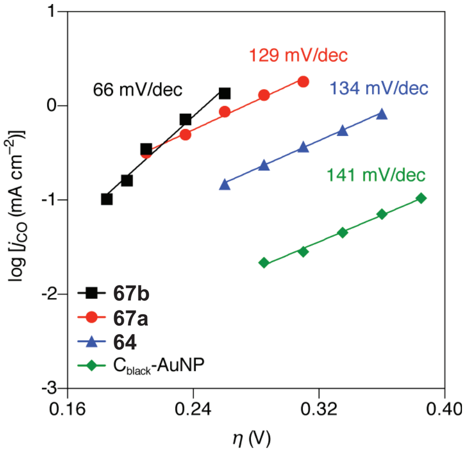

Figure 4.6: Tafel study of CO_2 reduction by GNR- and C_{black}-AuNP composite materials. A Tafel analysis shows the CO_2 reduction behavior of AuNP composites with **62** (blue triangles) and **65a** (red circles). Tafel slopes are comparable to that of the C_{black} (green diamonds) composite, indicating no shift in the mechanism of CO_2 reduction for those materials. For the **66b** composite (black squares), however, the Tafel slope is markedly different, indicating that the catalytic environment created by the support material changed the mechanism of CO_2 reduction at the AuNP surface.

tion by AuNPs.[131,169] Composites made from both GNRs **62** and **65a**, although delivering greater overall current, exhibit similar Tafel slopes to that of the C_{black} composite, indicating that the mechanism for CO_2 reduction is unchanged for these materials. In contrast, the Tafel slope for the composite made with GNR **65b** is only 66 mV/decade, suggesting a change in the rate-limiting step, and thus a significant change in the overall electrocatalytic mechanism. The Tafel slope observed for the ester-functionalized GNRAuNP composite is consistent with a pre-equilibrating oneelectron transfer followed by a rate-limiting chemical step.[117,194,195] These data suggest that an interaction between the reactant and the introduced methyl carboxylates stabilizes the transition statechanging the mechanism and leading to the increased activity observed for this composite. This experiment serves as primary evidence that nanoparticle electrocatalysis is responsive to the immediate catalytic environment created by the support material, and supports the assertion that the chemical tunability of a bottom-up synthesized support material can greatly improve catalytic performance.

4.2 SnO_2 Nanoparticles as Anode Material in Lithium Ion Batteries

In addition to CO_2 reduction as previously discussed, an alternative use of inorganic nanoparticles is for use as anode materials for lithium ion batteries (LIBs).[196–201] Similar to the pre-

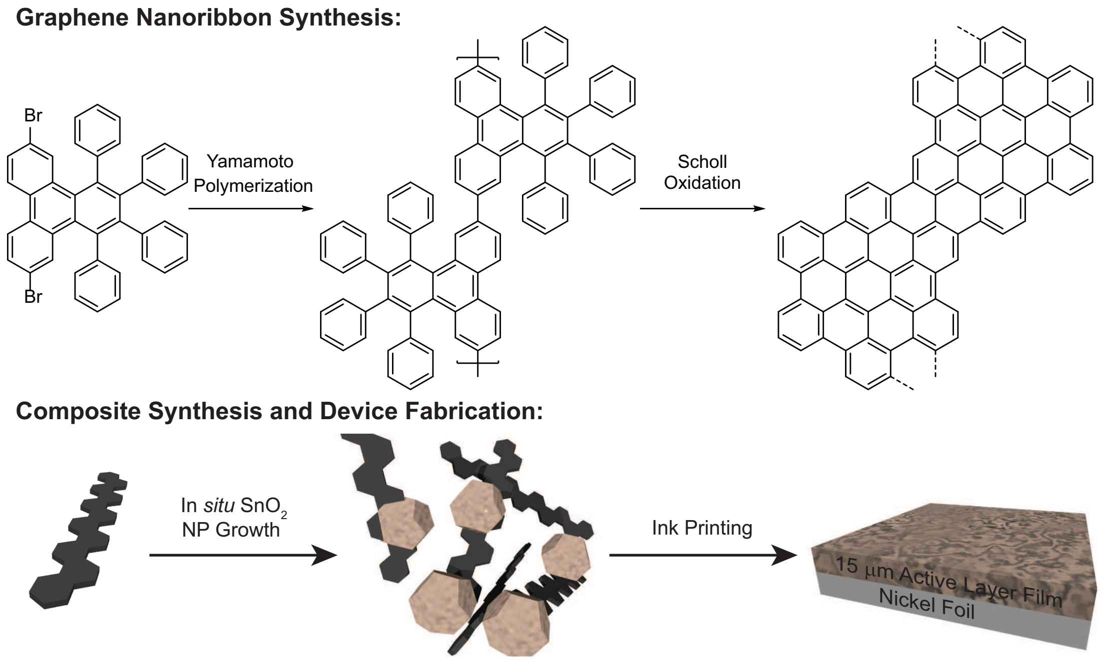

Scheme 4.2: Bottom-up synthesis of narrow GNRs from small molecule precursors and device fabrication.

vious case, stabilizing the nanoparticles during the harsh working conditions is a crucial and challenging issue for which GNRs are fit to address. For lithium ion batteries in particular, the support material and its defect structure have been shown to play a major role in device performance, inspiring us to move towards a next-generation graphitic support material.

SnO_2 batteries have been the subject of longstanding interest because of their high theoretical Li^+ storage capacity ($\sim$ 1480 mAh/g), low cost, material abundance, and low charge/discharge potential vs. Li^+/Li.[202–206] However, they are beset by stability challenges of the sort which support materials are best suited to address; in the process of alloying lithium (overall reaction $SnO_2 + 8.4\ Li \rightarrow Li_2O + Li_{4.4}Sn$), the material undergoes volume expansion of as much as 360%. This frequently leads to pulverization of the tin material, disrupts the stability of the solid electrolyte interphase (SEI) layer, saps faradaic efficiency, and eventually leads to loss of electrical contact and device function.[204,205,207–211] As such, SnO_2 batteries have been the subject of a great deal of research into graphitic support materials, which finds that defects, edges and dopant atoms, play an important role in battery performance. Defect sites have been shown to play a key role not only in storing lithium directly, but also in immobilizing tin nanoparticles, controlling nanoparticle growth, facilitating mass transport, and contributing to composite flexibility.[212–215] Unfortunately, modern support materials introduce defects by harsh chemical treatment or pyrolysis, with minimal control over defect concentration or morphology. Such an approach limits detailed investigation of defects role and inhibits rational design of improved support materials. GNRs, with their high edge to surface ratio and precise, synthetically controlled structure, meet this challenge to a degree unparalleled by other graphitic materials.[216]

We therefore synthesized a composite of SnO_2 nanoparticles grown in-situ on a support of bottom-up synthesized GNRs, and investigated it as an anode material for LIBs. Performance of the material was characterized by galvanostatic cycling, which revealed a high first charge capacity of 1233 mAh/g, indicating excellent transport of Li through the material. The composite material displayed coulombic efficiency as high as 98% after 20 cycles, with stable capacity exceeding 900 mAh/g together with strong rate capability. In addition, when the GNR-SnO_2 composite material was tested in a more limited potential range to isolate the performance of lithium alloying, the composite exhibited exceptional stability performance together with high capacity, coulombic efficiency and rate capability. These results demonstrate narrow GNRs suitability as a nanoparticle support material for battery applications.

Atomically precise chevron-type GNRs **62** were synthesized as discussed in the previous section (Figure 4.1). The SnO_2 nanoparticles were synthesized in-situ by hydrolysis of $SnCl_2$ in the presence of a surfactant-supported aqueous suspension of GNRs, followed by annealing in air. Powder X-ray diffraction (PXRD) of the composite (Figure 4.7A) confirmed the formation of nanocrystalline SnO_2, with average crystal size of 3.9 nm as calculated by the Scherrer equation. Raman spectroscopy of the GNR/SnO_2 composite (Figure 4.7B) revealed the characteristic peaks of narrow GNRs, including D and narrow G bands, together with the higher order 2D, D+D, and 2D peaks, indicating preservation of GNR structural integrity during nanoparticle synthesis. X-ray photoelectron spectroscopy (XPS) of the electrode (Figure 4.7C) shows elemental composition of the composite used in cell production, including prominent peaks corresponding to SnO_2 and graphitic carbon, and notably indicating the complete removal of residual Ni and Fe from the GNR synthesis. Thermogravimetric analysis (TGA) indicated that the composite was comprised of 69% SnO_2 by mass, consistent with the expected mass balance and suggesting complete incorporation of the GNRs.

Figures 4.8A and B show SEM micrographs for the GNR-SnO_2 nanocomposite under different, highlighting the rough microsctructure of the GNR composite, with SnO_2 nanoparticles dispersed throughout the larger composite structure. Following synthesis, the GNR/SnO_2 composite was wet ball milled, mixed with carbon black (8 wt%) and PVDF binder (10 wt%), and printed on a nickel current collector foil to give an electrode with thickness of $\sim 15\ \mu$m. SEM of the electrode surface (Figure 4.8C) illustrates its smooth morphology, a product of the ball milling done prior to printing. Electrodes prepared without this milling step appeared far rougher by SEM, and exhibited inferior battery performance (Figure 5.9). TEM of the composite (Figure 4.8D) indicated the SnO_2 consists of discrete nanoparticles with an average size of 4–5 nm, and confirmed they are well dispersed within aggregates of GNR. This structure, with nanoparticles immobilized within aggregates of flexible GNRs, is ideal for stabilizing nanoparticles and accommodating their volume expansion while also facilitating Li mass transport to the SnO_2 surface.

To gain an initial understanding of lithium storage by the GNR-SnO_2 nanocomposite, we performed cyclic voltammetry (CV) for the first three cycles between 0.005 and 3.0 V vs.

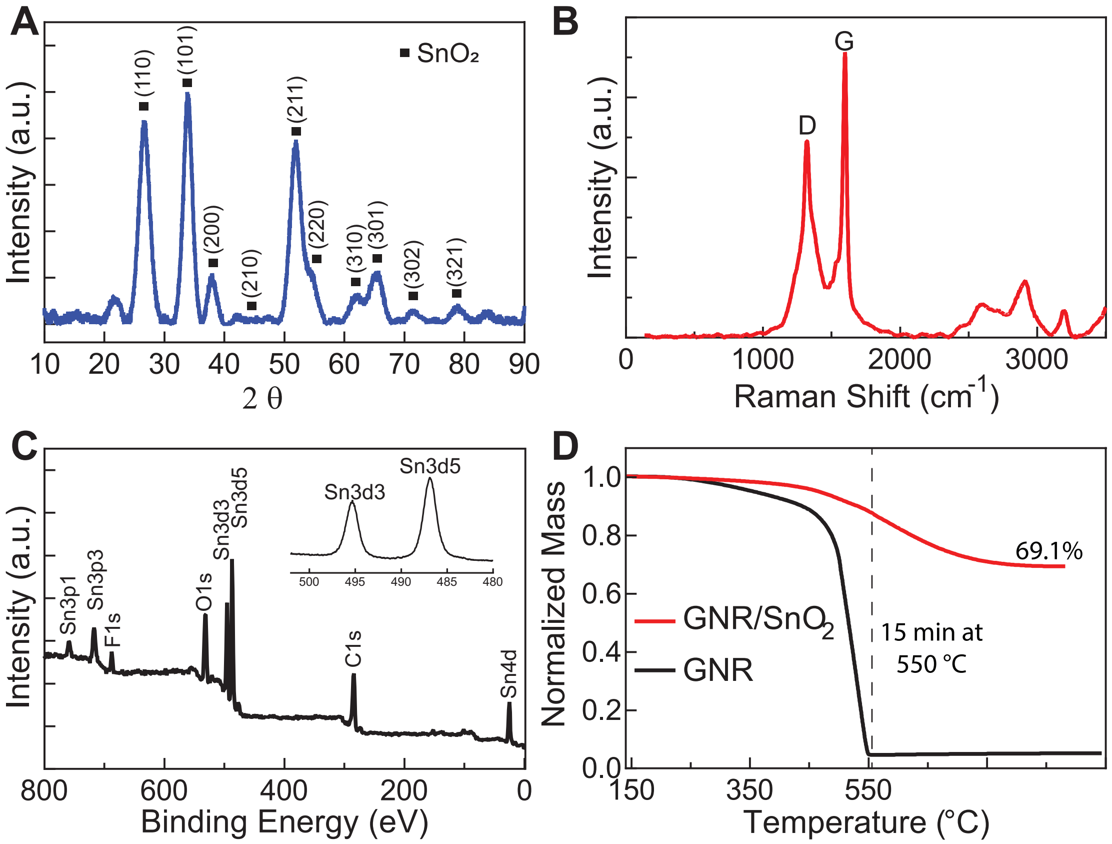

Figure 4.7: (A) XRD pattern of the GNR/SnO_2 nanocomposite. The particle size estimated using the Scherrer equation was 3.9 nm. (B) Raman spectroscopy of the GNR/SnO_2 composite exhibits the characteristic signals of narrow GNRs. (C) XPS spectroscopy of printed GNR/SnO_2 nanocomposite electrode, including prominent signals characteristic of SnO_2. (D) TGA under air of the GNR/SnO_2 composite (red) and GNRs alone (black) using a 20 °C min^{-1} ramp to 550 °C followed by 15 minutes at that temperature.

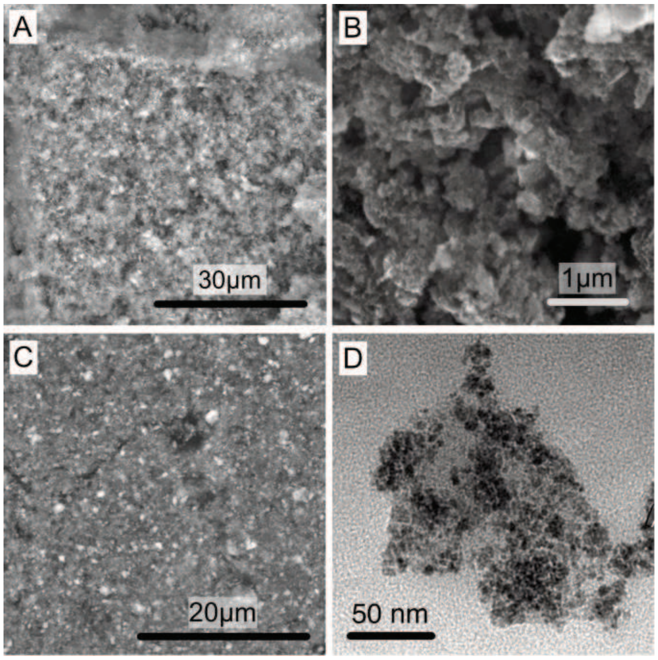

Figure 4.8: (A, B) SEM micrographs of the GNR/SnO_2 nanocomposite under different magnification. (C) SEM micrograph of the electrode prepared with GNR/SnO_2 nanocomposite with carbon black as conductive additive and PVDF as binder. (D) TEM micrograph of the GNR/SnO_2 nanocomposite.

Li^+/Li (Figure 4.9A, 0.1 mV s^{-1}). When SnO_2 is discharged in presence of a lithium source, it is known to reduce in a two-step process:

$$SnO_2 + 4\,Li^+ + 4e^- \rightarrow Sn + 2\,Li_2O \tag{4.1}$$

$$Sn + 4.4Li^+ + 4.4e^- \rightarrow Li_{4.4}Sn \tag{4.2}$$

In bulk SnO_2, the conversion of SnO_2 to Sn and Li_2O (Eq. 4.1) is irreversible, but the reaction is reversible if nanocrystals of SnO_2 are used the starting material. For our GNR composite, the first cycle in the cathodic direction exhibits a reaction up to 1.0 V corresponding to Equation 4.1, as well as the formation of a solid electrolyte interphase (SEI) layer. In the second cycle, the broad peak due to formation of the SEI layer disappeared, indicating the formation of a stable SEI layer during the first cycle. The rapid formation of a stable SEI is a crucial property often associated with graphene, and the ability of the GNR composite to maintain the SEI through multiple expansive cycles demonstrates its functionality as a flexible support material.

Below 1.0 V in CV of the GNR-SnO_2 nanocomposite, we observe current corresponding to Equation 4.2, the alloying of Sn with Li^+ to form $Li_{4.4}Sn$. The peak at 0.10 V can therefore

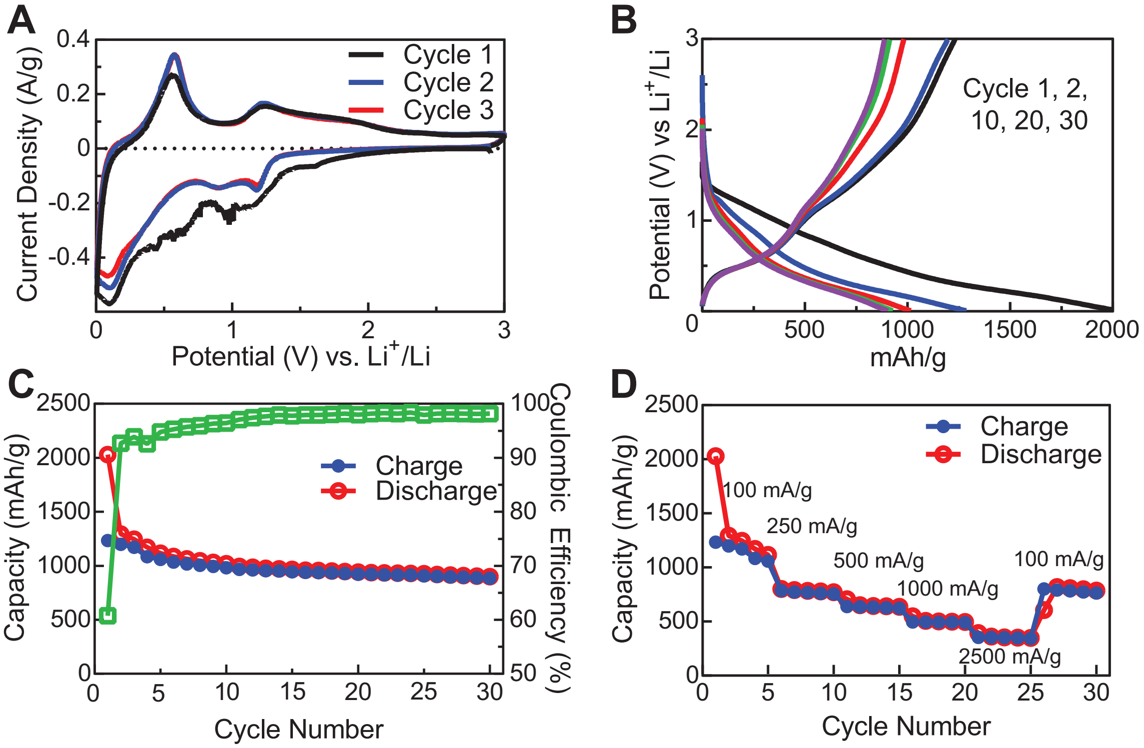

Figure 4.9: (A) Three cyclic voltammetry curve of GNR/SnO_2 nanocomposite between 3.0 to 0.005 V vs. Li^+/Li at 0.1 mV/s. (B) Galvanostatic charge/discharge curves and (C) charge/discharge capacity of GNR/SnO_2 nanocomposite cycled between 3.0 and 0.005 V vs. Li^+/Li at 100 mAh/g for 30 cycles. (D) Capacity retention of the electrode cycled between 3.0 and 0.005 V vs. Li^+/Li at 100, 250, 500, 1000, and 2000 mA/g.

be ascribed to the formation of $Li_4 \cdot 4\,Sn$. Recent studies have shown that the formation of Li_2O continues until the electrode reaches ∼0 V vs. Li^+/Li, and Sn formed during this process alloys with Li as soon as it is formed.[211,217] In the anodic direction, the peaks at 0.57 and 1.24 V are assigned to the delithiation of Li_xSn, and the reconversion of Sn to SnO_2, respectively. The peak at 1.24 V and the non-zero current between 1.5 to 3.0 V indicate that the reaction (4.1) is reversible to some extent. In later cycles, the new peaks at 1.24 and 0.87 V are can be ascribed to the conversion of SnO_2 to Sn, and alloying of Sn, respectively. The location of the peaks for the formation of $Li_{4.4}Sn$ alloy, dealloying of $Li_{4.4}Sn$ to Sn and the conversion of Sn to SnO_2 remained constant. The third cycle overlapped with the second cycle, demonstrating excellent reversibility of the GNR-SnO_2 nanocomposite.

To better understand the full lithium storage capabilities of the GNR-SnO_2 nanocomposite, we undertook galvanostatic charge/discharge cycling experiments between 0.005 to 3.0 V vs. Li^+/Li (Figure 4.9C, 100 mA g^{-1}). The first cycle discharge and charge capacities of the GNR/SnO_2 electrode were ∼2028.9 and ∼1233 mAh/g, respectively, corresponding to a coulombic efficiency (CE) of 60.8%. The loss in capacity during the first cycle was due to the consumption of lithium ions during formation of the SEI layer. The columbic efficiency increased to 97% within 10 cycles, and exceeded 98% after 20 cycles. The high first cycle charge capacity of ∼1233 mAh/g indicate that both reaction (4.1) and (4.2) are taking part in storage, as it exceeds the theoretical limit of either individually. The synergistic effect between nano-sized SnO_2 particles and bottom up synthesized graphene nanoribbons with high edge-to-surface ratio facilitated the conversion of Sn to SnO_2 and prevented aggregation during cycling, maintaining the few-nanometer sized NPs and thus allowing both reaction (4.1) and (4.2) to take part in reversible Li ion storage. Capacity of the electrode stabilized to ∼961 mAh/g after 10 cycles and the capacity at the end of 30 cycle was ∼900 mAh/g. Additionally, the composite showed excellent rate capability of 1170, 767, 663, 502 and 360 mAh/g at 100, 250, 500, 1000 and 2000 mA/g, respectively (Figure 4.9D). In Figure 4.9B we see that the charging curve up to ∼1.0 vs. Li^+/Li lay on the same plane demonstrating excellent reversibility of the alloying/dealloying process. The loss in capacity during initial cycles is due to incomplete conversion of Sn to SnO_2.

While taking advantage of the Li^+ storing reactions of both Eq. 4.1 and 4.2 maximizes reversible storage capacity, it requires a wide voltage range (3.0 to 0.005 V vs Li^+/Li), a full cell making use of both reactions together with a typical high voltage transition metal oxide based cathode would have to be discharged below 1 V, well below the input battery voltage of most consumer electronic devices. For this reason, we chose to focus on a cell using only reaction 4.2, the alloying and de-alloying of Sn with Li; because this process takes place between 0 and 1.2 V vs Li^+/Li, a full cell making use of this reaction only would operate at a much more desirable voltage. Furthermore, we find the GNR-SnO_2 nanocomposite displays exceptional stability behavior when cycled in this potential range. Figures 4.10A and B show the galvanostatic charge/discharge curves and charge/discharge capacities of GNR/SnO_2 nanocomposite cycled between 0.005 to 1.2 V vs. Li^+/Li for 30 cycles. The first cycle charge capacity of the electrode was ∼601 mAh/g, and more than 90% of this capacity is retained after 30 cycles. The columbic efficiency of the electrode was above 98% after 15 cycles. Notably, although limiting the electrode to the alloying/dealloying process of course limits its capacity, it still exhibits a capacity higher than the theoretical limit of a conventional graphite electrode (∼372 mAh/g), and with excellent stability. The charge/discharge curves lay on the same plane, indicating a highly reversible process. (Figure 4.10B). The composite showed excellent rate capability of 600, 492, 400, 324 and 245 mAh/g at 100, 250, 500, 1000 and 2000 mA/g, respectively (Figure 4.10C). Figure 4.10D shows the galvanostatic charge/discharge capacity of the electrode cycled at 100 mA/g for 25 cycles then at 250 mA/g for 125 cycles. The capacity at the start of cycling at 250 mA/g was ∼497 mAh/g and at the end of 125 cycles, the capacity was ∼458 mAh/g, demonstrating excellent capacity retention when the electrode was operating between 0 to 1.2 V.

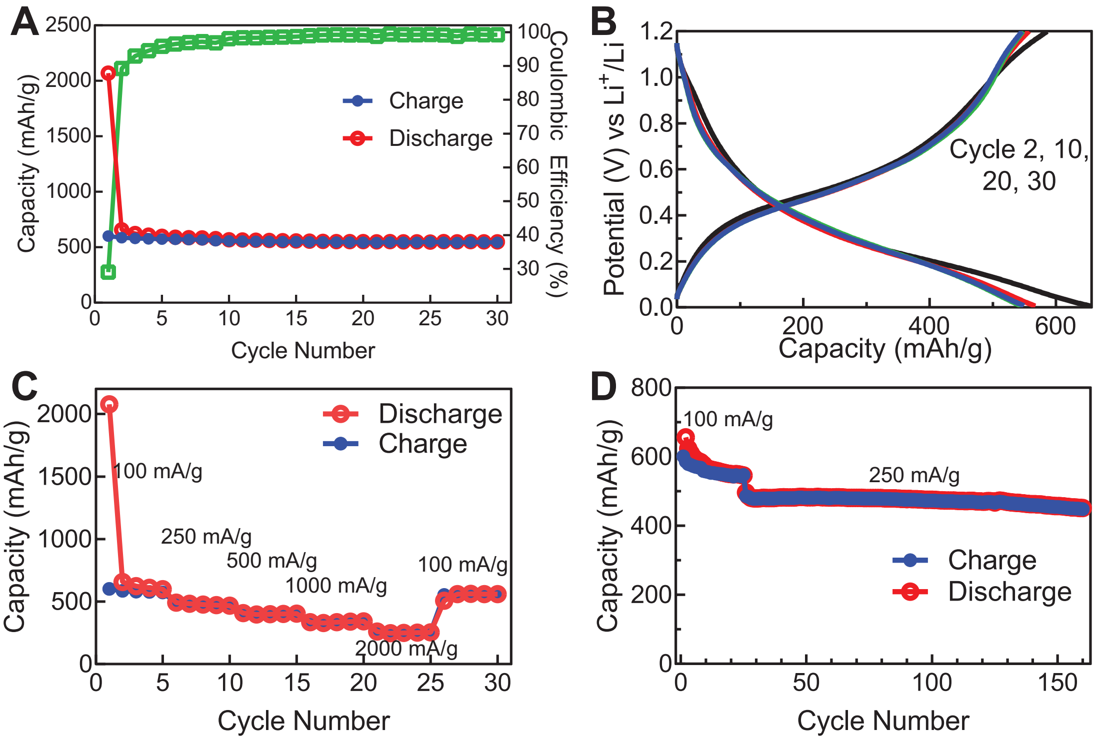

Figure 4.10: Galvanostatic charge/discharge curves (A) and charge/discharge capacity (B) of GNR/SnO_2 nanocomposite cycled between 1.2 and 0.005 V vs. Li^+/Li at 100 mA/g for 30 cycles, respectively. (C) Capacity retention of the electrode cycled between 1.2 and 0.005 V vs. Li^+/Li at 100, 250, 500, 1000 and 2000 mA/g. (D) Charge/discharge capacity of GNR/SnO_2 nanocomposite cycled between 1.2 and 0.005 V at 100 mA/g and 250 mA/g.

Chapter 5

Supporting Information

5.1 Materials and General Methods

Unless otherwise stated, all manipulations of air and/or moisture sensitive compounds were carried out in oven-dried glassware, under an atmosphere of Nitrogen. All solvents and reagents were purchased from Alfa Aesar, Spectrum Chemicals, Acros Organics, TCI America, and Sigma-Aldrich and were used as received unless otherwise noted. Organic solvents were dried by passing through a column of alumina and were degassed by vigorous bubbling of N_2 through the solvent for 20 min. Flash column chromatography was performed on SiliCycle silica gel (particle size 4063 μm). Thin layer chromatography was carried out using SiliCycle silica gel 60 ÅF-254 precoated plates (0.25 mm thick) and visualized by UV absorption. All ^{1}H and ^{13}C NMR spectra were recorded on a Bruker AV-600, AV-500, DRX-500, AVB-400, AVQ-400, or AV-300 spectrometer and are referenced to residual solvent peaks ($CDCl_3$ ^{1}H NMR = 7.26 ppm, ^{13}C NMR = 77.16 ppm; CD_2Cl_2 ^{1}H NMR = 5.32 ppm, ^{13}C NMR = 53.84 ppm). ESI mass spectrometry was performed on a Finnigan LTQFT (Thermo) spectrometer in positive ionization mode. Gel permeation chromatography (GPC) was carried out on a LC/MS Agilent 1260 Infinity set up with a guard and two Agilent Polypore 300 x 7.5 mm columns at 35 °C. All GPC analyses were performed on a 0.2 mg/mL solution of polymer in chloroform. An injection volume of 25 μL and a flow rate of 1 mL/min were used. Calibration was based on narrow polydispersity polystyrene standards ranging from Mw = 100 to 4,068,981. UV-Vis spectroscopic measurements were conducted in a Varian Cary 50 spectrophotometer (Agilent, USA). 3-bromobenzil, ^{13}C-$MePPh_3I$,[218] 5-phenyldipyrromethane,[219] 4-(1,3-dioxolan-2-yl)benzaldehyde,[220] 5,15-bis(4-ethynlphenyl)-10,20-diphenyl-21H,23H-porphine[221] and 3-bromobenzil[91] were synthesized according to literature procedures.

5.2 Synthetic Procedures

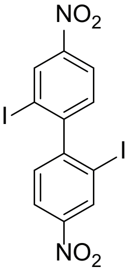

1

2,2'-Diiodo-4,4'-dinitrobiphenyl (**1**): A 100 mL flask was charged with 4,4'-dinitrobiphenyl (1.03 g, 4.23 mmol), $NaIO_3$ (0.87 g, 4.38 mmol), and H_2SO_4 (10 mL). The reaction mixture was heated to 110 °C for 2 h. The reaction mixture was poured over crushed ice and the precipitate filtered and collected. A 100 mL flask was charged with NaI (1.85 g, 12.355 mmol), CuI (0.10 g, 0.54 mmol), and DMF (10 mL). The previously collected precipitate was added to this reaction mixture and heated to 110 °C for 5 h. The reaction mixture was poured into water and extracted with EtOAc. The combined organics were dried with $MgSO_4$, filtered, and the solvent was removed under reduced pressure. Recrystallization from EtOH yielded **1** as yellow needles (1.06 g, 2.131 mmol, 50%). ^{1}H NMR (400 MHz, $CDCl_3$, 22 °C): δ = 8.82 (s, 2 H), 8.34 (d, J = 10.7 Hz, 2 H), 7.36 (d, J = 8.4 Hz, 2 H) ppm. ESI-HR-MS (m/z): calcd for $C_{12}H_6N_2O_4I_2$ $[M]^+$ 495.8417, found 495.8424. Matches previous reports.**??**

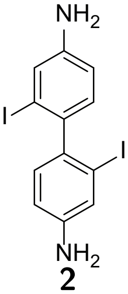

2

2,2'-Diiodo-4,4'-diaminobiphenyl (**2**): A 250 mL roundbottom flask was charged with **1** (3.26 g, 6.57 mmol), $SnCl_2{\cdot}2\,H_2O$ (17.94 g, 79.5 mmol), EtOH (40 mL), and conc. HCl (37 mL). The reaction mixture was heated to 40 °C for 1 h. The reaction mixture was basified with 200 mL 6 M NaOH and extracted with Et_2O. The combined organics were dried with $MgSO_4$, filtered, and the solvent was removed under reduced pressure. Recrystallization from EtOH yielded **2** as yellow needles (1.88 g, 4.32 mmol, 66%). ^{1}H NMR (300 MHz, $CDCl_3$, 22 °C): δ = 7.25 (d, J = 2.4 Hz, 2 H), 6.94 (d, J = 8.2 Hz, 2 H), 6.69 (dd, J = 8.1 Hz, 2.2 Hz, 2 H), 3.71 (s, 4 H) ppm; ESI-HR-MS (m/z): calcd for $C_{12}H_{11}N_2I_2$ $[M]^+$ 436.9012, found 436.9006. Matches previous reports.**??**

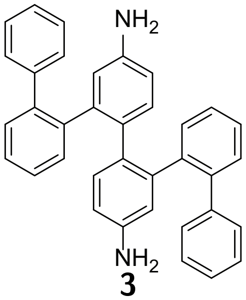

3

[1,1’:2’,1”:2”,1”’:2”’,1””:2””,1””’-Sexiphenyl]-4”’,5”-diamine (**3**): An oven dried 50 mL Schlenk roundbottom flask was charged with **2** (315 mg, 0.687 mmol), 2-biphenylboronic acid (302 mg, 2.53 mmol, 2.2 eq), toluene (8 mL), and 1M K_2CO_3 (aq.). The reaction mixture was sparged with N_2 for 1 h, at which point $Pd(PPh_3)_4$ (99 mg, 0.086 mmol, 0.13 eq) was added under flow of N_2. A reflux condenser was attached, and the mixture was stirred at 100 °C under N_2 for 4 h. After cooling to 22 °C the mixture was filtered and the filtrate was diluted with CH_2Cl_2 (10 mL) and H_2O (10 mL). The mixture was extracted with CH_2Cl_2 (2 × 10 mL). The combined organics were washed with sat. $NaHCO_3$ (10 mL), H_2O (10 mL), dried with $MgSO_4$, filtered, and the solvent removed under reduced pressure. Column chromatography (SiO_2: 4:1 hexanes/EtOAc) yielded **3** (91 mg, 0.19 mmol, 27%) as a colorless solid. ^1H NMR (500 MHz, $CDCl_3$, 22 °C): δ = 7.23–7.08 (m, 8H), 7.08–6.91 (m, 8H), 6.63 (d, J=6.1 Hz, 2H), 6.42 (s, 2H), 6.31 (d, J=6.4 Hz, 2H), 6.13 (d, J=6.6 Hz, 2H), 3.51 (s, br, 4H) ppm; ^{13}C $\{^1H\}$ NMR (125 MHz, $CDCl_3$, 22 °C): δ = 143.6, 141.5, 140.5, 140.2, 132.3, 131.6, 129.3, 128.7, 127.2, 126.0, 125.4, 118.5, 117.4, 114.4 ppm; ESI-HRMS (m/z): calcd for $C_{36}H_{29}N_2$ $[M+H]^+$ 489.2325, found 489.2327.

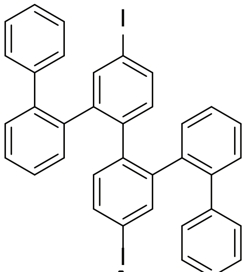

4

4”’,5”-Diiodo-1,1’:2’,1”:2”,1”’:2”’,1””:2””,1””’-sexiphenyl (**4**): A 50 mL roundbottom flask was charged with **3** (91 mg, 0.19 mmol), H_2O (10 mL), and H_2SO_4. The reaction mixture was cooled to 5 °C and a solution of $NaNO_2$ (30 mg, 0.43 mmol, 2.3 eq) in H_2O (1 mL) was added dropwise over 5 min, and stirred at 5 °C for 45 min. To this was added KI (128 mg, 0.77 mmol, 4.2 eq) portionwise over 5 min and the reaction mixture was stirred at 22 °C for 5 h. The mixture was then extracted with EtOAc (2 × 15 mL). The combined organics were washed with 2M NaOH (30 mL) and brine (30 mL), dried with $MgSO_4$, filtered, and the solvent was removed under reduced pressure. Column chromatography (SiO_2: 1:2 hexanes/EtOAc) yielded **4** (33 mg, 0.047 mmol, 25%). ^1H NMR (500 MHz, $CDCl_3$, 22 °C): δ = 7.47 (s, 2H), 7.24–7.14 (m, 4 H), 7.13–7.02 (m, 8H), 7.02–6.92 (m, 6H), 6.51–6.40 (m, 4H) ppm; ^{13}C {^{1}H} NMR (125 MHz, $CDCl_3$, 22 °C): δ = 141.9, 141.2, 139.4, 139.2, 138.1, 136.5, 132.9, 131.5, 131.1, 129.9, 128.8, 128.0, 127.2, 126.1, 92.3 ppm; EI-HRMS (*m/z*): calcd for $C_{36}H_{24}I_2$ $[M]^+$ 709.9968, found 709.9959.

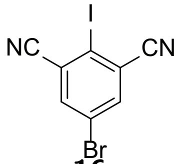

16

5-Bromo-2-iodoisophthalonitrile (**16**): A 100 round bottom flask was charged with **15** (5.00 g, 19.7 mmol) in sulfuric acid (22 mL). The reaction mixture was heated to 50 °C. N-bromosuccinimide (3.89 g, 21.9 mmol) was added portionwise over 3 min and the reaction mixture stirred for 10 min at 50 °C. The reaction mixture was poured over ice/water (200 mL), filtered, and the precipitate washed with water. Recrystallization from EtOAc (500 mL) yielded **16** (4.12 g, 12.4 mmol, 63%) as a colorless crystalline solid. ^{1}H NMR (400 MHz, $CDCl_3$, 22 °C): δ = 7.89 (s, 2H) ppm; ^{13}C {^{1}H} NMR (151 MHz, $CDCl_3$, 22 °C): δ = 140.0, 124.9, 122.9, 117.1, 101.8 ppm; EI-HRMS (*m/z*): calcd for $C_8H_2N_2Br_1I_1$ $[M]^+$ 331.8446, found 331.8450.

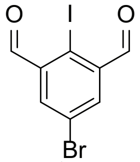

17

5-Bromo-2-iodoisophthalaldehyde (**17**): A 500 mL round bottom flask was charged with **16** (4.65 g, 14.0 mmol) in formic acid (210 mL). Raney-Nickel (50% slurry in H_2O, 17 mL, 136 mmol) was added quickly via syringe. The reaction mixture was heated to 100 °C and stirred for 1.5 h. The reaction mixture filtered hot and the grey precipitate washed with CH_2Cl_2. The filtrate was diluted with H_2O, and extracted with CH_2Cl_2 (3 × 200 mL). The combined organic phases were washed with saturated aqueous NaCl (400 mL), dried over $MgSO_4$, and the solvent removed under reduced pressure. Column chromatography (SiO_2; 40% CH_2Cl_2 in hexanes) yielded **17** (1.06 g, 3.13 mmol, 22%) as a colorless solid. ^{1}H NMR (500 MHz, $CDCl_3$, 22 °C): δ = 10.25 (s, 2H), 8.18 (s, 2H) ppm; ^{13}C {^{1}H} NMR (150 MHz, $CDCl_3$, 22 °C): δ = 193.5, 138.1, 137.4, 124.5, 103.3 ppm; EI-HRMS (*m/z*) cald for $C_8H_4O_2IBr$ $[M]^+$ 337.8439, found 337.8438.

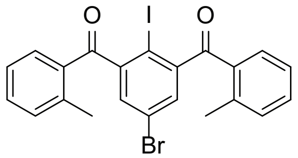

18

(5-Bromo-2-iodo-1,3-phenylene)bis(o-tolylmethanone) (**18**): A 200 mL Schlenk round bottom flask was charged under N_2 with **17** (1.01 g, 2.98 mmol), in dry THF (35 mL). The reaction mixture was cooled to −78 °C. o-tolylmagnesium chloride (1.0 M in THF, 6.5 mL, 6.5 mmol) was added dropwise over 5 min and the reaction mixture stirred for 16 h with gradual warming to 24 °C. The reaction mixture was acidified with 1 M aqueous HCl (5 mL), diluted with H_2O (100 mL) and extracted with CH_2Cl_2 (4×100 mL). The combined organic phases were washed with saturated aqueous NaCl (200 mL), dried over $MgSO_4$, and the solvent removed under reduced pressure. To the crude reaction product was added CH_2Cl_2 (500 mL), celite (2.43 g), and PCC (2.16 g, 10.0 mmol). The reaction mixture was stirred at 24 °C for 4 h. The reaction mixture was filtered and the brown precipitate washed with CH_2Cl_2 (500 mL), and the combined filtrates concentrated under reduced pressure. Column chromatography (SiO_2; 1:1 hexanes/CH_2Cl_2) yielded **18** (1.46 g, 2.81 mmol, 94%) as a colorless solid. ^{1}H NMR (500 MHz, $CDCl_3$, 22 °C): δ = 7.50 (s, 2H), 7.50-7.46 (m, 2H), 7.36 (dd, J=7.8, 1.3 Hz, 4H), 7.25 (t, J=7.6 Hz, 2H), 2.67 (s, 6H) ppm; ^{13}C {^{1}H} NMR (150 MHz, $CDCl_3$, 22 °C): δ = 197.5, 148.7, 141.2, 134.5, 133.1, 132.7, 132.5, 132.2, 126.0, 122.9, 88.7, 21.9 ppm; EI-HRMS (m/z): calcd for $C_{22}H_{16}O_2Br_1I_1$ $[M]^+$ 517.9378. found 519.9380.

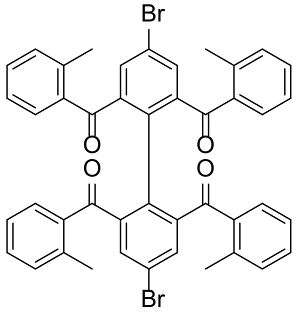

19

(4,4'-Dibromo-[1,1'-biphenyl]-2,2',6,6'-tetrayl)tetrakis(o-tolylmethanone) (**19**): A 5 mL Schlenk tube was charged under N_2 with **18** (78 mg, 0.15 mmol) and copper powder (70 mg, 1.1 mmol), in DMF (0.4 mL). The reaction mixture was heated to 120 °C and stirred for 14 h. The reaction mixture was cooled to 24 °C and filtered through celite, washing with EtOAc. The filtrate was washed with 0.5 M aqueous HCl (2 × 5 mL), and saturated aqueous NaCl, dried over $MgSO_4$, and the solvent removed under reduced pressure. Column chromatography (SiO_2; 1:1 hexanes/toluene) yielded **19** (53 mg, 0.068 mmol, 91%) as a colorless solid. ^{1}H NMR (400 MHz, $CDCl_3$, 22 °C): δ = 7.61 (s, 4H), 7.45 (d, J=7.7 Hz, 4H), 7.30 (t, J=7.5 Hz, 4H), 7.20 (d, J= 7.6 Hz, 4H), 7.08 (t, J=7.6 Hz, 4H), 2.34 (s, 12H) ppm; ^{13}C {^{1}H} NMR (150 MHz, $CDCl_3$, 22 °C): δ = 196.8, 140.6, 139.2, 138.6, 137.7, 136.9, 131.4, 131.2, 130.9, 125.2, 120.1, 20.29 ppm; ESI-HRMS (m/z): calcd for $C_{44}H_{32}O_4Br_2$ $[M]^+$ 782.0667, found 782.0658.

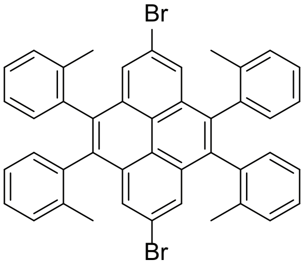

20

2,7-Dibromo-4,5,9,10-tetra-o-tolylpyrene (**20**): A 100 Schlenk round bottom flask was charged under N_2 with **19** (362 mg, 0.461 mmol), and phosphorus pentasulfide (2.27 g, 5.1 mmol), in dry o-xylene (20 mL). A reflux condenser was attached and the reaction mixture was heated to 150 °C and stirred for 48 h. The reaction mixture was cooled to 22 °C and filtered through celite, washing with toluene. The filtrate was concentrated under reduced pressure. Column chromatography (SiO_2; 9:1 hexanes/CH_2Cl_2) yielded **20** (120 mg, 0.17 mmol, 36%) as a colorless solid. ^{1}H NMR (600 MHz, CD_2Cl_2, 22 °C): δ = 7.71 (s, 4H), 7.28–7.24 (m, 8H), 7.16–7.12 (m, 8H), 7.15–7.03 (m, 12H) ppm; ^{13}C {^{1}H} NMR (126 MHz, $CDCl_3$, 22 °C): δ = 138.2, 137.7, 136.6, 132.6, 130.2, 130.0, 128.9, 128.0, 127.4, 125.8, 125.2, 20.6, 20.5 ppm; ESI-HRMS (m/z): calcd for $C_{44}H_{32}Br_2$ $[M]^+$ 718.0871, found 718.0872.

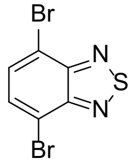

22

4,7-Dibromobenzo[c][1,2,5]thiadiazole (**22**): A 25 mL roundbottom flask was charged with a magnetic stirbar, benzo[*c*][1,2,5]thiadiazole (1.00 g, 7.34 mmol), NBS (2.75 g, 15.5 mmol, 2.1 eq), and conc. H_2SO_4 (10 mL) under air. The mixture was stirred at 60 °C for 3 h. After cooling room temperature, the reaction was quenched with aq. $Na_2S_2O_3$ (100 mL), extracted with toluene (3×100 mL), the combined organics were dried with $MgSO_4$, filtered, and the solvent removed to yield **22** as an off-white solid (2.09 g, 7.1 mmol, 97%). ^{1}H NMR (400 MHz, $CDCl_3$, 22 °C): δ = 7.73 (s, 2H) ppm; ^{13}C {^{1}H} NMR (126 MHz, $CDCl_3$, 22 °C): δ =153.1, 132.5, 114.0 ppm; EI-HRMS (m/z): calcd for $C_6H_2N_2S^{79}Br_1{}^{81}Br_1$ $[M]^+$ 293.8291, found 293.8289. Matches previous reports.**??**

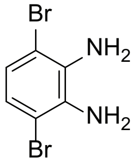

23

3,6-Dibromobenzene-1,2-diamine (**23**): An oven dried 500 mL Schlenk roundbottom flask was charged with a magnetic stirbar, **22** (2.01 g, 6.83 mmol), and EtOH (250 mL) under N_2.

The mixture was cooled to 0 °C in an ice water bath and $NaBH_4$ (4.65 g, 134 mmol, 19.6 eq) was added portionwise over 6 minutes. The mixture was stirred at 0 °C for 20 min, at which point the ice bath was removed and stirring continued under N_2 for 24 h. The mixture was then cooled to 0 °C and quenched with H_2O (150 mL). The EtOH was removed via rotavap and the mixture extracted with Et_2O (3 × 200 mL). The combined organics were dried with $MgSO_4$, filtered, and concentrated to yield **23** (1.816 g, 6.83 mmol, 100%) as an off-white solid. ^{1}H NMR (300 MHz, $CDCl_3$, 22 °C): δ = 6.84 (s, 2H), 3.89 (br, s, 4H) ppm. Matches previous reports.**??**

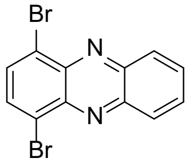

25

1,4-Dibromophenazine (**25**): A 1 L roundbottom flask was charged with a magnetic stirbar, $K_2Cr_2O_7$ (7.06 g, 24 mmol, 12 eq), H_2SO_4 (30 mL), and H_2O (270 mL). To this was added a solution of catechol (1.32 g, 12.0 mmol, 6 eq) in CH_2Cl_2 (300 mL) and the biphasic mixture was stirred vigorously for 15 min. The organic layer was transfered to a 500 mL roundbottom flask containing **23** (532 mg, 2.0 mmol) in AcOH (2 mL) and a magnetic stirbar. A reflux condensor was attached and the mixture stirred at 50 °C for 7 h. Solvent removed under reduced pressure. Column chromatography (SiO_2: CH_2Cl_2:hexanes 1:1) yielded **25** (59 mg, 0.17 mmol, 9%) as a yellow solid. ^{1}H NMR (600 MHz, $CDCl_3$, 22 °C): δ = 8.41 (dd, J=6.7, 3.4 Hz, 2H), 8.06 (s, 2H), 7.95 (dd, J=6.8, 3.4 Hz, 2H) ppm; ^{13}C {^{1}H} NMR (126 MHz, $CDCl_3$, 22 °C): δ = 144.0, 141.2, 133.4, 132.1, 129.9, 124.3 ppm; EI-HRMS (m/z): calcd for $C_{12}H_6N_2{}^{79}Br_1{}^{81}Br_1$ $[M]^+$ 337.8877, found 337.8880. Matches previous reports.**??**

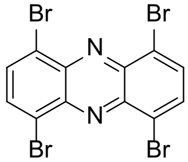

26

1,4,6,9-Tetrabromophenazine (**26**): A 25 mL roundbottom flask was charged with a magnetic stirbar, phenazine (662 mg, 3.68 mmol), and NBS (2.75 g, 15.5 mmol, 4.2 eq), and H_2SO_4 (10 mL). The mixture was stirred at 60 °C for 3 h. After cooling to 22 °C the mixture was diluted with H_2O (100 mL) and extracted with CH_2Cl_2 (3 × 100 mL). The combined organics were washed with aq. $Na_2S_2O_3$ (200 mL) and sat. NaCl (200 m), dried with $MgSO_4$, filtered, and concentrated. Column chromatography (SiO_2: CH_2Cl_2:hexanes 1:1) yielded **26** (100 mg, 0.20 mmol, 5.5%) as a yellow solid. ^{1}H NMR (600 MHz, $CDCl_3$, 22 °C): δ = 8.14 (s, 4H) ppm. ^{13}C {^{1}H} NMR (126 MHz, $CDCl_3$, 22 °C): δ = 141.6, 134.8, 124.3 ppm; EI-HRMS (m/z): calcd for $C_{12}H_4N_2{}^{79}Br_2{}^{81}Br_2$ $[M]^+$ 495.7067, found 495.7070.

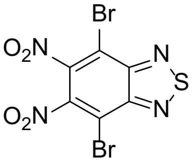

32

4,7-Dibromo-5,6-dinitrobenzo[c][1,2,5]thiadiazole (**32**): An oven dried 250 mL 2-neck roundbottom flask was charged with a magnetic stirbar and TfOH (60 mL) and cooled to 0 °C. Fuming nitric acid (6 mL) was added via needle and syringe, followed by **22** (10.14 g, 34.5 mmol) portionwise over 10 min. After stirring at 0 °C for 10 min after addition the mixture was heated to 50 °C and stirred for 21 h. After cooling to room temperature the mixture was poured carefully into 700 mL crushed ice water and filtered to give a colorless precipitate that was washed with a further 1 L of H_2O. The precipitate was suspended in and filtered from MeOH twice. Recrystallization from toluene yielded **32** as pale yellow needles (5.60 g, 14.7 mmol, 43%). $^{13}C\ \{^1H\}$ NMR (126 MHz, $CDCl_3$, 22 °C): $\delta = 155.9, 151.5, 110.4$ ppm; EI-HRMS (*m/z*): calcd for $C_6N_4O_4S^{79}Br_1{}^{81}Br_1$ $[M]^+$ 383.7987, found 383.7991. Matches previous reports.**??**

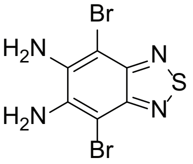

33

4,7-Dibromo-5,6-diaminobenzo[c][1,2,5]thiadiazole (**33**): A 1 L Schlenk roundbottom flask was charged with a magnetic stirbar and AcOH (500 mL) and sparged with N_2 for 38 min. A solid mixture of **32** (2.57 g, 6.73 mmol) and Fe powder (6.03 g, 108 mmol, 16 eq) was added under flow of N_2. The flask was fitted with a reflux condensor and the mixture was stirred at 100 °C for 3 h. The mixture was then poured into 1.4 L of 5% aq. NaOH and filtered. The yellow precipitate was taken up in 500 mL hot EtOAc, dried with $MgSO_4$, filtered, and the solvent removed to yield **33** as a ye llow solid (1.12 g, 3.45 mmol, 51%). GCMS (*m/z*): calcd for $C_6N_4S^{79}Br_1{}^{81}Br_1$ $[M]^+$ 323.9, found 323.9. Matches previous reports.**??**

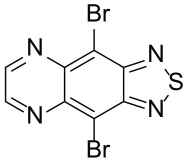

34

4,9-Dibromo-[1,2,5]thiadiazolo[3,4-g]quinoxaline (**34**): A 500 mL 2-neck roundbottom flask was charged with a magnetic stirbar, **33** (1.12 g, 3.45 mmol), EtOH (250 mL), THF (100 mL), and AcOH (20 mL) and sparged with N_2 for 15 min. Glyoxal (40 % in H_2O, 1.0 mL, 8.3 mmol, 2.4 eq) was added via needle and syringe and the mixture was stirred for 24 h. The solvents were then removed at reduced pressure and the residue taken up in EtOAc (300 mL) and washed with sat. $NaHCO_3$ (3×200 mL) and brine (200 mL). The combined organics were dried with $MgSO_4$, filtered, and the solvent removed to yield **34** as an orange solid (560 mg, 1.62 mmol, 47%). ^{1}H NMR (600 MHz, $CDCl_3$, 22 °C): $\delta = 9.03$ (s, 2H) ppm. Previously reported.**??**

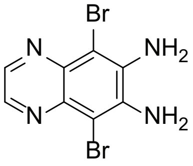

35

5,8-Dibromoquinoxaline-6,7-diamine (**35**): An oven dried 500 mL Schlenk roundbottom flask was charged with a magnetic stirbar, **34** (560 mg, 1.62 mmol), and dry Et_2O (250 mL) and sparged with N_2 for 15 min. The solution was cooled to 0 °C and solid $LiAlH_4$ (1.04 g, 27.4 mmol, 17 eq) was added portionwise. After addition the cold bath was removed and the mixture stirred at room temperature for 18 h. The reaction was quenched with sat. NH_4Cl and extracted with Et_2O (3 × 200 mL). The combined organics were dried with $MgSO_4$, filtered, and the solvent removed. Column chromatography (Al_2O_3: EtOAc:hexanes 1:1 to EtOAc) yielded **35** as a red solid (37 mg, 0.12 mmol, 7.2%). GCMS (*m/z*): calcd for $C_8H_6N_4{}^{79}Br_1{}^{81}Br_1$ $[M]^+$ 317.9, found 317.9.

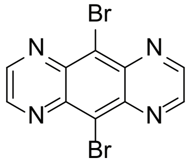

29

5,10-Dibromopyrazino[2,3-g]quinoxaline (**29**): A 50 mL Schlenk roundbottom flask was charged with a magnetic stirbar, **35** (36 mg, 0.11 mmol), and EtOH (25 mL) and sparged with N_2 for 20 min. Glyoxal (40 % in H_2O, 0.9 mL, 7.4 mmol, 68 eq) was added via needle and syringe and the solution was stirred at room temperature for 18 h. The solvent was removed at reduced pressure and the red residue was taken up in CH_2Cl_2 (20 mL) and washed with sat. $NaHCO_3$ (3 × 20 mL) and brine (20 mL). The combined organics were dried with $MgSO_4$, filtered, and the solvents removed at reduced pressure. Preparative TLC (Al_2O_3: EtOAc:hexanes 1:1) yielded **29** as an orange solid (7.5 mg, 0.022 mmol, 20%). ^{1}H NMR (300 MHz, $CDCl_3$, 22 °C): $\delta = 9.17$ (s, 4H) ppm; EI-HRMS (*m/z*): calcd for $C_{10}H_4N_4{}^{79}Br_1{}^{81}Br_1$ $[M]^+$ 339.8782, found 339.8784. Previously reported.**??**

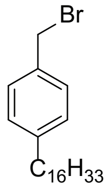

37

1-(Bromomethyl)-4-hexadecylbenzene (**37**): A 100 mL heavy wall pressure vessel was charged under N_2 with hexadecylbenzene (24.85 g, 82.1 mmol) and paraformaldehyde (3.02 g, 100.6

mmol) in acetic acid (30 mL). HBr (33% in AcOH, 24 mL) was added with stirring. The reaction mixture was stirred for 15 h at 120 °C. The reaction mixture was cooled to 24 °C and diluted with CH_2Cl_2 (150 mL). The combined organic phases were washed with saturated aqueous $NaHCO_3$ (150 mL), water (150 mL), saturated aqueous NaCl (150 mL), dried over $MgSO_4$, filtered, and concentrated on a rotary evaporator. Column chromatography (SiO_2; hexanes) followed by recrystallization from hexanes yielded **37** (14.51 g, 36.7 mmol, 45%) as a colorless solid. ^{1}H NMR (400 MHz, $CDCl_3$, 22 °C): δ = 7.30 (d, J = 7.9 Hz, 2H), 7.15 (d, J = 7.8 Hz, 2H), 4.49 (s, 2H), 2.59 (t, J = 7.8 Hz, 2H), 1.22–1.33 (m, 26H), 0.88 (t, J = 6.6 Hz, 3H) ppm; ^{13}C {^{1}H} NMR (126 MHz, $CDCl_3$, 22 °C): δ = 143.6, 135.1, 129.1, 129.0, 35.9, 34.0, 32.1, 31.5, 29.9 (2C), 29.8 (2C), 29.8 (2C), 29.7, 29.6, 29.5, 29.5, 22.9, 14.3 ppm; EI-HRMS (m/z): calcd for $C_{23}H_{39}Br$ $[M]^+$ 394.2235, found 394.2233. Matches previous report.**??**

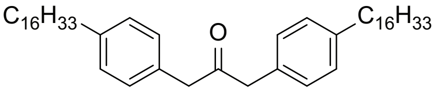

38

1,3-Bis(4-hexadecylphenyl)propan-2-one (**38**): A 150 mL heavy wall pressure vessel was charged under N_2 with NaOH (4.02 g, 100.5 mmol) and benzyltriethylammonium chloride (187.3 mg, 0.82 mmol) in water (2.3 mL). **37** (7.62 g, 19.3 mmol) and CH_2Cl_2 (57 mL) added with stirring. Reaction mixture heated to 40 °C. $Fe(CO)_5$ (1.4 mL, 10.4 mmol) was added and the reaction mixture was stirred at 40 °C for 18 h. The reaction mixture was cooled to 24 °C, diluted with CH_2Cl_2 (100 mL), and filtered through celite. The filtrate was diluted with water (100 mL) and extracted with CH_2Cl_2 (3 × 100 mL). The combined organic phases were washed with saturated aqueous saturated aqueous NaCl (200 mL), dried over $MgSO_4$, filtered, and concentrated on a rotary evaporator. Column chromatography (SiO_2; 2:1 hexanes/CH_2Cl_2), followed by recrystallization from hexanes yielded **38** (3.99 g, 6.05 mmol, 63%) as a colorless solid. ^{1}H NMR (500 MHz, $CDCl_3$, 22 °C): δ = 7.12 (d, J = 7.9 Hz, 4H), 7.05 (d, J = 7.9 Hz, 4H), 3.67 (s, 4H), 2.57 (t, J = 7.8 Hz, 4H), 1.62–1.55 (m, 4H), 1.34–1.22 (m, 52H), 0.88 (t, J = 6.9 Hz, 6H) ppm; ^{13}C {^{1}H} NMR (126 MHz, $CDCl_3$, 22 °C): δ = 206.4, 141.9, 131.3, 129.5, 128.9, 48.8, 35.7, 32.1, 31.6, 29.9 (2C), 29.8 (2C), 29.8 (2C), 29.7 (2C), 29.5, 29.5, 22.9, 14.3 ppm; EI-HRMS (m/z): calcd for $C_{47}H_{78}O$ $[M]^+$ 658.6053, found 658.6044.

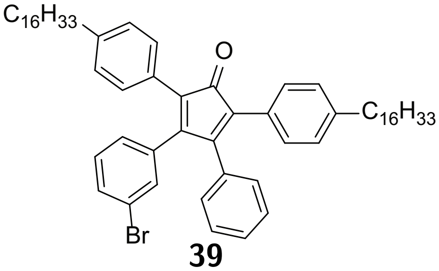

39

3-(3-Bromophenyl)-2,5-bis(4-hexadecylphenyl)-4-phenylcyclopenta-2,4-dienone (**39**): A 500 mL three neck round bottom flask with reflux condensor was charged under N_2 with **38**

(5.48 g, 8.31 mmol) 1-(3-bromophenyl)-2-phenylethane-1,2-dione (2.41 g, 8.34 mmol) and in *t*-BuOH (250 mL). The reaction mixture was heated to 80 °C. Tetraethylammonium hydroxide (20 wt% in H_2O, 2.8 mL) was added all at once. The reaction mixture was stirred at 80 °C for 50 min. The reaction mixture was cooled to 24 °C, quenched with 1M HCl (15 mL), diluted with water (150 mL) and extracted with CH_2Cl_2 (3 × 150 mL). The combined organic phases were washed with saturated aqueous NaCl (300 mL), dried over $MgSO_4$, filtered, and concentrated on a rotary evaporator. Column chromatography (SiO_2; 4:1 hexanes:CH_2Cl_2) yielded **39** (4.60 g, 5.04 mmol, 61%) as a purple solid. ^{1}H NMR (500 MHz, CD_2Cl_2, 22 °C): δ = 7.38 (d, J = 8.8 Hz, 1H), 7.28 (t, J = 7.4 Hz, 2H), 7.21 (t, J = 7.5 Hz, 2H), 7.14–7.09 (m, 5H), 7.09–7.04 (m, 5H), 6.95 (d, J = 7.1 Hz, 2H), 6.89 (d, J = 7.6 Hz, 1H), 2.61–2.53 (m, 4H), 1.62–1.56 (m, 4H), 1.34-1.24 (m, 52H), 0.88 (t, J = 6.9 Hz, 6H) ppm; ^{13}C {^{1}H} NMR (126 MHz, $CDCl_3$, 22 °C): δ = 200.7, 153.7, 152.0, 142.9, 142.6, 135.6, 133.2, 132.3, 131.4, 130.0, 129.6, 129.4, 128.7, 128.4, 128.3, 128.2, 128.1, 127.9, 127.6, 125.9, 125.1, 122.0, 35.9, 32.1, 31.4, 29.9 (2C), 29.8 (2C), 29.8 (2C), 29.7, 29.7, 29.5, 29.5, 29.5, 22.9, 14.3 ppm; EI-HRMS (*m/z*): calcd for $C_{61}H_{83}O^{79}Br$ $[M]^+$ 910.5622, found 910.5621.

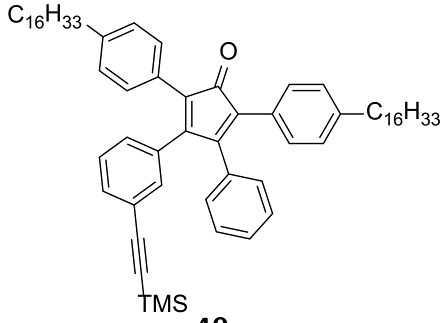

40

2,5-bis(4-Hexadecylphenyl)-3-phenyl-4-(3-((trimethylsilyl)ethynyl)phenyl)cyclopenta-2,4-dienone (**40**): A 500 mL Schlenk round bottom flask was charged under N_2 with **39** (4.53 g, 4.96 mmol) and CuI (102 mg, 0.54 mmol) in triethylamine (275 mL). The reaction mixture was degassed. Trimethylsilylacetylene (2.25 mL, 15.9 mmol) and $Pd(PPh_3)_4$ (275 mg, 0.24 mmol) were added and the reaction mixture was stirred at 80 °C for 17 h. The reaction mixture was cooled to 24 °C and the solvent removed under reduced pressure. The purple residue was taken up in CH_2Cl_2 (300 mL) and washed with saturated aqueous NH_4Cl (200 mL) and saturated aqueous NaCl (200 mL), dried over $MgSO_4$, filtered, and concentrated on a rotary evaporator. Column chromatography (SiO_2; 6:1 hexane/ CH_2Cl_2) yielded **40** (3.79 g, 4.08 mmol, 82%) as a purple solid. ^{1}H NMR (500 MHz, CD_2Cl_2, 22 °C): δ = 7.32 (m, 1H), 7.28–7.23 (m, 1H), 7.21–7.18 (m, 2H), 7.17–7.11 (m, 5H), 7.11–7.04 (m, 5H), 6.96–6.93 (m, 2H), 6.90–6.88 (m, 1H), 2.62–2.54 (m, 4H), 1.66–1.54 (m, 4H), 1.41–1.09 (m, 52H), 0.88 (t, J = 6.9 Hz, 6H), 0.19 (s, 9H) ppm; ^{13}C {^{1}H} NMR (151 MHz, $CDCl_3$): δ 201.0, 153.9, 152.9, 142.7, 142.5, 134.0, 133.3, 132.6, 131.9, 130.1, 130.0, 129.5, 129.4, 128.6, 128.3, 128.3, 128.2, 128.1, 128.1, 127.8, 125.5, 125.0, 123.2, 104.6, 94.9, 36.0, 35.9, 32.1, 31.4, 31.3, 29.9, 29.8, 29.8, 29.7, 29.7, 29.6, 29.5, 22.8, 14.3, 0.0 ppm; EI-HRMS (*m/z*): calcd for $C_{66}H_{93}OSi$ $[M+H]^+$ 929.6990, found 929.6990.

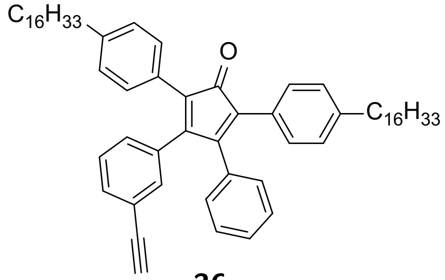

36

3-(3-Ethynylphenyl)-2,5-bis(4-hexadecylphenyl)-4-phenylcyclopenta-2,4-dienone (**36**): A 1000 mL three neck round bottom flask was charged under N_2 with **40** (3.68 g, 3.96 mmol) in THF (350 mL) and MeOH (350 mL). Solid KF (1.39 g, 23.9 mmol) was added and the reaction mixture was stirred at 40 °C for 7 h. The reaction mixture was concentrated on a rotary evaporator. Column chromatography (SiO_2; 6:1 hexane/CH_2Cl_2) yielded **36** (2.77 g, 3.23 mmol, 82%) as purple solid. ^1H NMR (600 MHz, CD_2Cl_2, 22 °C): $\delta = 7.36$ (dt, $J =$ 7.8, 1.4 Hz, 1H), 7.28–7.24 (m, 1H), 7.22–7.18 (m, 2H), 7.15 (t, $J = 7.8$ Hz, 1H), 7.13–7.10 (m, 4H), 7.10–7.05 (m, 5H), 6.96–6.92 (m, 3H), 3.04 (s, 1H), 2.59–2.52 (m, 4H), 1.63–1.54 (m, 4H), 1.35–1.11 (m, 52H), 0.88 (t, J = 7.0 Hz, 6H) ppm; ^{13}C $\{^1H\}$ NMR (151 MHz, $CDCl_3$, 22 °C): $\delta = 200.9$, 153.8, 152.7, 142.7, 142.5, 134.0, 133.3, 132.9, 132.1, 130.1, 130.0, 129.9, 129.4, 128.6, 128.4, 128.3, 128.2, 128.1, 128.0, 127.8, 125.7, 125.1, 122.1, 83.2, 77.7, 35.9, 32.1, 31.3, 31.3, 29.9, 29.9, 29.8, 29.8, 29.8, 29.8, 29.7, 29.7, 29.6, 29.5, 22.8, 14.3 ppm; EI-HRMS (*m/z*): calcd for $C_{63}H_{85}O$ $[M+H]^+$ 857.6595, found 857.6591.

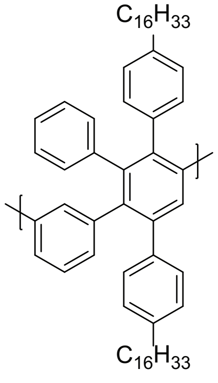

***poly*-36**

Poly-36 A 5 mL Schlenk tube was charged under N_2 with **36** (32 mg, 0.037 mmol) and diphenyl ether (167 mg, 0.98 mmol). The reaction mixture was degassed, the vessel sealed under N_2, and the reaction mixture was stirred at 230 °C for 6 h. After cooling to 24 °C the residue was taken up in THF and precipitated in MeOH (1:2 by volume) and centrifuged. The pellet was reprecipitated 4× to yield polymer **poly-36** as a yellow solid (28 mg, 91%). **42** was prepared according to a literature procedure.[222]

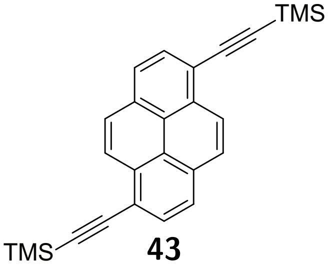

43

1,6-Bis((trimethylsilyl)ethynyl)pyrene (**43**): A 50 mL Schlenk tube was charged with **42** (379 mg, 1.0 mmol), CuI (18 mg, 0.096 mmol, 0.10 eq), magnetic stirbar, THF (7 mL), and NEt_3 (2.5 mL) under N_2. The reaction mixture was degassed freeze-pump-thaw. $Pd(PPh_3)_4$ (69 mg, 0.059 mmol, 0.06 eq) and TMSA (0.85 mL, 6.0 mmol, 6 eq) were added under N_2 and the reaction mixture was stirred at 50 °C for 43 h. The solvent was removed under reduced pressure and the residue was extracted with Et_2O. The combined organics were washed with 1M HCl (20 mL), and sat. NaCl (20 mL), dried with $MgSO_4$, filtered, and the solvent removed under reduced pressure. Column chromatography (SiO_2: 9:1 hexanes/EtoAc) yielded **43** (347 mg, 0.88, 88%) as a yellow solid. ^{1}H NMR (500 MHz, $CDCl_3$, 22 °C): δ = 8.54 (d, J=8.9 Hz, 2H), 8.14 (d, J=7.7 Hz, 2H), 8.12–8.05 (m, 4H), 0.42 (s, 18H) ppm; ^{13}C {^{1}H} NMR (126 MHz, $CDCl_3$, 22 °C): δ = 132.2, 131.1, 130.1, 128.1, 126.2, 125.0, 123.9, 118.2, 103.8, 100.6, 0.18 ppm; EI-HRMS (m/z): calcd for $C_{26}H_{26}Si_2$ $[M]^+$ 394.1573, found 394.1577. Matches previous report.**??**

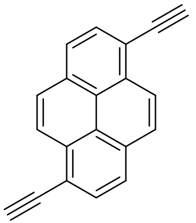

44

1,6-Diethynylpyrene (**44**): A 25 mL roundbottom flask was charged with **43** (347 mg, 0.88 mmol), MeOH (5 mL) and $CHCl_3$ (10 mL) under N_2. Solid K_2CO_3 (506 mg, 3.67 mmol, 4.2 eq) was added and the reaction mixture was stirred at 22 °C for 1 h. The reaction mixture was diluted with $CHCl_3$ (20 mL) and washed with 1M HCl (10 mL) and brine (10 mL), dried over $MgSO_4$, filtered, and the solvent removed under reduced pressure. Recrystallization from $CHCl_3$ yielded **44** as a brown solid (120 mg, 0.48 mmol, 55%). ^{1}H NMR (500 MHz, $CDCl_3$, 22 °C): δ = 8.63 (d, J=9.0 Hz, 2H), 8.24–8.12 (m, 6H), 3.64 (s, 2H) ppm; ^{13}C {^{1}H} NMR (126 MHz, $CDCl_3$, 22 °C): δ = 132.5, 131.3, 130.5, 128.2, 126.2, 125.1, 123.8, 117.2, 93.0, 82.5 ppm; EI-HRMS (m/z): calcd for $C_{20}H_{10}$ $[M]^+$ 250.0783, found 250.0783. Matches previous report.**??**

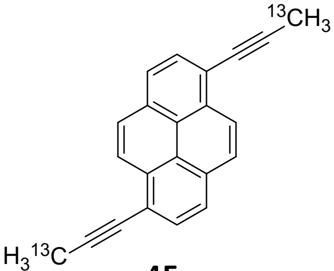

45

1,6-Di(prop-1-yn-1-yl-3-^{13}C)pyrene (**45**): An oven-dried 50 mL Schlenk tube was charged with **44** (9 mg, 0.036 mmol), dry THF (6 mL), and a magnetic stirbar under N_2. The reaction mixture was cooled to –78 °C and *n*-BuLi (2.5M in hexanes, 0.1 mL, 0.25 mmol, 7 eq) was added and stirred for 1 h. ^{13}C-MeI (0.1 mL, 1.6 mmol, 45 eq) was then added and stirred for 14 h with gradual warming to 22 °C. The reaction was quenched with addition of sat. NH_4Cl (10 mL), extracted with Et_2O (10 mL). The combined organics were washed with sat. NaCl (10 mL), dried with $MgSO_4$, filtered, and the solvent removed under reduced pressure. Column chromatography (SiO_2: hexanes) yielded **45** as a yellow solid (6 mg, 0.02 mmol, 59%). ^{1}H NMR (400 MHz, $CDCl_3$, 22 °C): δ = 8.56 (d, J=9.1 Hz, 2H), 8.13–8.03 (m, 6H), 2.30 (d, J=131.7 Hz, 6H) ppm.

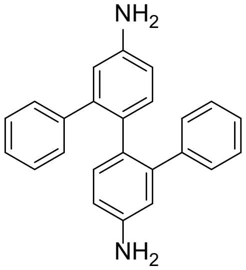

49

[1,1':2',1":2",1"'-Quaterphenyl]-4",5'-diamine (**49**): A 250 mL 3-neck roundbottom flask was charged with **2** (3.23 g, 7.41 mmol), Ph-B(OH)$_2$ (3.67 g, 30.1 mmol, 4.1 eq), K_2CO_3 (8.43 g, 61 mmol, 8.2 eq), Pd(PPh$_3$)$_4$ (147 mg, 0.13 mmol, 0. 018 eq), THF (80 mL), H_2O (60 mL), and a magnetic stirbar under N_2. The reaction mixture was degassed by freeze-pump-thaw and stirred at 75 °C for 24 h. After cooling to 22 °C the crude mixture was filtered through celite and washed with sat. $NaHCO_3$ (2 × 50 mL), sat. NaCl (2 × 50 mL), and the combined organics were dried with $MgSO_4$, filtered, and the solvent removed under reduced pressure. Column chromatography (SiO_2: 40% EtOAc in hexanes) yielded **49** (319 mg, 0.95 mmol, 13%). ^{1}H NMR (600 MHz, $CDCl_3$, 22 °C): δ = 7.12 (d, J=8.1 Hz, 2H), 7.06 (t, J=7.3 Hz, 2H), 6.99 (t, J=7.5 Hz, 4H), 6.68–6.62 (m, 6H), 6.49 (d, J=2.0 Hz, 2H), 3.67 (s(br), 4H) ppm; EI-HRMS (*m/z*): calcd for $C_{24}H_{20}N_2$ $[M]^+$ 336.1626, found 336.1622. Matches previous report.**??**

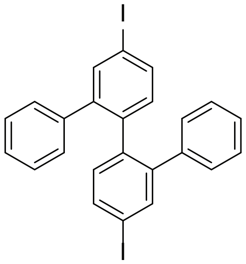

50

4”,5’-Diiodo-1,1’:2’,1”:2”,1”’-quaterphenyl (**50**): A 100 mL roundbottom flask was charged with **49** (283 mg, 0.84 mmol) and a magnetic stirbar. The reaction vessel was submerged in an ice water bath and to it were added sequentially H_2O (20 mL), conc. HCl (6 mL), and H_2SO_4 (20 mL). When the reaction mixture had reached 0 °C a solution of $NaNO_2$ (125 mg, 1.81 mmol, 2.2 eq) in H_2O (14 mL) was added dropwise over 17 min, maintaining an internal temperature <10 °C, and stirred for 1 h at 0 °C. The reaction mixture was then poured quickly into a solution of KI (1.50 g, 9.04 mmol, 10.8 eq) at 0 °C and stirred for 16 h with gradual warming to 22 °C. The reaction mixture was extracted with CH_2Cl_2 (3 × 50 mL) and the combined organics were washed with $Na_2S_2O_3$ (aq), and sat. NaCl, dried over $MgSO_4$, filtered, and the solvent removed under reduced pressure. Column chromatography (SiO_2: hexanes) yielded **50** (219 mg, 0.39 mmol, 47%) as a colorless solid. ^{1}H NMR (500 MHz, $CDCl_3$, 22 °C): δ = 7.66 (dd, J=8.2, 1.6 Hz, 2H), 7.51 (t, J=1.9 Hz, 2H), 7.12 (t, J=7.3 Hz, 2H), 7.07 (d, J=8.1 Hz, 2H), 7.03 (t, J=7.6 Hz, 4H), 6.56 (d, J=7.6 Hz, 4H) ppm; ^{13}C {^{1}H} NMR (126 MHz, $CDCl_3$, 22 °C): δ = 143.0, 139.2, 138.9, 138.6, 136.3, 133.2, 129.1, 127.9, 126.8, 93.6 ppm; EI-HRMS (m/z): calcd for $C_{24}H_{16}I_2$ $[M]^+$ 557.9342, found 557.9346.

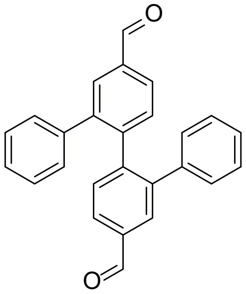

51

[1,1’:2’,1”:2”,1”’-Quaterphenyl]-4”,5’-dicarbaldehyde (**51**): An oven dried 25 mL Schlenk roundbottom flask was charged with **50** (182 mg, 0.33 mmol), a magnetic stirbar, and dry THF (10 mL). The reaction mixture was cooled to –78 °C and n-BuLi (2.5M in hexanes, 0.30 mL, 0.75 mmol, 2.3 eq) was added dropwise over 2 min. The reaction mixture was stirred under N_2 at –78 °C for 1 h, then dry DMF (3 mL) was added and the reaction mixture was stirred for 16 h with gradual warming to 22 °C. yielded **51** as a colorless solid (36 mg, 0.10 mmol, 30%). ^{1}H NMR (500 MHz, $CDCl_3$, 22 °C): δ = 10.05 (s, 2H), 7.90 (dd, J= 8.2, 1.9 Hz, 2H), 7.70 (d, J= 2.0 Hz, 2H), 7.59 (d, J=8.2 Hz, 2H), 7.14 (t, J=7.25 Hz, 2H), 7.04 (t, J=7.5 Hz, 4H), 6.60 (d, J=8.7 Hz, 4H) ppm; ^{13}C {^{1}H} NMR (126 MHz, $CDCl_3$, 22 °C):

δ = 192.0, 145.2, 142.0, 139.1, 136.1, 132.3, 131.9, 129.2, 128.1, 128.0, 127.1 ppm; EI-HRMS (*m/z*): calcd for $C_{26}H_{18}O_2$ $[M]^+$ 362.1307, found 362.1312.

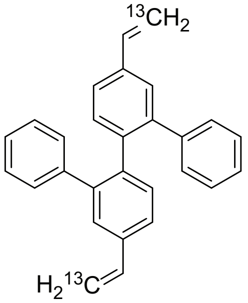

52

4”,5’-Di(vinyl-^{13}C)-1,1’:2’,1”:2”,1”’-quaterphenyl (**52**): An oven dried 25 mL Schlenk round-bottom flask was charged with ^{13}C-MePPh$_3$I (36 mg, 0.089 mmol, 3.2 eq), dry THF (3.5 mL), and a magnetic stirbar under N_2. The reaction mixture was cooled to 0 °C and *t*-BuOK (11.5 mg, 0.10 mmol, 3.7 eq) was added. The reaction mixture was stirred at 0 °C for 1 h, then **51** (10 mg, 0.028 mmol) was added. The mixture was stirred at 0 °C for 1 h, and then for a further 16 h at 22 °C. The crude mixture was diluted with Et_2O (10 mL) and washed with sat. NH_4Cl (10 mL) and sat. NaCl (10 mL). The combined organics were dried over $MgSO_4$, filtered, and the solvent removed under reduced pressure. Column chromatography (SiO_2: hexanes) yielded **52** (8 mg, 0.022 mmol, 79%) as a colorless solid. ^{1}H NMR (500 MHz, $CDCl_3$, 22 °C): δ = 7.41 (d, *J*=7.5 Hz, 2H), 7.35 (d, *J*=7.9 Hz, 2H), 7.21 (s, 2H), 7.10 (t, *J*=7.2 Hz, 4H), 6.73 (dd, *J*=17.6 , 11.0 Hz, 2H), 6.65 (d, *J*=7.4 Hz, 4H), 5.77 (dd, *J*=154.4, 17.6 Hz, 2H), 5.26 (dd, *J*=160.3, 10.9 Hz, 2H) ppm; ^{13}C {^{1}H} NMR (126 MHz, $CDCl_3$, 22 °C): δ = 141.3, 140.9, 139.4, 136.8, 136.3, 132.0, 129.2, 128.3, 127.7, 126.2, 124.9, 114.1 ppm.

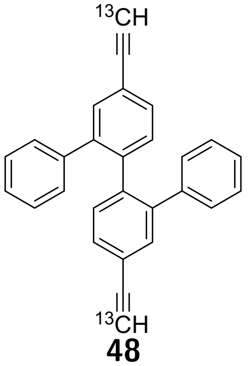

48

4”,5’-Di(ethynyl-^{13}C)-1,1’:2’,1”:2”,1”’-quaterphenyl (**48**): An oven dried 50 mL Schlenk tube was charged with **52** (8 mg, 0.022 mmol), dry CH_2Cl_2 (3 mL), and a magnetic stirbar. The reaction mixture was cooled to 0 °C and a solution of Br_2 in CH_2Cl_2 (0.6M, 0.1 mL, 0.06 mmol, 2.7 eq) was added dropwise over 10 min. The reaction was stirred at 0 °C for 30 min, then stirred at 22 °C for a further 2 h. Volatiles were removed at reduced pressure and dry Et_2O (3 mL) was added to the reaction vessel, at which point *t*-BuOK (70 mg, 0.62

mmol, 28 eq) was added with stirring over 1 h, then stirred at 22 °C for 5 h. The mixture was washed with H_2O (2 × 2 mL) and sat. NaCl (2 mL), the combined organics were dried over $MgSO_4$, filtered, and the solvent removed at reduced pressure. Column chromatography (SiO_2: hexanes:toluene 95:5) yielded **48** (3 mg, 0.008 mmol, 36%) as a colorless solid. ^{1}H NMR (500 MHz, $CDCl_3$, 22 °C): δ = 7.47 (d, J=8.5 Hz, 2H), 7.36–7.30 (m, 4H), 7.10 (t, J=6.8 Hz, 2H), 7.01 (t, J=7.8 Hz, 4H), 6.57 (d, J=8.1 Hz, 4H), 3.10 (d, J=251.6 Hz, 2H) ppm.

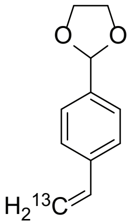

54

2-(4-[2-^{13}C]Vinylphenyl-1,3-dioxolane (**54**): A 200 mL Schlenk round bottom flask was charged under N_2 with methyl-^{13}C-triphenylphosphonium iodide (219 mg, 0.54 mmol) in dry THF (12 mL). The reaction mixture cooled to 0 °C, followed by addition of *t*-BuOK (72 mg, 0.64 mmol). The reaction mixture was stirred at 0 °C for 1 h. After darkening the flask with aluminum foil, a solution of 4-(1,3-dioxolan-2-yl)benzaldehyde (99 mg, 0.55 mmol) in dry THF (3 mL) was added to the yellow reaction mixture at 0 °C. The reaction mixture was stirred for 24 h at 24 °C in the dark. The reaction mixture was diluted with EtOAc (50 mL) and washed with saturated aqueous ammonium chloride. The aqueous phase was extracted with EtOAc (2 × 50 mL). The combined organic phases were dried over $MgSO_4$, filtered, and concentrated on a rotary evaporator. Column chromatography (SiO_2; 9:1 hexane/ EtOAc) yielded **54** (87 mg, 0.49 mmol, 88%) as a colorless oil. ^{1}H NMR (600 MHz, $CDCl_3$, 22 °C): δ = 7.48–7.36 (m, 4H), 6.72 (dd, J = 17.6, 10.9 Hz, 1H), 5.81 (s, 1H), 5.77 (ddd, J = 154.6, 17.6, 0.9 Hz, 1H), 5.26 (ddd, J = 160.5, 10.9, 0.9 Hz, 1H), 4.18–4.09 (m, 2H), 4.08–3.99 (m, 2H) ppm; ^{13}C {^{1}H} NMR (126 MHz, $CDCl_3$, 22 °C): δ = 138.6, 137.5, 136.6 (d, J = 69.7 Hz), 126.8, 126.3 (d, J = 4.9 Hz), 114.6, 103.7, 65.4 ppm; EI-HRMS (m/z): calcd for $^{12}C_{10}{}^{13}C_1H_{12}O_2$ $[M]^+$ 17.0871, found 177.0868.

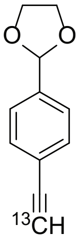

55

2-(4-[2-^{13}C]Ethynylphenyl)-1,3-dioxolane (**55**): A 100 mL Schlenk round bottom flask was charged under N_2 with **54** (219 mg, 1.24 mmol) in dry CH_2Cl_2. Br_2 (0.1 mL, 1.94 mmol) was added dropwise over 2 min at 0 °C and the reaction mixture was stirred at 0 °C for 3 h. Solvent and excess Br_2 were removed at reduced pressure. The residue was dissolved in dry THF (60 mL) and cooled to 0 °C, followed by addition of *t*-BuOK (497 mg, 4.43 mmol). The reaction mixture was stirred for 1 h at 0 °C, and then 15 h at 24 °C. The reaction mixture was quenched with saturated aqueous ammonium chloride (60 mL), and extracted with EtOAc (3×60 mL). The combined organic phases were dried over $MgSO_4$, filtered, and concentrated on a rotary evaporator. Column chromatography (SiO_2; 9:1 hexane/ EtOAc) yielded **55** (84 mg, 0.48 mmol, 39%) as a colorless solid; ^{1}H NMR (500 MHz, $CDCl_3$, 22 °C): δ = 7.51 (d, J = 8.2 Hz, 2H), 7.44 (d, J = 8.2 Hz, 2H), 5.81 (s, 1H), 4.16–4.09 (m, 2H), 4.09–4.01 (m, 2H), 3.09 (d, J = 251.5 Hz, 1H) ppm; ^{13}C {^{1}H} NMR (126 MHz, $CDCl_3$, 22 °C): δ = 138.6, 132.2, 126.5, 123.0 (d, J = 12.7 Hz), 103.3, 83.5 (d, J = 176.3 Hz), 77.8, 65.4 ppm; ESI-HRMS (*m/z*): calcd for $^{12}C_{10}{}^{13}C_1H_{10}O_2$ [M]$^+$ 175.00714, found 175.0709.

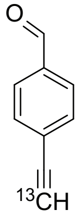

56

4-[2-^{13}C]Ethynylbenzaldehyde (**56**): A 25 mL round bottom flask was charged with **55** (72 mg, 0.41 mmol), in MeOH (6 mL). Aqueous HCl (1 M, 6 mL) was added and the reaction mixture stirred for 3 h at 30 °C. The reaction mixture was quenched with saturated aqueous $NaHCO_3$ (10 mL) and extracted with CH_2Cl_2 (3×15 mL). The combined organic phases were washed with, saturated aqueous NaCl (30 mL), dried over $MgSO_4$, filtered, and concentrated on a rotary evaporator. Column chromatography (SiO_2; 2:1 hexane/ CH_2Cl_2) yielded **56** (42 mg, 0.32 mmol, 78%) as a colorless solid. ^{1}H NMR (500 MHz, $CDCl_3$, 22 °C): δ = 10.02 (s, 1H), 7.85 (d, J = 8.2 Hz, 2H), 7.65 (d, J = 8.2 Hz, 2H), 3.29 (d, J = 253.1 Hz, 1H) ppm; ^{13}C {^{1}H} NMR (126 MHz, $CDCl_3$, 22 °C): δ = 191.6, 136.0, 132.8, 129.6, 128.4 (d, J = 12.7 Hz), 82.0 (d, J = 82.2 Hz), 81.22 ppm; ESI-HRMS (*m/z*): calcd for $^{12}C_8{}^{13}C_1H_6O_1$ [M]$^+$ 131.0452, found 131.0449.

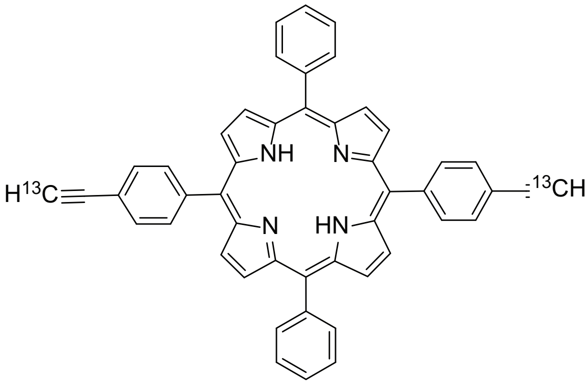

57

5,15-bis(4-[2-^{13}C]Ethynlphenyl)-10,20-diphenyl-21H,23H-porphine (**57**): A 100 mL Schlenk round bottom flask was charged under N_2 with **56** (40 mg, 0.305 mmol) and

5-phenyldipyrromethane (68 mg, 0.306 mmol) in dry CH_2Cl_2 (32 mL). The reaction vessel was darkened with aluminum foil. TFA (0.02 mL, 0.26 mmol) was added and the reaction mixture was stirred at 24 °C for 3 h, at which point DDQ (144 mg, 0.63 mmol) was added and the reaction mixture stirred at 24 °C for an additional 1 h. The reaction mixture was quenched with NEt_3 (1 mL) and filtered through a plug of silica, eluting with CH_2Cl_2, and concentrated on a rotary evaporator. Column chromatography (SiO_2; 1:1 hexane/ CH_2Cl_2) yielded **57** (11 mg, 0.17 mmol, 11%) as a purple solid. ^{1}H NMR (500 MHz, $CDCl_3$, 22 °C): δ = 8.89–8.79 (m, 8H), 8.23–8.17 (m, 8H), 7.90 (d, J = 7.7 Hz, 4H), 7.80–7.72 (m, 6H), 3.32 (d, J = 251.4 Hz, 2H), -2.81 (s, br, 2H) ppm; ^{13}C {^{1}H} NMR (226 MHz, $CDCl_3$, 22 °C): δ = 142.9, 142.8, 142.2, 142.1, 134.6 (d, J = 18.3 Hz), 130.7, 128.0, 127.9, 126.9, 125.0, 121.8, 120.6, 120.4, 119.4, 78.5, 78.4 (d, J = 88 Hz) ppm; ESI-HRMS (m/z): calcd for $^{12}C_{46}{}^{13}C_2H_{31}N_4$ $[M+H]^+$ 665.2610, found 665.2609.

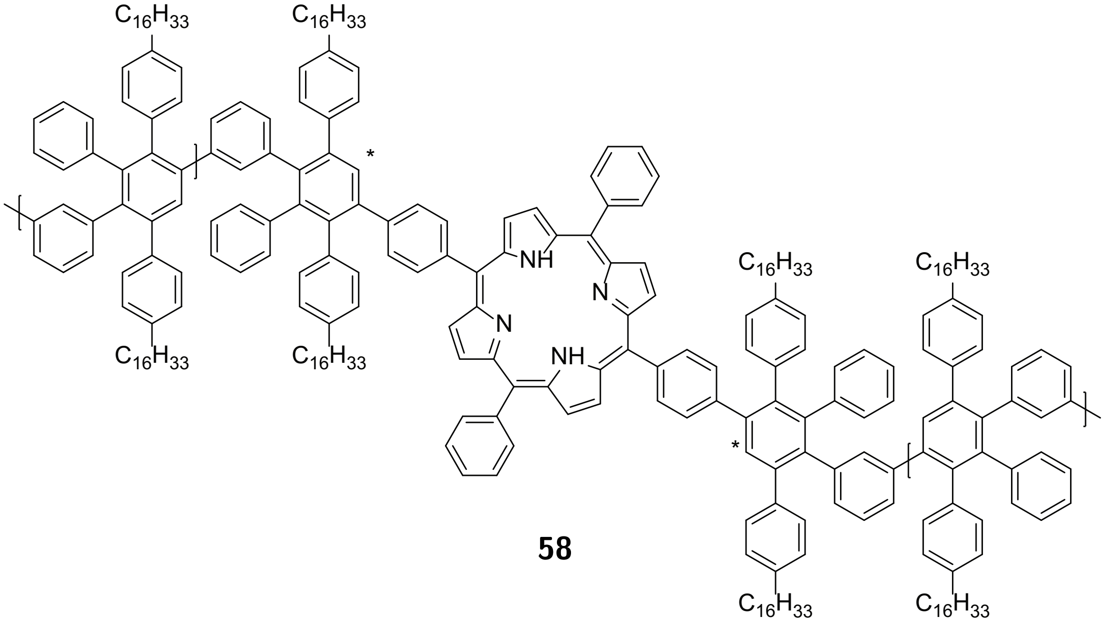

58

58: A 5 mL Schlenk tube was charged under N_2 with **36** (62 mg, 0.072 mmol), **57** (2.0 mg, 0.003 mmol) and diphenyl ether (280 mg, 1.65 mmol). The reaction mixture was degassed, the vessel sealed under N_2, and the reaction mixture was stirred at 230 °C for 16 h. After cooling to 24 °C the residue was taken up in THF and precipitated in MeOH (1:2 by volume) and centrifuged. The pellet was reprecipitated 4× to yield polymer **58** as a red solid (53.4 mg, 86%), Mn = 29 000, PDI = 1.8 based on SEC analysis. Fractionation by chromatography over SiO_2 (10% DCM in hexanes, followed by DCM) yielded **poly-36** (28 mg), Mn = 27 000, PDI = 2.2, and **58** (25 mg) Mn = 11 000, PDI = 1.2.

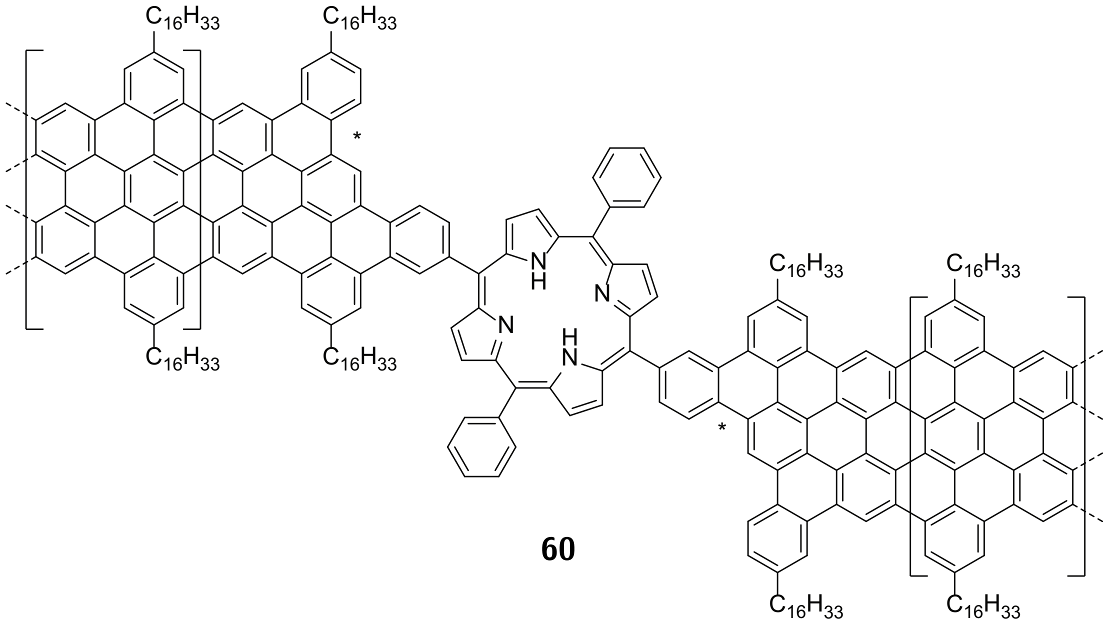

60

60: A 500 mL Schlenk round bottom flask was charged under N_2 with polymer **58** (50 mg) in dry CH_2Cl_2 (200 mL). To this was added a solution of $FeCl_3$ (3.923 g, 24.2 mmol) in dry $MeNO_2$ (8 mL). Nitrogen was bubbled through the reaction mixture with stirring at 24 °C for 66 h. The reaction mixture was then poured into MeOH (800 mL) and filtered. The dark precipitate was washed sequentially with MeOH (500 mL), THF (500 mL), 1M HCl (500 mL), H_2O (500 mL), 15% NaOH (500 mL), and MeOH (500 mL) to yield **60** as a dark purple powder (48 mg, 97%).

60@Zn: A 25 mL heavy wall pressure vessel was charged with GNR **60** (10 mg) and $Zn(OAc)_2$ (18 mg, 0.098 mmol), in toluene (6 mL). The reaction mixture was sonicated for 5 min., and then stirred at 120 °C for 42 h. The reaction mixture was filtered and the precipitate washed sequentially with toluene, MeOH, 1M HCl, H_2O, 15% NaOH, H_2O, and MeOH to yield **60@Zn** as a dark purple powder (9 mg, 90%).

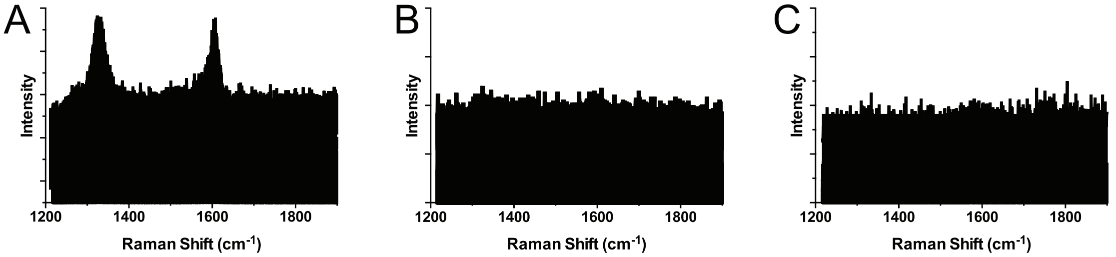

Figure 5.1: Collected line scans of the Raman mapping experiments (Figure 3.11) for A) **Zn@60** on aminated SAM, B) cGNR on aminated SAM, and C) **Zn@60**.

Time (h)	Total Charge (C)	Volume CO (mL)	FE_{CO} (%)	Volume H_2 (mL)	FE_{H2} (%)
0.5	7.8	0.79	80.3	0.24	24.0
1	15.6	1.54	78.2	0.50	25.2
2	31.3	3.10	78.2	0.96	24.3
3	46.8	4.59	77.4	1.45	24.5
4	66.9	6.39	75.5	1.90	22.4
6	103.1	9.54	73.1	3.13	24.0
8	131.2	12.03	72.4	4.13	24.9
10	168.0	15.07	70.8	5.42	25.5

Table 5.1: Controlled potential electrolysis experiments at −0.47 V using coveester GNR-AuNP composite electrodes. Results of controlled potential electrolysis experiments at −0.47 V to explore the stability and CO_2 reduction performance of the coveester GNR-AuNP composite electrodes. Note: The TCD channel of the GC has a high detection limit for H_2 and the internal standard C_2H_4, leading to some uncertainty in the quantification of H_2. As a result, the Faradaic efficiency for H_2 and the overall Faradaic efficiency have an error of up to ± 10%. However, the CO quantification by GC (FID) is accurate, and therefore so are the corresponding Faradaic efficiencies.

Time (h)	Total Charge (C)	Volume CO (mL)	FE_{CO} (%)	Volume H_2 (mL)	FE_{H2} (%)
0.5	6.8	0.59	68.3	0.28	33.1
1	13.4	1.16	68.1	0.58	34.1
2	26.4	2.25	67.3	1.22	36.4
3	40.1	3.40	66.9	1.68	33.1
4	53.0	4.39	65.4	2.38	35.5
6	77.8	6.22	63.1	3.54	35.9
8	103.2	8.03	61.4	4.66	35.7
10	129.6	9.77	59.5	6.08	37.0

Table 5.2: Controlled potential electrolysis experiments at −0.47 V using cove GNR-AuNP composite electrodes. Results of controlled potential electrolysis experiments at −0.47 V to explore the stability and CO_2 reduction performance of the cove GNR-AuNP composite electrodes. Note: The TCD channel of the GC has a high detection limit for H_2 and the internal standard C_2H_4, leading to some uncertainty in the quantification of H_2. As a result, the Faradaic efficiency for H_2 and the overall Faradaic efficiency have an error of up to ± 10%. However, the CO quantification by GC (FID) is accurate, and therefore so are the corresponding Faradaic efficiencies.

Time (h)	Total Charge (C)	Volume CO (mL)	FE_{CO} (%)	Volume H_2 (mL)	FE_{H2} (%)
0.5	2.3	0.17	57.3	0.14	49.6
1	4.6	0.33	57.3	0.29	49.2
2	9.2	0.65	55.9	0.59	50.8
3	14.2	0.94	52.1	0.96	53.4
4	19.1	1.19	49.3	1.27	52.6
6	28.5	1.60	44.3	1.90	52.6
8	37.7	1.96	41.2	2.68	56.1
10	47.2	2.41	40.4	3.35	56.1

Table 5.3: Controlled potential electrolysis experiments at −0.47 V using chevron GNR-AuNP composite electrodes. Results of controlled potential electrolysis experiments at −0.47 V to explore the stability and CO_2 reduction performance of the chevron GNR-AuNP composite electrodes. Note: The TCD channel of the GC has a high detection limit for H_2 and the internal standard C_2H_4, leading to some uncertainty in the quantification of H_2. As a result, the Faradaic efficiency for H_2 and the overall Faradaic efficiency have an error of up to ± 10%. However, the CO quantification by GC (FID) is accurate, and therefore so are the corresponding Faradaic efficiencies.

Time (h)	Total Charge (C)	Volume CO (mL)	FE_{CO} (%)	Volume H_2 (mL)	FE_{H2} (%)
0.5	0.30	0.02	45.0	0.02	59.0
1	0.66	0.04	42.9	0.05	60.7
2	1.18	0.06	38.5	0.11	71.1
3	1.95	0.07	27.3	0.19	75.3
4	2.71	0.08	23.0	0.25	73.6
6	3.61	0.09	20.7	0.36	78.8
8	4.63	0.10	16.9	0.49	83.6
10	5.65	0.11	15.0	0.62	87.0

Table 5.4: Controlled potential electrolysis experiments at −0.47 V using Cblack-AuNP composite electrodes. Results of controlled potential electrolysis experiments at −0.47 V on Cblack-AuNP composite electrodes to serve as a standard reference for GNR composite performance and stability. Note: The TCD channel of the GC has a high detection limit for H_2 and the internal standard C_2H_4, leading to some uncertainty in the quantification of H_2. As a result, the Faradaic efficiency for H_2 and the overall Faradaic efficiency have an error of up to ± 10%. However, the CO quantification by GC (FID) is accurate, and therefore so are the corresponding Faradaic efficiencies.

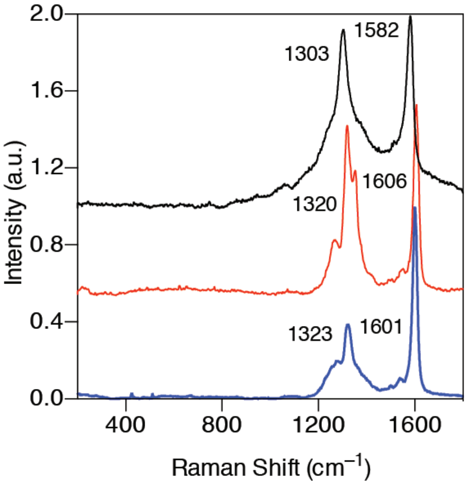

Figure 5.2: Raman spectra of GNRs. Chevron GNRs (**62**) (blue), cove GNRs (**65a**) (red), and coveester GNR (**65b**) (black).

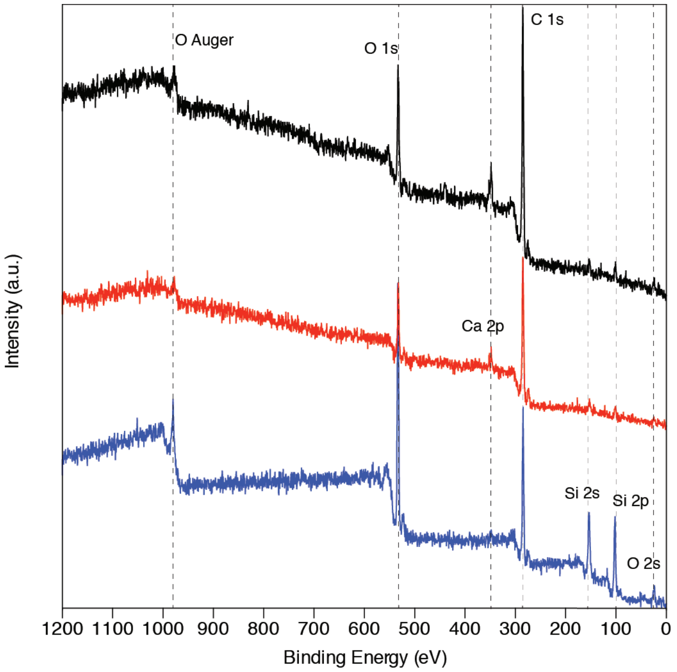

Figure 5.3: X-ray photoelectron spectroscopy (XPS) characterization GNRs. XPS of chevron GNRs (**62**) (blue), cove GNRs (**65a**) (red), and coveester GNRs (**65b**) (black). Samples were prepared by sonicating 0.5 mg of the respective GNR in THF (0.5 mL) and dropcasting onto a Si wafer held at 80 °C. All samples show prominent C 1s signals from the deposited GNR, as well as Si and O signals from the underlying substrate. While adventitious Ca was observed in some samples, prominent signals associated with Ni (2p3/2, 853 eV; 2p1/2, 870 eV) and Fe (2p3/2, 707 eV; 2p1/2, 720 eV) used as reagents or catalysts in the GNR synthesis could not be detected in purified GNR.

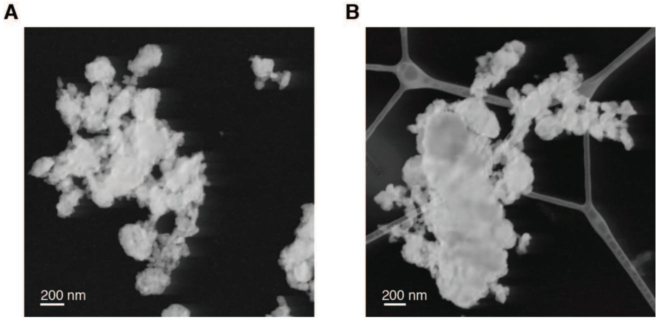

Figure 5.4: Structural characterization of GNRs. (A,B) STEM of chevron GNR (**62**) aggregates.

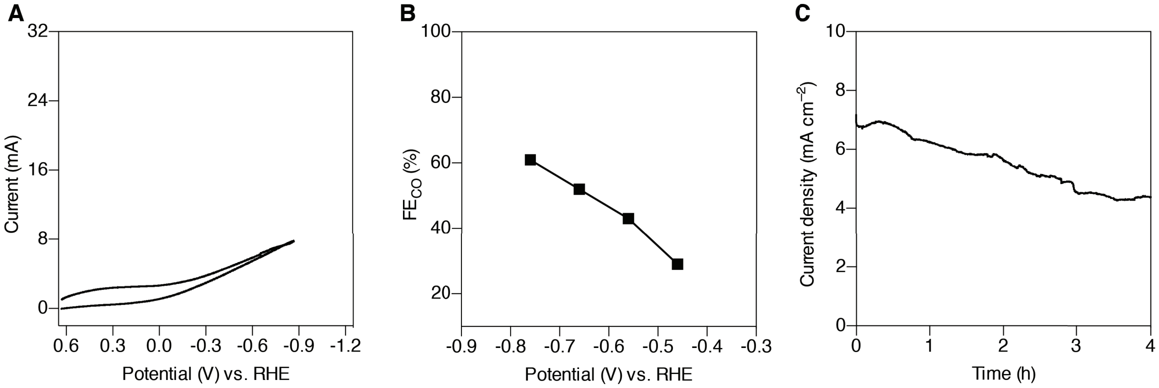

Figure 5.5: Electrocatalytic performance of SWCNT-AuNP composites. SWCNT-AuNP composites serve as an additional point of reference for the performance of GNR-AuNP composites. The SWCNT-AuNP composite materials exhibit drastically inferior performance, even in comparison to Cblack composites. In a direct comparison with GNR composites, CO_2 reduction activity was significantly reduced at mildly reducing potentials, and correspondingly FECO is reduced across the entire potential window. SWCNT-AuNP composites were prepared following the same procedure described for GNR and Cblack composites, but using SWCNTs as support material. All electrochemical experiments were performed in 0.5 M aqueous $KHCO_3$ solution saturated with CO_2 (pH 7.3). (A) Cyclic voltammogram of SWCNT-AuNP composite material. (B) Faradaic efficiencies for CO production (FECO) by SWCNT-AuNP composite electrodes. Electrolysis performed at potentials from −0.47 V to −0.77 V vs. RHE. (C) Total current density for SWCNT-AuNP composite over 4 h at −0.77 V vs. RHE. Note that this potential is more negative than that used for long-term controlled potential electrolysis experiments using GNR or Cblack support materials (−0.47 V vs. RHE); at −0.47 V the SWCNT composite showed minimal CO_2 reduction activity. Across the 4 h experiment, FECO for the SWCNT-AuNP composite fell to 27% from its initial value of 61%.

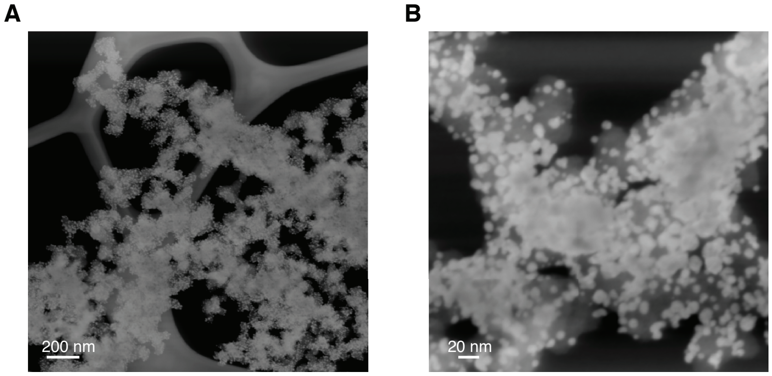

Figure 5.6: (A) HAADF-STEM image of Cblack-AuNP composites after annealing show a narrow size distribution centered around an average NP diameter of 8 nm. (B) HAADF-STEM image of Cblack-AuNP composites after 3 h of bulk electrocatalysts in 0.5 M aqueous $KHCO_3$ saturated with CO_2 (pH 7.3) show a significant broadening of the AuNP size distribution as a result of sintering of AuNPs.

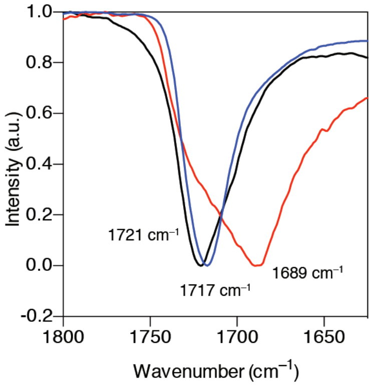

Figure 5.7: IR spectrum of coveester GNRs. The carbonyl CO stretch of the coveester GNR (**65b**) following the Scholl reaction matches that of the ester-functionalized ***poly*-73**, indicating that the esters remain intact. A partially saponified sample of ***poly*-73** shows a significant shift of the CO stretching frequency that is absent in the IR spectrum of coveester GNR (**65b**). We thus conclude that the methyl esters in coveester GNR (**65b**) have not been saponified under the reaction conditions.

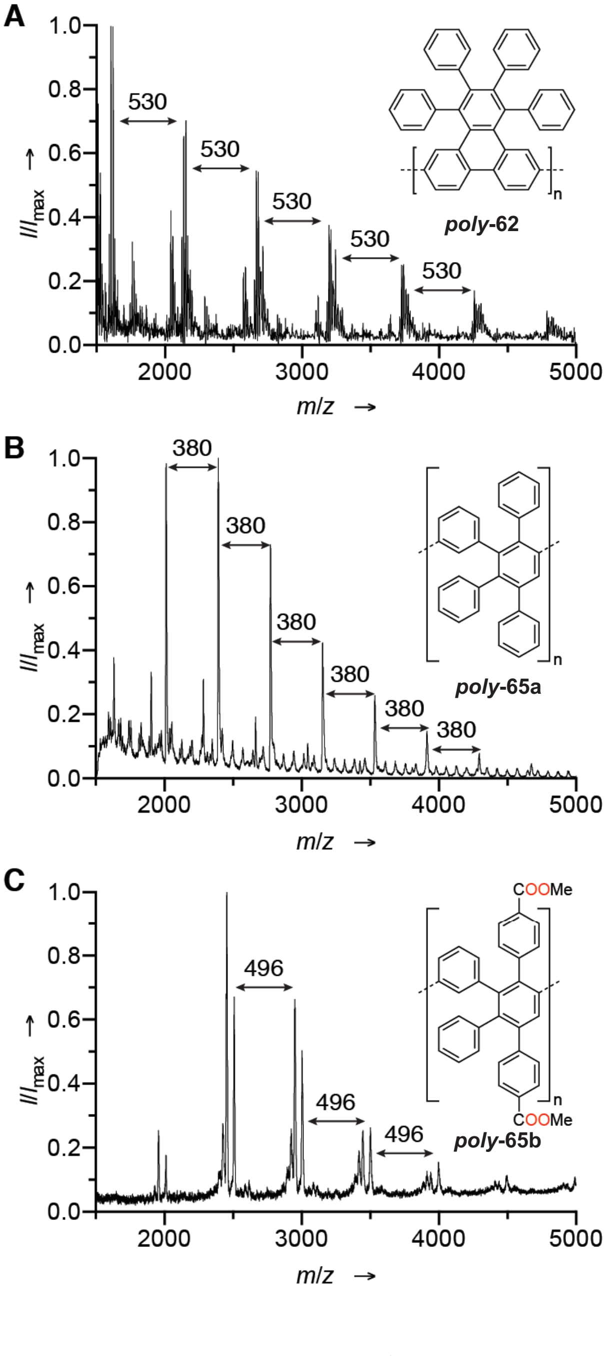

Figure 5.8: MALDI of GNR precursor polymers. MALDI mass spectrometry of (A) chevron GNR precursor ***poly*-61**, (B) cove GNR precursor ***poly*-64a**, (C) coveester GNR precursor ***poly*-64b**.

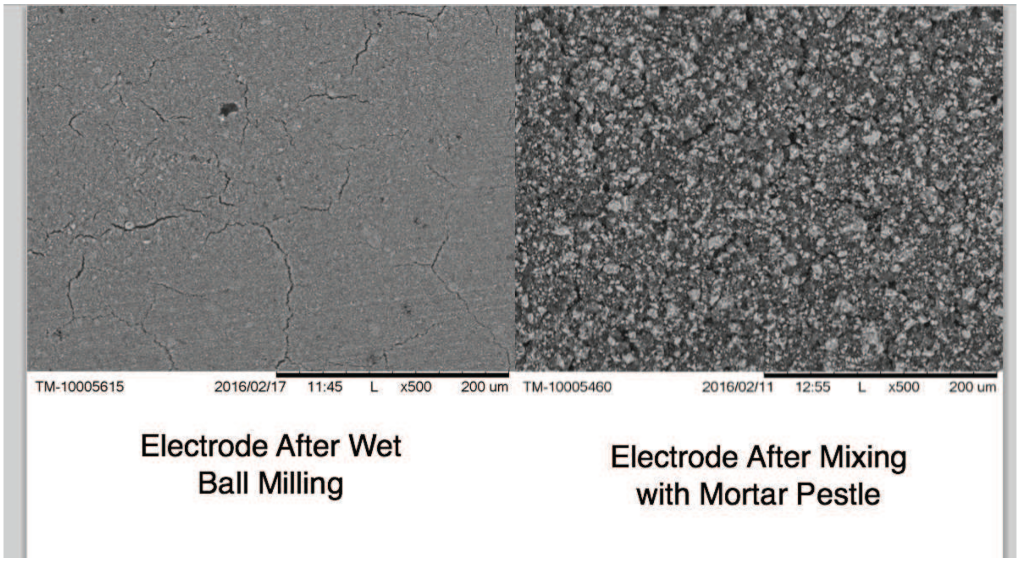

Figure 5.9: SEM comparison of ball milled and hand ground GNR/SnO_2 composite electrodes.

Chapter 6

Appendix

This chapter includes the Quantum Espresso input files for electronic calculations on $N = 9$ and $N = 11$ AGNRs, unfuctionalized, ester functionalized, and carboxylic acid functionalized cove GNRs, and chevron GNRs.

6.1 $N = 9$ AGNR Quantum Espresso Code

Relax Calculation Input

```
&CONTROL

    calculation = 'relax' ,
    pseudo_dir = '/usr/software/espresso-5.1.1/pseudo' ,
    prefix = '9AGNR' ,
    forc_conv_thr = 1.0D-3 ,

/
&SYSTEM
    ibrav = 8,
    celldm(1) = 8,
    celldm(2) = 20,
    celldm(3) = 20,
    nat = 22,
    ntyp = 2,
    ecutwfc = 70.0 ,
    ecutrho = 280.0 ,

/
&ELECTRONS

    conv_thr = 0.0001 ,

/
&IONS
/
ATOMIC_SPECIES

 C   12.01070   C.pbe-mt_fhi.UPF
 H    1.00794   H.pbe-mt_fhi.UPF

ATOMIC_POSITIONS angstrom


                    C   -4.060200000   14.064000000   0.000000000
                    C   -3.366400000   12.841100000   0.000000000
                    C   -1.965000000   12.842000000   0.000000000
                    C   -1.272100000   14.066700000   0.000000000
```

```
C   -1.970200000   15.285100000   0.000000000
C   -3.362600000   15.283700000   0.000000000
H   -1.436300000   16.221300000   0.000000000
H   -3.896900000   16.218600000   0.000000000
C   -4.061500000   11.618500000   0.000000000
C   -3.366200000   10.396500000   0.000000000
C   -1.964700000   10.396600000   0.000000000
C   -1.269900000   11.619700000   0.000000000
C   -4.062200000    9.174700000   0.000000000
C   -3.367100000    7.952300000   0.000000000
C   -1.965000000    7.951500000   0.000000000
C   -1.269700000    9.173600000   0.000000000
C   -4.061900000    6.729700000   0.000000000
C   -3.363900000    5.510200000   0.000000000
C   -1.970200000    5.508900000   0.000000000
C   -1.271400000    6.727100000   0.000000000
H   -3.899100000    4.575500000   0.000000000
H   -1.435900000    4.572900000   0.000000000

K_POINTS automatic

32 1 1 0 0 0
```

Non Self-Consistent Input

```
&CONTROL

    calculation = ’nscf’ ,
    outdir = ’/home/wsperkins/Quantum_Pyrene/N9/258567’ ,
    pseudo_dir = ’/usr/software/espresso-5.1.1/pseudo’ ,
    prefix = ’9AGNR’ ,
    forc_conv_thr = 1.0D-3 ,

/
&SYSTEM

    ibrav = 8,
    celldm(1) = 8,
    celldm(2) = 20,
    celldm(3) = 20,
    nat = 22,
    ntyp = 2,
```

```
    ecutwfc = 70.0 ,
    ecutrho = 280.0 ,
    nbnd = 40,

/
&ELECTRONS

    conv_thr = 0.0001 ,

/
ATOMIC_SPECIES

 C   12.01070   C.pbe-mt_fhi.UPF
 H    1.00794   H.pbe-mt_fhi.UPF

ATOMIC_POSITIONS angstrom


                    C   -4.069999646   14.086888378   0.000000000
                    C   -3.372735945   12.859996827   0.000000000
                    C   -1.959287670   12.859992504   0.000000000
                    C   -1.262475340   14.087104270   0.000000000
                    C   -1.985266735   15.290733608   0.000000000
                    C   -3.347086319   15.290591821   0.000000000
                    H   -1.469612555   16.241280976   0.000000000
                    H   -3.862909463   16.240988008   0.000000000
                    C   -4.078140473   11.623102243   0.000000000
                    C   -3.375624564   10.396821912   0.000000000
                    C   -1.956238048   10.396866141   0.000000000
                    C   -1.253929867   11.623167236   0.000000000
                    C   -4.078276552    9.170455343   0.000000000
                    C   -3.373014404    7.933678363   0.000000000
                    C   -1.959566282    7.933745698   0.000000000
                    C   -1.254069262    9.170397618   0.000000000
                    C   -4.070353409    6.706682816   0.000000000
                    C   -3.347606212    5.503068549   0.000000000
                    C   -1.985780269    5.503076101   0.000000000
                    C   -1.262833941    6.706521623   0.000000000
                    H   -3.863282317    4.552589880   0.000000000
                    H   -1.470310727    4.552450086   0.000000000
```

```
  K_POINTS automatic

 32 1 1 0 0 0
```

Density of States Input

```
&DOS

    prefix = '9AGNR',
    outdir = '/home/wsperkins/Quantum_Pyrene/N9/258567',
    fildos = '9AGNR_fildos',
    Emin = -23,
    Emax = 0,
    ngauss = 0,
    degauss = 0.00293996,
    DeltaE = 0.01,

/
```

Band Structure Input

```
&BANDS

    prefix = '9AGNR',
    outdir = '/home/wsperkins/Quantum_Pyrene/N9/258567',
    filband = '9AGNR_bands_filband',

/
```

6.2 $N = 11$ AGNR Quantum Espresso Code

Relax Calculation Input

```
&CONTROL

    calculation = 'relax' ,
    pseudo_dir = '/usr/software/espresso-5.1.1/pseudo' ,
    prefix = '11AGNR_yz' ,
```

```
    forc_conv_thr = 1.0D-3 ,

/
&SYSTEM

    ibrav = 8,
    celldm(1) = 8,
    celldm(2) = 20,
    celldm(3) = 20,
    nat = 26,
    ntyp = 2,
    ecutwfc = 70.0 ,
    ecutrho = 280.0 ,

/
&ELECTRONS

    conv_thr = 0.0001 ,

/
&IONS
/
ATOMIC_SPECIES

 C   12.01070   C.pbe-mt_fhi.UPF
 H    1.00794   H.pbe-mt_fhi.UPF

ATOMIC_POSITIONS angstrom


                    C    1.706191839    6.100030548   0.000000000
                    C    0.294180648    6.100056911   0.000000000
                    C   -0.412776332    4.869473265   0.000000000
                    C    2.413026046    4.869562480   0.000000000
                    C    1.705928538    8.560029697   0.000000000
                    C    0.293951621    8.559995896   0.000000000
                    C   -0.409833073    7.329886265   0.000000000
                    C    2.409772837    7.329923903   0.000000000
                    C    1.707263489   11.025287678   0.000000000
                    C    0.291993830   11.025250074   0.000000000
                    C   -0.413259925    9.790291015   0.000000000
                    C    2.412608677    9.790302760   0.000000000
```

```
C   1.678905891   13.460650063   0.000000000
C   0.320107506   13.460539024   0.000000000
C  -0.406923904   12.253902509   0.000000000
C   2.405759079   12.253944070   0.000000000
H   2.195158018   14.410641168   0.000000000
H  -0.195687232   14.410746745   0.000000000
C   2.406293016    2.406154727   0.000000000
C   1.707835679    3.634617311   0.000000000
C   0.292503548    3.634686893   0.000000000
C  -0.406370543    2.405985560   0.000000000
C   0.320499229    1.199649414   0.000000000
C   1.679147719    1.199658283   0.000000000
H  -0.195319343    0.249196327   0.000000000
H   2.194843144    0.249337416   0.000000000

 K_POINTS automatic

32 1 1 0 0 0
```

Non Self-Consistent Input

```
&CONTROL

    calculation = 'nscf' ,
    outdir = '/home/wsperkins/Quantum_Pyrene/11AGNR_ecutwft70_yzexpansion/248069'
    ,
    pseudo_dir = '/usr/software/espresso-5.1.1/pseudo' ,
    prefix = '11AGNR_yz' ,
    forc_conv_thr = 1.0D-3 ,

/
&SYSTEM

    ibrav = 8,
    celldm(1) = 8,
    celldm(2) = 20,
    celldm(3) = 20,
    nat = 26,
    ntyp = 2,
    ecutwfc = 70.0 ,
    ecutrho = 280.0 ,
```

```
    nbnd = 50,

/
&ELECTRONS

    conv_thr = 0.0001 ,

/
ATOMIC_SPECIES

 C   12.01070   C.pbe-mt_fhi.UPF
 H    1.00794   H.pbe-mt_fhi.UPF

ATOMIC_POSITIONS angstrom

                    C    1.706191839    6.100030548   0.000000000
                    C    0.294180648    6.100056911   0.000000000
                    C   -0.412776332    4.869473265   0.000000000
                    C    2.413026046    4.869562480   0.000000000
                    C    1.705928538    8.560029697   0.000000000
                    C    0.293951621    8.559995896   0.000000000
                    C   -0.409833073    7.329886265   0.000000000
                    C    2.409772837    7.329923903   0.000000000
                    C    1.707263489   11.025287678   0.000000000
                    C    0.291993830   11.025250074   0.000000000
                    C   -0.413259925    9.790291015   0.000000000
                    C    2.412608677    9.790302760   0.000000000
                    C    1.678905891   13.460650063   0.000000000
                    C    0.320107506   13.460539024   0.000000000
                    C   -0.406923904   12.253902509   0.000000000
                    C    2.405759079   12.253944070   0.000000000
                    H    2.195158018   14.410641168   0.000000000
                    H   -0.195687232   14.410746745   0.000000000
                    C    2.406293016    2.406154727   0.000000000
                    C    1.707835679    3.634617311   0.000000000
                    C    0.292503548    3.634686893   0.000000000
                    C   -0.406370543    2.405985560   0.000000000
                    C    0.320499229    1.199649414   0.000000000
                    C    1.679147719    1.199658283   0.000000000
                    H   -0.195319343    0.249196327   0.000000000
                    H    2.194843144    0.249337416   0.000000000
```

```
   K_POINTS automatic

  32 1 1 0 0 0
```

Density of States Input

```
&DOS

    prefix = ’11AGNR_yz’,
    outdir = ’/home/wsperkins/Quantum_Pyrene/11AGNR_ecutwft70_yzexpansion/248069/’,
    fildos = ’11AGNR_yz_fildos’,
    ngauss = 0,
    degauss = 0.00073499,
    DeltaE = 0.01,

/
```

Band Structure Input

```
&BANDS

    prefix = ’11AGNR_yz’,
    outdir = ’/home/wsperkins/Quantum_Pyrene/11AGNR_ecutwft70_yzexpansion/248069’,
    filband = ’11AGNR_ecutwft70_yzx_bands_filband’,

/
```

6.3 Carboxylic Acid Functionalized Cove GNR Quantum Espresso Code

Relax Input Calculation

```
&CONTROL

    calculation = ’relax’ ,
    pseudo_dir = ’/usr/software/espresso-5.1.1/pseudo/’ ,
    prefix = ’AcidCove’ ,
    verbosity = ’high’ ,
```

```
    forc_conv_thr = 1.0D-3 ,

/
&SYSTEM

    ibrav = 8,
    celldm(1) = 14,
    celldm(2) = 20,
    celldm(3) = 20,
    nat = 44,
    ntyp = 3,
    ecutwfc = 20 ,
    ecutrho = 80 ,
    occupations = 'smearing' ,
    degauss = 0.05D0 ,
    smearing = 'm-v' ,

/
&ELECTRONS

    conv_thr = 0.000001 ,

/
&IONS
/
ATOMIC_SPECIES

 O  15.99940  O.pbe-mt_fhi.UPF
 C  12.01070  C.pbe-mt_fhi.UPF
 H   1.00794  H.pbe-mt_fhi.UPF

ATOMIC_POSITIONS angstrom
```

C	1.991159772	2.197862641	0.000000000
C	3.215697147	1.421512653	0.000000000
C	3.216158305	-0.066772728	0.000000000
C	1.976223518	-0.828388024	0.000000000
C	0.740833672	-0.026078724	0.000000000
C	0.748149245	1.442585426	0.000000000
C	4.439402382	2.197861526	0.000000000
C	5.681927119	1.441592235	0.000000000

C	5.689583995	-0.027970266	0.000000000
C	4.454154134	-0.830023987	0.000000000
C	6.919464201	2.194101921	0.000000000
C	6.920473643	-0.744035931	0.000000000
C	1.991403011	3.669662771	0.000000000
C	4.439316627	3.669805120	0.000000000
C	6.919862403	3.673107706	0.000000000
C	0.748705679	4.425481280	0.000000000
C	0.742223981	5.894765385	0.000000000
C	1.977079738	6.699728397	0.000000000
C	3.216389101	5.935777147	0.000000000
C	3.215777436	4.446946577	0.000000000
C	4.455262635	6.697996324	0.000000000
C	5.690170354	5.894714735	0.000000000
C	5.682287990	4.425340360	0.000000000
C	6.921083017	6.611345850	0.000000000
C	4.467202214	-2.289709292	0.000000000
C	3.214087523	-3.020753490	0.000000000
C	1.964080489	-2.285349558	0.000000000
C	1.966820008	8.157675210	0.000000000
C	3.218467657	8.892055067	0.000000000
C	4.469629421	8.157488975	0.000000000
H	6.925946842	-1.858065675	0.000000000
H	6.926610664	7.725656965	0.000000000
H	5.428435336	-2.867787368	0.000000000
H	1.022434414	-2.896462970	0.000000000
H	1.025602656	8.770196622	0.000000000
H	5.431385419	8.734979685	0.000000000
O	4.538432481	11.042637943	0.000000000
H	4.167613270	12.081626890	0.000000000
C	3.168179146	10.420840481	0.000000000
O	1.996105484	11.165896444	0.000000000
C	3.151737522	-4.547900568	0.000000000
O	4.515429226	-5.182817764	0.000000000
H	4.132660090	-6.217309038	0.000000000
O	1.972151032	-5.281516959	0.000000000

K_POINTS automatic

8 1 1 0 0 0

Non Self-Consistent Input

```
&CONTROL

    calculation = ’nscf’ ,
    outdir = ’/home/wsperkins/Quantum_Pyrene/Carboxycove/262680’ ,
    pseudo_dir = ’/usr/software/espresso-5.1.1/pseudo’ ,
    prefix = ’AcidCove’ ,
    forc_conv_thr = 1.0D-3 ,

/
&SYSTEM

    ibrav = 8,
    celldm(1) = 14,
    celldm(2) = 20,
    celldm(3) = 20,
    nat = 44,
    ntyp = 3,
    ecutwfc = 20.0 ,
    ecutrho = 80.0 ,
    nbnd = 85,

/
&ELECTRONS

    conv_thr = 0.000001 ,

/
ATOMIC_SPECIES

 O   15.99940   O.pbe-mt_fhi.UPF
 C   12.01070   C.pbe-mt_fhi.UPF
 H    1.00794   H.pbe-mt_fhi.UPF

ATOMIC_POSITIONS angstrom


          C   1.991159772    2.197862641   0.000000000
          C   3.215697147    1.421512653   0.000000000
          C   3.216158305   -0.066772728   0.000000000
          C   1.976223518   -0.828388024   0.000000000
          C   0.740833672   -0.026078724   0.000000000
```

C	0.748149245	1.442585426	0.000000000
C	4.439402382	2.197861526	0.000000000
C	5.681927119	1.441592235	0.000000000
C	5.689583995	-0.027970266	0.000000000
C	4.454154134	-0.830023987	0.000000000
C	6.919464201	2.194101921	0.000000000
C	6.920473643	-0.744035931	0.000000000
C	1.991403011	3.669662771	0.000000000
C	4.439316627	3.669805120	0.000000000
C	6.919862403	3.673107706	0.000000000
C	0.748705679	4.425481280	0.000000000
C	0.742223981	5.894765385	0.000000000
C	1.977079738	6.699728397	0.000000000
C	3.216389101	5.935777147	0.000000000
C	3.215777436	4.446946577	0.000000000
C	4.455262635	6.697996324	0.000000000
C	5.690170354	5.894714735	0.000000000
C	5.682287990	4.425340360	0.000000000
C	6.921083017	6.611345850	0.000000000
C	4.467202214	-2.289709292	0.000000000
C	3.214087523	-3.020753490	0.000000000
C	1.964080489	-2.285349558	0.000000000
C	1.966820008	8.157675210	0.000000000
C	3.218467657	8.892055067	0.000000000
C	4.469629421	8.157488975	0.000000000
H	6.925946842	-1.858065675	0.000000000
H	6.926610664	7.725656965	0.000000000
H	5.428435336	-2.867787368	0.000000000
H	1.022434414	-2.896462970	0.000000000
H	1.025602656	8.770196622	0.000000000
H	5.431385419	8.734979685	0.000000000
O	4.538432481	11.042637943	0.000000000
H	4.167613270	12.081626890	0.000000000
C	3.168179146	10.420840481	0.000000000
O	1.996105484	11.165896444	0.000000000
C	3.151737522	-4.547900568	0.000000000
O	4.515429226	-5.182817764	0.000000000
H	4.132660090	-6.217309038	0.000000000
O	1.972151032	-5.281516959	0.000000000

K_POINTS automatic

```
  8 1 1 0 0 0
```

Density of States Input

```
&DOS

    prefix = ’AcidCove’,
    outdir = ’/home/wsperkins/Quantum_Pyrene/Carboxycove/262680’,
    fildos = ’CarboxyCove_fildos’,
    ngauss = 0,
    degauss = 0.00073499,
    DeltaE = 0.01,

/
```

Band Structure Input

```
&BANDS

    prefix = ’AcidCove’,
    outdir = ’/home/wsperkins/Quantum_Pyrene/Carboxycove/262680’,
    filband = ’CarboxyCove_bands_filband’,

/
```

6.4 Ester Functionalized Cove GNR Quantum Espresso Code

Relax Calculation Input

```
&CONTROL

    calculation = ’relax’ ,
    pseudo_dir = ’/usr/software/espresso-5.1.1/pseudo/’ ,
    prefix = ’estercove’ ,
    verbosity = ’high’ ,
    forc_conv_thr = 1.0D-3 ,
```

```
/
&SYSTEM

    ibrav = 8,
    celldm(1) = 14,
    celldm(2) = 20,
    celldm(3) = 20,
    nat = 50,
    ntyp = 3,
    ecutwfc = 20 ,
    ecutrho = 80 ,
    occupations = ’smearing’ ,
    degauss = 0.05D0 ,
    smearing = ’marzari-vanderbilt’ ,

/
&ELECTRONS

    conv_thr = 0.000001 ,

/
&IONS
/
ATOMIC_SPECIES

 C   12.01070   C.pbe-mt_fhi.UPF
 H    1.00794   H.pbe-mt_fhi.UPF
 O   15.99940   O.pbe-mt_fhi.UPF

ATOMIC_POSITIONS angstrom


                    C   10.854400000   -2.247400000   1.213200000
                    C   10.862200000   -3.666200000   1.220600000
                    C   10.860100000    2.007400000   1.220700000
                    C   10.853400000    0.588700000   1.213200000
                    C    9.617100000   -1.539100000   1.215800000
                    C    8.378700000   -2.243200000   1.219600000
                    C    8.376500000   -3.659400000   1.222800000
                    C    9.618900000   -4.330200000   1.220300000
                    C    9.616400000   -0.120700000   1.215800000
                    C    9.616400000    2.670900000   1.219900000
```

C	8.374700000	1.999300000	1.222400000
C	8.377700000	0.583000000	1.219400000
H	9.622600000	-5.410100000	1.209000000
H	9.619300000	3.750900000	1.208300000
C	7.147400000	-4.380500000	1.229200000
C	5.913200000	-3.672200000	1.226200000
C	4.681300000	-4.387700000	1.231700000
C	4.707200000	-5.805600000	1.252500000
C	5.914900000	-6.522000000	1.261100000
C	5.912400000	-2.251300000	1.219600000
C	4.680100000	-1.542100000	1.215800000
C	7.144300000	-1.539700000	1.218800000
C	7.143600000	-0.121600000	1.218700000
C	5.911500000	0.589200000	1.219500000
C	4.679600000	-0.120700000	1.215800000
C	5.911200000	2.010300000	1.226100000
C	4.678900000	2.724900000	1.231700000
C	7.145200000	2.719200000	1.228900000
C	5.911200000	4.860000000	1.261100000
C	4.703900000	4.143000000	1.252600000
C	5.954700000	-7.984100000	1.290000000
O	6.983500000	-8.633000000	1.195500000
O	4.725200000	-8.553400000	1.447300000
C	4.616700000	-9.958000000	1.506000000
C	5.950400000	6.322200000	1.290400000
O	6.979000000	6.971400000	1.196100000
O	4.720600000	6.890800000	1.447900000
C	4.612000000	8.295300000	1.508400000
H	3.801200000	-6.393400000	1.262200000
H	3.797700000	4.730500000	1.262200000
H	5.254200000	-10.366800000	2.290000000
H	4.903400000	-10.406200000	0.554600000
H	3.586900000	-10.241800000	1.722600000
H	5.246200000	8.702400000	2.296000000
H	4.902800000	8.745300000	0.559200000
H	3.581300000	8.578800000	1.721200000
C	7.114000000	4.139500000	1.242800000
H	8.004500000	4.750500000	1.249300000
C	7.117300000	-5.800700000	1.243100000
H	8.008300000	-6.411100000	1.250000000

```
  K_POINTS automatic

 8 1 1 0 0 0
```

6.5 Unfunctionalized Cove GNR Quantum Espresso Code

Relax Calculation Input

```
&CONTROL

    calculation = ’relax’ ,
    pseudo_dir = ’/usr/software/espresso-5.1.1/pseudo/’ ,
    prefix = ’cove’ ,
    verbosity = ’high’ ,
    forc_conv_thr = 1.0D-3 ,

/
&SYSTEM

    ibrav = 8,
    celldm(1) = 14,
    celldm(2) = 20,
    celldm(3) = 20,
    nat = 38,
    ntyp = 2,
    ecutwfc = 20 ,
    ecutrho = 80 ,
    occupations = ’smearing’ ,
    degauss = 0.05D0 ,
    smearing = ’marzari-vanderbilt’ ,

/
&ELECTRONS

    conv_thr = 0.000001 ,

/
&IONS
/
ATOMIC_SPECIES
```

```
 C   12.01070   C.pbe-mt_fhi.UPF
 H    1.00794   H.pbe-mt_fhi.UPF
ATOMIC_POSITIONS angstrom

        C   1.997100000    2.225600000   0.000000000
        C   3.226900000    1.510600000   0.000000000
        C   3.228300000    0.084100000   0.000000000
        C   1.995900000   -0.630100000   0.000000000
        C   0.796400000    0.083600000   0.000000000
        C   0.798800000    1.473600000   0.000000000
        C   4.455400000    2.222600000   0.000000000
        C   5.682100000    1.500900000   0.000000000
        C   5.669800000    0.083600000   0.000000000
        C   4.454900000   -0.637800000   0.000000000
        C   6.877100000    2.244000000   0.000000000
        C   6.996100000   -0.682700000   0.000000000
        C   1.998800000    3.643100000   0.000000000
        C   4.455900000    3.651400000   0.000000000
        C   6.877200000    3.635000000   0.000000000
        C   0.803300000    4.392400000   0.000000000
        C   0.804600000    5.782500000   0.000000000
        C   2.004700000    6.498900000   0.000000000
        C   3.233400000    5.787400000   0.000000000
        C   3.228900000    4.360800000   0.000000000
        C   4.459200000    6.512000000   0.000000000
        C   5.668500000    5.793100000   0.000000000
        C   5.681700000    4.375700000   0.000000000
        C   6.987700000    6.562000000   0.000000000
        C   4.400600000   -2.048800000   0.000000000
        C   3.188400000   -2.744500000   0.000000000
        C   1.990800000   -2.031900000   0.000000000
        C   2.003900000    7.900600000   0.000000000
        C   3.202500000    8.615900000   0.000000000
        C   4.410600000    7.923000000   0.000000000
        H   6.905000000   -1.653100000   0.000000000
        H   6.864600000    7.532700000   0.000000000
        H   5.294800000   -2.643500000   0.000000000
        H   3.179300000   -3.819700000   0.000000000
        H   1.054000000   -2.568400000   0.000000000
```

```
H   1.070100000   8.435300000   0.000000000
H   3.197600000   9.691100000   0.000000000
H   5.307000000   8.519600000   0.000000000

K_POINTS automatic

8 1 1 0 0 0
```

6.6 Chevron GNR Quantum Espresso Code

Relax Calculation Input

```
&CONTROL

    calculation = ’relax’ ,
    pseudo_dir = ’/usr/software/espresso-5.1.1/pseudo/’ ,
    prefix = ’C_chevron’ ,
    verbosity = ’high’ ,
    forc_conv_thr = 1.0D-3 ,

/
&SYSTEM

    ibrav = 8,
    celldm(1) = 32.31,
    celldm(2) = 5,
    celldm(3) = 20,
    nat = 108,
    ntyp = 2,
    ecutwfc = 5 ,
    ecutrho = 20 ,
    occupations = ’smearing’ ,
    degauss = 0.05D0 ,
    smearing = ’marzari-vanderbilt’ ,

/
&ELECTRONS

    conv_thr = 0.000001 ,
```

```
/
&IONS
/
ATOMIC_SPECIES

 C   12.01070   C.pbe-mt_fhi.UPF
 H    1.00794   H.pbe-mt_fhi.UPF

ATOMIC_POSITIONS angstrom


          C    -2.780848738   30.831723667   -1.049746108
          C    -1.986470207   32.327728762   -0.673730830
          C    -2.921363107   33.685142099   -1.140415924
          C    -4.551157692   33.620982056   -0.668048224
          C    -5.324093977   32.183300511   -1.099438877
          C    -4.467037631   30.765860902   -0.640485498
          C    -1.882099202   29.382131840   -0.631257810
          C    -2.597395393   27.867491768   -1.113232402
          C    -1.810902676   26.407071253   -0.602012558
          C    -0.148388073   26.440374262   -1.046239543
          C     0.600497259   27.940563036   -0.581572678
          C    -0.213133876   29.414085022   -1.099658969
          C     0.590109148   30.918227435   -0.673342301
          C    -4.267947670   27.771741878   -0.708456211
          C    -2.508612076   24.871988814   -1.043743797
          C     0.652875388   24.949923771   -0.618425946
          C     2.276484716   27.937022607   -1.071086446
          C     2.276943377   30.991874320   -1.061031304
          C     3.062271600   32.454704312   -0.588902875
          C     2.194347517   33.823548406   -1.061263085
          C     0.570345885   33.784292658   -0.573869947
          C    -0.270270036   32.374084776   -1.061315876
          C    -5.193654900   29.208898531   -1.077852371
          C    -6.851563736   29.052504846   -0.691417917
          C    -7.571906200   27.659224681   -1.344778719
          C    -6.666097576   26.287675238   -0.824373159
          C    -4.981936543   26.226360116   -1.163474873
          C    -4.167190636   24.738903726   -0.602942081
          C    -4.481314402   22.989737036   -0.944069098
          C    -2.953362168   22.118288914   -0.886413631
          C    -2.402408024   20.479722280   -0.692839246
```

C	-1.748598397	23.363456936	-0.628551678
C	-0.034728571	23.361433266	-0.981734670
C	0.514301679	20.525958761	-1.026582209
C	1.245976353	22.134106968	-0.823970428
C	2.733368987	23.166327659	-1.430859484
C	2.334653634	24.889632929	-1.019607870
C	3.185297895	26.448505999	-0.708058386
C	4.837480259	26.739200658	-1.319658102
C	5.532535534	28.151960303	-0.601749465
C	4.723704164	29.513332137	-1.140301522
C	3.081304759	29.457160338	-0.701276104
C	-6.062100599	22.205992474	-0.880249326
C	4.250424584	22.734364863	-0.525979422
C	5.294425159	24.158061439	-0.226736486
C	4.365634583	20.045538145	-1.580531915
C	5.999821047	22.258548600	-0.568539072
C	6.916231252	23.741028451	-0.789287701
C	6.402547447	25.451851112	-0.723844312
C	7.260625387	20.980301135	-0.892226278
C	5.923366310	19.837339123	-0.860330345
C	6.593333076	18.246847098	-1.046001788
C	4.121536475	17.189565691	-0.882097624
C	5.779040146	16.874826339	-0.380171299
C	3.419902051	18.858537946	-0.747153200
C	1.656199267	19.160517464	-0.918729583
C	0.882487767	17.639883487	-0.633500698
C	1.426936419	16.233972448	-1.390611015
C	3.036188136	15.831846197	-0.955829536
C	4.023721535	14.393269101	-0.714075429
C	3.044266730	12.957032151	-0.777650052
C	4.262449279	11.755091607	-0.799531867
C	5.922262375	12.180504947	-0.728287420
C	7.087116719	13.377854335	-1.037892753
C	-7.345402823	24.689071797	-0.917795915
C	-9.036974703	24.964983779	-0.423288964
C	-7.563946303	22.999084317	-0.507353471
C	-8.203898742	20.156377039	-1.316797860
C	-6.534064605	20.472792387	-0.686689418
C	-8.802389711	18.576888425	-0.842220811
C	-8.497199936	15.729768365	-0.282044103
C	-7.838197754	17.148973107	-1.103142130
C	-7.619006668	14.408001399	-1.021967250

C	-6.186324536	17.488022571	-0.623506434
C	-8.364785400	12.793226606	-0.880664233
C	-7.485324418	11.336619695	-1.287350724
C	-5.944188917	11.662265287	-0.598978935
C	-5.072772416	13.046830805	-1.050742411
C	-5.914542946	14.521655471	-0.710825982
C	-5.202716357	16.116415618	-1.081380975
C	-3.597212521	16.354659539	-0.580598222
C	-2.999337706	17.845353190	-1.040795520
C	-3.768914525	19.349004049	-0.808790268
C	-5.509568340	19.093768661	-1.186436368
H	-5.248055098	34.664353721	-1.095251619
H	2.834365576	34.905054325	-0.653178813
H	-7.554207201	30.168249001	-0.895107302
H	-9.217024291	30.562931733	-0.854569575
H	-1.669726339	17.842207001	-1.003273582
H	-0.447331808	17.588903096	-0.491390817
H	7.179519583	31.137112415	-0.762469768
H	5.354023584	30.677316723	-1.020535206
H	6.851235678	28.213274516	-0.803640533
H	-0.602574276	14.458186925	-0.797778465
H	0.757419582	15.166778349	-0.974500998
H	4.113532065	10.445187024	-0.991031554
H	-8.870714419	27.580650896	-1.016675616
H	-2.764670446	15.391730340	-0.903178656
H	-1.498687203	14.303495873	-0.854362763
H	-3.739600353	12.985130183	-0.925513113
H	1.885356879	12.290051042	-0.811642845
H	-5.171928626	10.598534496	-0.815699337
H	-6.602639954	32.173170882	-0.758142059
H	4.327767873	32.506799373	-0.986931146
H	7.157004872	10.012298509	-0.887602795
H	-10.337442108	9.205158152	-0.798255848
H	-2.288802665	34.811455438	-0.810500959
H	-0.121983369	34.868578249	-0.890451295

K_POINTS automatic

8 1 1 0 0 0

6.7 List of Abbreviations Used

AFM	atomic force microscopy
AGNR	armchair graphene nanoribbon
CNT	carbon nanotube
DCM	dichloromethane
DFT	density functional theory
DMF	N,N-dimethyl formamide
DOS	density of states
EBL	electron beam lithography
ECSA	electrochemically active surface area
EEM	excitation-emissio matrix
FE	Faraday efficiency
FET	field effect transistor
FMV	flavin mononucleotide
FWHM	full-width at half-max
GNR	graphene nanoribbon
GO	graphene oxide
GPC	gel permeation chromatography
HAADF-STEM	high-angle annular dark field scanning transmission electron microscopy
LDA	local density approximation
LIB	lithium ion battery
MALDI	matrix-assisted laser desorption ionization
MWCNT	multi wall carbon nanotube
NBS	N-bromo succinamide
NC-AFM	non-contact atomic force microscopy
NMR	nuclear magnetic resonance
NP	nanoparticle
OPT	organic phototransistor
P3HT	poly(3-hexylthiophene)
PAH	polycyclic aromatic hydrocarbon
PCC	pyridinium chlorochromate
PMMA	poly(methyl methacrylate)
PVDF	poly(vinylidene fluoride)
PmPV	poly(*m*-phenylenevinylene)
PVP	poly(vinylpyrrolidinone)
QD	quantum dot
RBLM	radial breathing like mode
RBM	radial breathing mode
rGO	reduced graphene oxide
RHE	reversible hydrogen electrode

SAM	self-assembled monolayer
SDS	sodium dodecyl sulfate
SEC	size exclusion chromatography
SEI	solid electrolyte interphase
SEM	scanning electron microscopy
STM	scanning tunneling microscopy
STS	scanning tunneling spectroscopy
SWCNT	single wall carbon nanotube
TEM	transmission electron microscopy
THF	tetrahydrofuran
TMS	trimethyl silyl
UHV	ultra high vacuum
XPS	X-ray photoelectron spectroscopy
XRD	X-ray diffraction
ZGNR	zig-zag graphene nanoribbon

Bibliography

[1] Novoselov, K. S.; Geim, A. K.; Morozov, S. V.; Jiang, D.; Zhang, Y.; Dubonos, S. V.; Grigorieva, I. V.; Firsov, A. A. *Science* **2004**, *306*, 666.

[2] Dresselhaus, M. S.; Dresselhaus, G. *Adv. Phys.* **2002**, *51*, 1.

[3] Spain, I. L. In *Chemistry and Physics of Carbon*; Walker, P. L., Thrower, P. A., Eds.; Dekker, New York, 1981; p 229.

[4] Shenderova, O. A.; Zhirnov, V. V.; Brenner, D. W. *Crit. Rev. Solid State Mater. Sci.* **2002**, *27*, 227.

[5] Krishnan, A.; Dujardin, E.; Treacy, M. M. J.; Hugdahl, J.; Lynum, S.; Ebbesen, T. W. *Nature* **1997**, *388*, 451.

[6] Dujardin, E.; Thio, T.; Lezec, H.; Ebbesen, T. W. *Appl. Phys. Lett.* **2001**, *79*, 2474.

[7] Shioyama, H. *J. Mat. Sci. Lett.* **2001**, *20*, 499.

[8] Orlita, M.; Faugeras, C.; Plochocka, P.; Neugebauer, P.; Martinez, G.; Maude, D. K.; et al., *Phys. Rev. Lett.* **2008**, *101*, 267601.

[9] Stoller, M. D.; Park, S.; Zhu, Y.; Ruoff, J.; Ruoff, R. S. *Nano Lett.* **2008**, *8*, 3498.

[10] Balandin, A. A.; Ghosh, S.; Bao, W.; Calizo, I.; Teweldebrhan, D.; Miao, F.; Lau, C. N. *Nano Lett.* **2008**, *8*, 902.

[11] Lee, C.; Wei, X.; Kysar, J. W.; Hone, J. *Science* **2008**, *321*, 385.

[12] Nair, R. R.; Blake, P.; Grigorenko, A. N.; Novoselov, K. S.; Booth, T. J.; Stauber, T.; Peres, N. M. R.; Geim, A. K. *Science* **2008**, *320*, 1308.

[13] Del Rio-Castillo, A. E.; Merino, C.; Diez-Barra, E.; Vazquez, E. *Nano Res.* **2014**, *7*, 963.

[14] Alanyalioglu, M.; Segura, J. J.; Oro-Sole, J.; Casan-Pastor, N. *Carbon* **2012**, *50*, 142.

[15] Yu, L.; Yasuda, S.; Murakoshi, K. *Trans. Mater. Res. Soc. Jpn.* **2012**, *37*, 209.

[16] Xu, M.; Fujita, D.; Sagisaka, K.; Watanabe, E.; Hanagata, N. *ACS Nano* **2011**, *5*, 1522.

[17] Gao, J.-H.; Ishida, N.; Scott, I.; Fujita, D. *Carbon* **2012**, *50*, 1674.

[18] Somani, P. R.; Somani, S. P.; Umeno, M. *Chem. Phys. Lett.* **2006**, *430*, 56.

[19] Sun, Z.; Yan, Z.; Yao, J.; Beitler, E.; Zhu, Y.; Tour, J. M. *Nature* **2010**, *468*, 549.

[20] Wu, T.; Ding, G.; Shen, H.; Wang, H.; Sun, L.; Jiang, D.; Xie, X.; Jiang, M. *Adv. Funct. Mater.* **2013**, *23*, 198.

[21] Seah, C.-M.; Chai, S.-P.; Mohamed, A. R. *Carbon* **2014**, *70*, 1.

[22] Li, Z.; Wu, P.; Wang, C.; Fan, X.; Zhang, W.; Zhai, W.-H.; Zhai, Z.-F.; Zeng, C.-G.; Li, Z.-Y.; Yang, J.-L.; Hou, J.-G. *ACS Nano* **2011**, *5*, 3385.

[23] Gan, X.; Zhou, H.; Zhu, B.; Yu, X.; Jia, Y.; Sun, B.; et al., *Carbon* **2012**, *50*, 306.

[24] Sharma, S.; Kalita, G.; Hirano, R.; Shinde, S. M.; Papon, R.; Ohtani, H.; Tanemura, M. *Carbon* **2014**, *72*, 66.

[25] Ruan, G.; Sun, Z.; Peng, Z.; Tour, J. M. *ACS Nano* **2011**, *5*, 7601.

[26] Lee, J.-K.; Lee, S.; Kim, Y.-I.; Kim, J.-G.; Min, B.-K.; Lee, K.-I.; Park, Y.; John, P. *Sci. Rep.* **2014**, *4*, 5682.

[27] Yao, Y.; Li, Z.; Lin, Z.; Moon, K.-S.; Agar, J.; Wong, C. *J. Phys. Chem. C* **2011**, *115*, 5232.

[28] Campos-Delgado, J.; Botello-Mndez, A. R.; Algara-Siller, G.; Hackens, B.; Pardeon, T.; Kaiser, U.; et al., *Chem. Phys. Lett.* **2013**, *584*, 142.

[29] Dai, G.-P.; Cooke, P. H.; Deng, S. *Chem. Phys. Lett.* **2012**, *531*, 193.

[30] Gadipelli, S.; Calizo, I.; Ford, J.; Cheng, G.; Hight Walker, A. R.; Yildirim, T. *J. Mater. Chem.* **2011**, *21*, 16057.

[31] Paul, R. K.; Badhulika, S.; Niyogi, S.; Haddon, R. C.; Boddu, V. M.; Costales-Nieves, C.; Bozhilov, K. N.; Mulchandani, A. *Carbon* **2011**, *49*, 3789.

[32] Guermoune, A.; Chari, T.; Popescu, F.; Sabri, S. S.; Guillemette, J.; Skulason, H. S.; et al., *Carbon* **2011**, *49*, 4204.

[33] Stutter, P. W.; Flege, J.-I.; Stutter, E. *Nat. Mater.* **2008**, *7*, 406.

[34] Ueta, H.; Saida, M.; Nakai, C.; Yamada, Y.; Sasaki, M.; Yamamoto, S. *Surf. Sci.* **2004**, *560*, 183.

[35] Marchini, S.; Gunther, S.; Wintterlin, J. *Phys. Rev. B* **2007**, *76*, 075429.

[36] Coraux, J.; Diaye, A. T. N.; Busse, C.; Michely, *Nano* **2008**, *8*, 565.

[37] Gall, N. R.; Rut'kov, E. V.; Tontegode, Y. *Phys. Solid State* **2004**, *46*, 371.

[38] Nandamuri, G.; Rouminov, S.; Solanki, R. *Nanotechnology* **2010**, *21*, 145604.

[39] De Arco, L. G.; Zhang, Y.; Kumar, A.; Chongwu, Z. *IEEE Trans. Nanotechnol.* **2009**, *8*, 135.

[40] Chen, Z.; Ren, W.; Liu, B.; Gao, L.; Pei, S.; Wu, Z.-S. *Carbon* **2010**, *48*, 3543.

[41] Kim, K. S.; Zhao, Y.; Jang, H.; Lee, S. Y.; Kim, J. M.; Kim, K. S.; Ahn, J.-H.; Kim, P.; Choi, J.-Y.; Hong, B. H. *Nature* **2009**, *457*, 706.

[42] Lee, Y.; Bae, S.; Jang, H.; Jang, S.; Zhu, S.-E.; Sim, S. H.; Song, Y. I.; Hong, Y. H.; Ahn, J.-H. *Nano Lett.* **2010**, *10*, 490.

[43] Reina, A.; Jia, X.; Ho, J.; Nezich, D.; Son, H.; Bulovic, V.; Dresselhaus, M. S.; Kong, J. *Nano Lett.* **2009**, *9*, 30.

[44] Reina, A.; Son, H.; Jiao, L.; Fan, B.; Dresselhaus, M. S.; Liu, Z.; et al., *J. Phys. Chem. C* **2008**, *112*, 17741.

[45] Bae, S.; Kim, H.; Lee, Y.; Xu, X.; Park, J.-S.; Zheng, Y.; et al., *Nat. Nanotechnol.* **2010**, *5*, 574.

[46] Juang, Z.-Y.; Wu, C.-Y.; Lu, A.-Y.; Su, C.-Y.; Leou, K.-C.; Chen, F.-R.; Tsai, C.-H. *Carbon* **2010**, *48*, 3169.

[47] Byun, S. J.; Lim, H.; Shin, G. Y.; Han, T. H.; Oh, S. H.; Ahn, J. H.; Choi, H. C.; Lee, T. W. *J. Phys. Chem. Lett.* **2011**, *2*, 493.

[48] Ismach, A.; Druzgalski, C.; Penwell, S.; Schwartzberg, A.; Zheng, M.; Javey, A.; Bokor, J.; Zhang, Y. *Nano Lett.* **2010**, *10*, 1542.

[49] Yoon, W.; Lee, Y.; Jang, H.; Jang, M.; Kim, J. S.; Lee, H. S.; Im, S.; Boo, D. W.; Park, J.; Ju, S.-Y. *Carbon* **2015**, *81*, 629.

[50] Li, X.; Wang, X.; Zhang, L.; Lee, S.; Dai, H. *Science* **2008**, *319*, 1229.

[51] Wu, Z.-S.; Ren, W.; Gao, L.; Liu, B.; Zhao, J.; Cheng, H.-M. *Nano Res.* **2010**, *3*, 16.

[52] Paiva, M. C.; Xu, W.; Fernanda Proenca, M.; Novais, R. M.; Lgsgaard, E.; Besenbacher, F. *Nano Lett.* **2010**, *10*, 1764.

[53] Shinde, D. B.; Debgupta, J.; Kushwaha, A.; Aslam, M.; Pillai, V. K. *J. Am. Chem. Soc.* **2011**, *133*, 4168.

[54] Li, Y.-S.; Liao, J.-L.; Wang, S.-Y.; Chiang, W.-H. *Sci. Rep.* **2016**, *6*, 22755.

[55] Kumar, P.; Panchakarla, L. S.; Rao, C. N. R. *Nanoscale* **2011**, *3*, 2127.

[56] Talyzin, A. V.; Luzan, S.; Anoshkin, I. V.; Nasibulin, A. G.; Jiang, H.; Kauppinen, E. I.; Mikoushkin, V. M.; Shnitov, V. V.; Marchenko, D. E.; Noreus, D. *ACS Nano* **2011**, *5*, 5132.

[57] Bai, J.; Duan, X.; Huang, Y. *Nano Lett.* **2009**, *9*, 2083.

[58] Han, M. Y.; Ozyilmaz, B.; Zhang, Y.; Kim, P. *Phys. Rev. Lett.* **2007**, *98*, 206805.

[59] Zhang, X.; Yazyev, O. V.; Feng, J.; Xie, L.; Tao, C.; Chen, Y.-C.; Jiao, L.; Pedramrazi, Z.; Zettl, A.; Louie, S. G.; Dai, H.; Crommie, M. F. *ACS Nano* **2013**, *7*, 198.

[60] Sommer, B.; Sonntag, J.; Ganczarczyk, A.; Braam, D.; Prinz, G.; Lorke, A.; Geller, M. *Sci. Rep.* **2015**, *5*, 7781.

[61] Dauber, J.; Terres, B.; Volk, C.; Trellenkamp, S.; Stampfer, C. *Appl. Phys. Lett.* **2014**, *104*, 083105.

[62] Han, M. Y.; Brant, J. C.; Kim, P. *Phys. Rev. Lett.* **2010**, *104*, 056801.

[63] Jeong, S.-J.; Jo, S.; Lee, J.; Yang, K.; Lee, H.; Lee, C.-S.; Park, H.; Park, S. *Nano Lett.* **2016**, *16*, 5378.

[64] Cai, J.; Ruffieux, P.; Jaafar, R.; Bieri, M.; Braun, T.; Blankenburg, S.; Muoth, M.; Seitsonen, A. P.; Saleh, M.; Feng, X.; Mullen, K.; Fasel, R. *Nature* **2010**, *466*, 470.

[65] Chen, Y.-C.; de Oteyza, D. G.; Pedramrazi, Z.; Chen, C.; Fischer, F. R.; Crommie, M. F. *ACS Nano* **2013**, *7*, 6123.

[66] Zhang, H.; Lin, H.; Sun, K.; Chen, L.; Zagranyarski, Y.; Aghdassi, N.; Duhm, S.; Li, Q.; Zhong, D.; Li, Y.; Mullen, K.; Fuchs, H.; Chi, L. *J. Am. Chem. Soc.* **2015**, *137*, 4022.

[67] Bieri, M.; Nguyen, M.-T.; Groning, O.; Cai, J.; Treier, M.; Alt-Mansour, K.; Ruffieux, P.; Pignedoli, C. A.; Passerone, D.; Kastler, M.; Mullen, K.; Fasel, R. *J. Am. Chem. Soc.* **2010**, *132*, 16669.

[68] Nguyen, M. T.; Pignedoli, C. A.; Passerone, D. *Phys. Chem. Chem. Phys.* **2011**, *13*, 154.

[69] Wang, W. H.; Shi, X. Q.; Wang, S. Y.; Van Hove, M. A.; Lin, N. *Journal of the American Chemical Society* **2011**, *133*, 13264.

[70] Grill, L.; Dyer, M.; Lafferentz, L.; Persson, M.; Peters, M. V.; Hecht, S. *Nat. Nanotechnol.* **2007**, *2*, 687.

[71] Ruffieux, P.; Wang, S.; Yang, B.; Sanchez-Sanchez, C.; Liu, J.; Dienel, T.; Talirz, L.; Shinde, P.; Pignedoli, C. A.; Passerone, D.; Dumslaff, T.; Feng, X.; Mullen, K.; Fasel, R. *Nature* **2016**, *531*, 489.

[72] Cloke, R. R.; Marangoni, T.; Nguyen, G. D.; Joshi, T.; Rizzo, D. J.; Bronner, C.; Cao, T.; Louie, S. G.; Crommie, M. F.; Fischer, F. R. *J. Am. Chem. Soc.* **2015**, *137*, 8872.

[73] Kawai, S.; Saito, S.; Osumi, S.; Yamaguchi, S.; Foster, A. S.; Spijker, P.; Meyer, E. *Nat. Commun.* **2015**, *6*, 8098.

[74] Nguyen, G. D.; Toma, F. M.; Cao, T.; Pedramrazi, Z.; Chen, C.; Rizzo, D. J.; Joshi, T.; Bronner, C.; Chen, Y.-C.; Favaro, M.; Lousie, S. G.; Fischer, F. R.; Crommie, M. F. *J. Phys. Chem. C.* **2016**, *120*, 2684.

[75] Marangoni, T.; Haberer, D.; Rizzo, D. J.; Cloke, R. R.; Fischer, F. R. *Chem-Eur. J.* **2016**, *22*, 13037.

[76] Bronner, C.; Stremlau, S.; Gille, M.; Brausse, F.; Haase, A.; Hecht, S.; Tegeder, P. *Angew. Chem. Int. Ed.* **2013**, *52*, 4422.

[77] Zhang, Y.; Zhang, Y.; Li, G.; Lu, J.; Lin, X.; Du, S.; Berger, R.; Feng, X.; Mullen, K.; Gao, H.-J. *Appl. Phys. Lett.* **2014**, *105*, 023101.

[78] Cai, J.; Pignedoli, C. A.; Talirz, L.; Ruffieux, P.; Sode, H.; Liang, L.; Meunier, V.; Berger, R.; Li, R.; Feng, X.; Mullen, K.; Fasel, R. *Nat. Nanotechnol.* **2014**, *9*, 896.

[79] Carbonell-Sanroma, E.; Brandimarte, P.; Balog, R.; Corso, M.; Kawai, S.; Garcia-Lekue, A.; Saito, S.; Yamaguchi, S.; Meyer, E.; Sanchez-Portal, D.; Pascual, J. I. *Nano Lett.* **2017**, *17*, 50.

[80] Chen, Y.-C.; Cao, T.; Chen, C.; Pedramrazi, Z.; Haberer, D.; de Oteyza, D. G.; Fischer, F. R.; Louie, S. G.; Crommie, M. F. *Nat. Nanotechnol.* **2015**, *10*, 156.

[81] Yang, X.; Dou, X.; Rouhanipour, A.; Zhi, L.; Rader, H. J.; Mullen, K. *J. Am. Chem. Soc.* **2008**, *130*, 4216.

[82] Dossel, L., L. F.sel; Gherghel, L.; Feng, X.; Mullen, K. *Angew. Chem. Int. Ed.* **2011**, *50*, 2540.

[83] El Gemayel, M.; Narita, A.; Dossel, L. F.; Sundaram, R. S.; Kiersnowski, A.; Pisula, W.; Hansen, M. R.; Ferrari, A. C.; Orgiu, E.; Feng, X.; Mullen, K.; Samori, P. *Nanoscale* **2014**, *6*, 6301.

[84] Schwab, M. G.; Narita, A.; Hernandez, Y.; Balandina, T.; Mali, K. S.; De Feyter, S.; Feng, X.; Mullen, K. *J. Am. Chem. Soc.* **2012**, *134*, 18169.

[85] Vo, T. H.; Shekhirev, M.; Lipatov, A.; Korlacki, R. A.; Sinitskii, A. *Faraday Discuss.* **2014**, *173*, 105.

[86] Vo, T. H.; Shekhirev, M.; Kunkel, D. A.; Morton, M. D.; Berglund, E.; Kong, L.; Wilson, P. M.; Dowben, P. A.; Enders, A.; Sinitskii, A. *Nat. Commun.* **2014**, *5*, 3189.

[87] Narita, A. et al. *Nat. Chem.* **2014**, *6*, 126.

[88] Narita, A.; Feng, X. *Nat. Chem.* **2014**, *6*, 126.

[89] Abbas, A. N.; Liu, G.; Narita, A.; Orosco, M.; Feng, X.; Mullen, K.; Zhou, C. *J. Am. Chem. Soc.* **2014**, *136*, 7555.

[90] Konnerth, R.; Cervetti, C.; Narita, A.; Feng, X.; Mullen, K.; Hoyer, A.; Burghard, M.; Kern, K.; Dressel, M.; Bogani, L. *Nanoscale* **2015**, *7*, 12807.

[91] Narita, A.; Verzhbitskiy, I. A.; Frederickx, W.; Mali, K. S.; Jensen, S. A.; Hansen, M. R.; Bonn, M.; De Feyter, S.; Casiraghi, C.; Feng, X.; Mullen, K. *ACS Nano* **2014**, *8*, 11622.

[92] Bennett, P. B.; Pedramrazi, Z.; Madani, A.; Chen, Y.-C.; de Oteyza, D. G.; Chen, C.; Fischer, F. R.; Crommie, M. F.; Bokor, J. *Appl. Phys. Lett.* **2013**, *103*, 253114.

[93] Zschieschang, U.; Klauk, H.; Muller, I. B.; Strudwick, A. J.; Hintermann, T.; Schwab, M. G.; Narita, A.; Feng, X.; Mullen, K.; Weitz, R. T. *Adv. Electron. Mater.* **2015**, *1*, 1400010.

[94] Fantuzzi, P.; Martini, L.; Candini, A.; Corradini, V.; del Pennino, U.; Hu, Y.; Feng, X.; Mllen, K.; Narita, A.; Affronte, M. *Carbon* **2016**, *104*, 112.

[95] Ferrari, A. C.; Basko, D. M. *Nat. Nanotechnol.* **2013**, *8*, 235.

[96] Pisana, S.; Lazzeri, M.; Casiraghi, C.; Novoselov, K. S.; Geim, A. K.; Ferrari, A. C.; Mauri, F. *Nat. Mater.* **2007**, *6*, 198.

[97] Ferrari, A. C. *Solid State Commun.* **2007**, *143*, 47.

[98] Gillen, R.; Mohr, M.; Maultzsch, J. *Phys. Status Solidi-R* **2010**, *247*, 2941.

[99] Verzhbitskiy, I. A.; Corato, M. D.; Ruini, A.; Molinari, E.; Narita, A.; Hu, Y.; Schwab, M. G.; Bruna, M.; Yoon, D.; Milana, S.; Feng, X.; Mullen, K.; Ferrari, A. C.; Casiraghi, C.; Prezzi, D. *Nano Lett.* **2016**, *16*, 3442.

[100] Gillen, R.; Mohr, M.; Thomsen, C.; Maultzsch, J. *Phys. Rev. B* **2009**, *80*, 155418.

[101] Thomsen, C.; Reich, S. *Phys. Rev. Lett.* **2000**, *85*, 5214.

[102] Maghsoumi, A.; Brambilla, L.; Castiglioni, C.; Mullen, K.; Tommasini, M. *J. Raman Spectrosc.* **2015**, *46*, 757.

[103] Yang, L.; Park, C.-H.; Son, Y.-W.; Cohen, M. L.; Louie, S. G. *Physical Review Letters* **2007**, *99*, 186801.

[104] Gianozzi, P.; Baroni, S.; Bonini, N.; Calandra, M.; Car, R.; Cavazzoni, C.; Ceresoli, D.; Chiarotti, G. L.; Cococcioni, M.; Dabo, I. *J. Phys. Chem. C* **2009**, *21*, 395502.

[105] Son, Y.-W.; Cohen, M. L.; Louie, S. G. *Phys. Rev. Lett.* **2006**, *97*, 216803.

[106] Petta, J. R.; Johnson, A. C.; Taylor, J. M.; Laird, E. A.; Yacoby, A.; Lukin, M. D.; Marcus, C. M.; Hanson, M. P.; Gossard, A. C. *Science* **2005**, *309*, 2180.

[107] Cordourier-Maruri, G.; Omar, Y.; de Coss, R.; Bose, S. *Phys. Rev. B* **2014**, *89*, 075426.

[108] Xiong, Y.-J. *Physica B* **2013**, *431*, 32.

[109] Chiu, K. L.; Connolly, M. R.; Cresti, A.; Chua, C.; Chorley, S. J.; Sfigakis, F.; Milana, S.; Ferrari, A. C.; Griffiths, J. P.; Jones, G. A. C.; Smith, C. G. *Phys. Rev. B* **2012**, *85*, 205452.

[110] Raimondi, F.; Scherer, G. G.; Kotz, R.; Wokaun, A. *Angew. Chem. Int. Ed.* **2005**, *44*, 2190.

[111] Guo, Y.; Hu, J.-S.; Wan, L.-J. *Adv. Mater.* **2008**, *20*, 2878.

[112] Torres Galvis, H. M.; Bitter, J. H.; Khare, C. B.; Ruitenbeek, M.; Dugulan, A. I.; de Jong, K. P. *Science* **2012**, *335*, 835.

[113] Chen, C. et al. *Science* **2014**, *343*, 1339.

[114] Kim, H.; Robertson, A. W.; Kim, S. O.; Kim, J. M.; Warner, J. H. *ACS Nano* **2015**, *9*, 5947.

[115] Whipple, D. T.; Kenis, P. J. A. *J. Phys. Chem. Lett* **2010**, *1*, 3451.

[116] Coq, B.; Figueras, F. *Coord. Chem. Rev.* **1998**, *178*, 1753.

[117] Chen, Y.; Li, C. W.; Kanan, M. W. *J. Am. Chem. Soc.* **2012**, *134*, 19969.

[118] Reske, R.; Mistry, H.; Behafarid, F.; Cuenya, B. R.; Strasser, P. *J. Am. Chem. Soc.* **2014**, *136*, 6978.

[119] Mistry, H.; Reske, R.; Zheng, Z.; Zhao, Z.-J.; Greeley, J.; Strasser, P.; Cuenya, B. R. *J. Am. Chem. Soc.* **2014**, *136*, 16473.

[120] Zhu, W.; Zhang, Y.-J.; Zhang, H.; Lv, H.; Li, Q.; Michalsky, R.; Peterson, A. A.; Sun, S. *J. Am. Chem. Soc.* **2014**, *136*, 16132.

[121] Gao, D.; Zhou, H.; Wang, J.; Miao, S.; Yang, F.; Wang, G.; Wang, J.; Bao, X. *J. Am. Chem. Soc.* **2015**, *137*, 4288.

[122] Feng, X.; Jiang, K.; Fan, S.; Kanan, M. W. *J. Am. Chem. Soc.* **2015**, *137*, 4606.

[123] Hall, A. S.; Yoon, Y.; Wuttig, A.; Surendranath, Y. *J. Am. Chem. Soc.* **2015**, *137*, 14834.

[124] Liu, M. et al. *Nature* **2016**, *537*, 382.

[125] Ertl, G. *Angew. Chem. Int. Ed.* **1990**, *29*, 1219.

[126] Somorjai, G. A. *Surf. Sci.* **1994**, *299*, 849.

[127] Zhu, W.; Michalsky, R.; Metin, O.; Lv, H.; Guo, S.; Wright, C. J.; Sun, X.; Peterson, A. A. *J. Am. Chem. Soc.* **2013**, *135*, 16833.

[128] Hori, Y.; Murata, A.; Kikuchi, K.; Suzuki, S. *J. Chem. Soc., Chem. Commun.* **1987**, *10*, 728.

[129] Hori, Y.; Wakebe, H.; Tsukamoto, T.; Koga, O. *Electrochim. Acta.* **1994**, *39*, 1833.

[130] Kim, D.; Resasco, J.; Yu, Y.; Asiri, A. M.; Yang, P. *Nat. Commun.* **2014**, *5*, 4948.

[131] Koh, J. H.; Jeon, H. S.; Jee, M. S.; Nursanto, E. B.; Lee, H.; Hwang, Y. J.; Min, B. K. *J. Phys. Chem. C* **2015**, *119*, 883.

[132] Manthiram, K.; Surendranath, Y.; Alivisatos, A. P. *J. Am. Chem. Soc.* **2014**, *136*, 7237.

[133] Zhou, X.; Qiao, J.; Yang, L.; Zhang, J. *Adv. Energy Mater.* **2014**, *4*, 1301523.

[134] Fujigaya, T.; Kim, C.; Hamasaki, Y.; Nakashima, N. *Sci. Rep.* **2016**, *6*, 21314.

[135] Yin, H.; Tang, H.; Wang, D.; Gao, Y.; Tang, Z. *ACS Nano* **2012**, *6*, 8288.

[136] Shao, Y.; Yin, G.; Gao, Y. *J. Power Sources* **2007**, *171*, 558.

[137] Shao, Y.; Yin, G.; Gao, Y.; Shi, P. *J. Electrochem. Soc.* **2006**, *153*, A1093.

[138] Wang, X.; Tan, Z.; Zeng, M.; Wang, J. *Sci. Rep.* **2014**, *4*, 4437.

[139] Ding, M.; Tang, Y.; Star, A. *J. Phys. Chem. Lett.* **2013**, *4*, 147.

[140] Navalon, S.; Dhakshinamoorthy, A.; Alvaro, M.; Garcia, H. *Coord. Chem. Rev.* **2016**, *312*, 99.

[141] Liu, M.; Zhang, R.; Chen, W. *Chem. Rev.* **2014**, *114*, 5117.

[142] Zhang, S.; Shao, Y.; Liao, H.; Liu, J.; Aksay, I.; In, G.; Lin, Y. *Chem. Mater.* **2011**, *23*, 1079.

[143] Gracia-Espino, E.; Hu, G.; Shchukarev, A.; Wagberg, T. *J. Am. Chem. Soc.* **2014**, *136*, 6626.

[144] Zhou, J.; Zhou, X.; Sun, W.; Li, R.; Murphy, M.; Ding, Z.; Sun, X.; Sham, T. *Chem. Phys. Lett* **2007**, *437*, 229.

[145] Khomyakov, P.; Giovannetti, G.; Rusu, P.; Brocks, G.; van den Brink, J.; Kelly, P. *Phys. Rev. B* **2009**, *79*, 195425.

[146] Coloma, F.; Sepulveda-Escribano, A.; Rodriguez-Reinoso, F. *J. Catal.* **1995**, *154*, 299.

[147] Chambers, A.; Nemes, T.; Rodriguez, N.; Baker, T. T. *J. Phys. Chem. B* **1998**, *102*, 2251.

[148] Truong-Phuoc, L.; Pham-Huu, C.; Da Costa, V.; Janowska, I. *Chem. Commun.* **2014**, *50*, 14433.

[149] Wei, W.; Wang, G.; Yang, S.; Feng, X.; Mullen, K. *J. Am. Chem. Soc.* **2015**, *137*, 5576.

[150] Khoa, N.; Kim, S.; Yoo, D.; Kim, E.; Hahn, S. *Appl. Catal., A* **2014**, *469*, 159.

[151] Li, Y.; Gao, W.; Ci, L.; Wang, C.; Ajayan, P. *Carbon* **2010**, *48*, 1124.

[152] Girishkumar, G.; Hall, T.; Vinodgopal, K.; Kamat, P. *J. Phys. Chem. B* **2006**, *110*, 107.

[153] Jeong, G.; Suzuki, S.; Kobayahi, Y. *Nanotechnology* **2009**, *20*, 285708.

[154] Lee, W.; Maiti, U.; Lee, J.; Lim, J.; Han, T.; Kim, S. *Chem. Commun.* **2014**, *50*, 6818.

[155] Liu, Z.-F.; Wei, S.; Yoon, H.; Adak, O.; Ponce, I.; Jiang, Y.; Jang, W.-D.; Campos, L. M.; Venkataraman, L.; Neaton, J. B. *Nano Lett.* **2014**, *14*, 5365.

[156] Li, X.; Antonietti, M. *Chem. Soc. Rev* **2013**, *42*, 6593.

[157] Wang, Y.; Nie, Y.; Ding, W.; Chen, S.; Xiong, K.; Qi, K.; Zhang, Y.; Wang, J.; Wei, Z. *Chem. Commun.* **2015**, *51*, 8942.

[158] Zhou, Y.; Liu, C.; Fan, S. *J. Mater. Chem.* **2015**, *3*, 19539.

[159] Kim, M.; Hwang, S.; Yu, J. *J. Mater. Chem.* **2007**, *17*, 1656.

[160] Subramanian, V.; Wolf, E.; Kamat, P. *J. Am. Chem. Soc.* **2004**, *126*, 4943.

[161] Wang, Y.; Yao, J.; Li, H.; Su, D.; Antonietti, M. *J. Am. Chem. Soc.* **2011**, *133*, 2362.

[162] Su, H.; Zhang, K.; Zhang, B.; Wang, H.; Yu, Q.; Li, X.; Antonietti, M.; Chen, J. *J. Am. Chem. Soc.* **2017**, *139*, 811.

[163] Hu, S.; Yang, L.; Tian, Y.; Wi, X.; Ding, J.; Zhong, J.; Chu, P. *Appl. Catal., B* **2015**, *163*, 611.

[164] Cai, Y.; Li, X.; Zhang, Y.; Wi, X.; Wang, K.; Chen, J. *Angew. Chem. Int. Ed.* **2013**, *52*, 11822.

[165] Saleh, M.; Baumgarten, M.; Mavrinskiy, A.; Schafer, T.; Mullen, K. *Macromolecules* **2010**, *43*, 137.

[166] Martinelli, J.; Watson, D.; Freckmann, D.; Barder, T. E.; Buchwald, S. *J. Org. Chem.* **2008**, *73*, 7102.

[167] Kim, S.; Kim, B.; In, J. *Synthesis* **2009**, *2009*, 1963.

[168] Mullen, K. *ACS Nano* **2014**, *8*, 6531.

[169] Cao, Z.; Kim, D.; Hong, D.; Yu, Y.; Xu, J.; Lin, S.; Wen, X.; Nichols, E. M.; Jeong, K.; Reimer, J. A.; Yang, P.; Chang, C. J. *J. Am. Chem. Soc.* **2016**, *138*, 8120.

[170] Peng, S.; Lee, Y.; Wang, C.; Yin, H.; Dai, S.; Sun, S. *Nano Res.* **2008**, *1*, 229.

[171] Lee, J.; Kim, J.; Hyeon, T. *Adv. Mater.* **2006**, *18*, 2073.

[172] Stein, A.; Wang, Z.; Fierke, M. A. *Adv. Mater.* **2009**, *21*, 265.

[173] Luo, J.; Jang, H. D.; Huang, J. *ACS Nano* **2013**, *7*, 1464.

[174] McEnaney, B. *Carbon* **1988**, *26*, 267.

[175] Rodriguez-Reinoso, F.; Garrido, J.; Martin-Martinez, J.; Molina-Sabio, M.; Terregrosa, R. *Carbon* **1989**, *27*, 23.

[176] Sing, K. In *Adsorption by Powders and Porous Solids, 2nd ed.*; Rouquerol, J., Rouquerol, F., Llewellyn, P., Maurin, G., Sing, K., Eds.; Elsevier: Oxford, 2014; Chapter Adsorption by Active Carbons, p 339.

[177] Thommes, M.; Cychosz, K.; Neimark, A. In *Novel Carbon Adsorbents*; Tascon, J., Ed.; Elsevier: Oxford, 2012; Chapter Advanced Physical Adsorption Characterization of Nanoporous Carbons, p 111.

[178] Blanco Lopez, M.; Martinez-Alonso, A.; Tascon, J. *Carbon* **2000**, *38*, 1177.

[179] Ehrburger, P.; Pusset, N.; Dziedzinl, P. *Carbon* **1992**, *30*, 1105.

[180] Thommes, M.; Morlay, C.; Ahmad, R.; Joly, J. *Adsorption* **2011**, *17*, 653.

[181] Hamelin, A. *J. Electroanal. Chem. Interfacial Electrochem* **1984**, *165*, 167.

[182] Hamelin, A.; Lipkowski, J. *J. Electroanal. Chem. Interfacial Electrochem* **1984**, *171*, 317.

[183] Somorjai, G.; Li, Y. *Introduction to Surface Chemistry and Catalysis, 2nd ed.*; J. Wiley & Sons: Hoboken, 2011; p 390.

[184] Pramod, P.; Soumya, C.; Thomas, K. G. *J. Phys. Chem. Lett.* **2011**, *2*, 775.

[185] Choi, H. C.; Shim, M.; Bangsaruntip, S.; Dai, H. *J. Am. Chem. Soc.* **2002**, *124*, 9058.

[186] Kong, B.; Jung, D.; Oh, S.; Han, C.; Jung, H. *J. Phys. Chem. C* **2007**, *111*, 9377.

[187] Gautier, L.; Le Borgne, V.; Delegan, N.; Pandiyan, R.; El Khakani, M. *Nanotechnology* **2015**, *26*, 045706.

[188] Giovannetti, G.; Khomyakov, P.; Brocks, G.; Karpan, V.; van den Brink, J.; Kelly, P. *Phys. Rev. Lett.* **2008**, *101*, 026803.

[189] Peng, X.; Tang, F.; Copple, A. *Phys. Condens. Matter* **2012**, *24*, 075501.

[190] Suzuki, S.; Bower, C.; Watanabe, Y.; Zhou, O. *Appl. Phys. Lett.* **2000**, *76*, 4007.

[191] Liu, J.; Li, B.; Tan, Y.; Giannakopoulos, A.; Sanchez-Sanchez, C.; Beljonne, D.; Ruffieux, P.; Fase, R.; Feng, X.; Mullen, K. *J. Am. Chem. Soc.* **2015**, *137*, 6097.

[192] Fabish, T.; Schleifer, D. *Carbon* **1984**, *22*, 19.

[193] Loutfy, R. O. *Carbon* **1986**, *24*, 127.

[194] Gileadi, E. *Electrode Kinetics for Chemists, Chemical Engineers and Materials Scientists*; Wiley-VCH: New York, 1993.

[195] Lu, Q.; Rosen, J.; Zhou, Y.; Hutchings, G. S.; Kimmel, Y. C.; Chen, J. G.; Jiao, F. *Nat. Commun.* **2014**, *5*, 3242.

[196] Chen, J. S.; Wen, X.; Lou, D. *Small* **2013**, *9*, 1877.

[197] Poizot, P.; Laruelle, S.; Grugeon, S.; Dupont, L.; Tarascon, J.-M. *Nature* **2000**, *407*, 496.

[198] Bruce, P. G.; Scrosati, B.; Tarascon, J.-M. *Angew. Chemie* **2008**, *47*, 2930.

[199] Arico, A. S.; Bruce, P.; Scrosati, B.; Tarascon, J.-M.; Van Schalkwijk, W. *Nat. Mater.* **2005**, *4*, 366.

[200] Armand, M.; Tarascon, J.-M. *Nature* **2008**, *451*, 652.

[201] Goodenough, J. B.; Kim, Y. *Chem. Mater.* **2010**, *22*, 587.

[202] Paek, S.; Yoo, E.; Honma, I. *Nano Lett.* **2009**, *9*, 72.

[203] Courtney, I. A.; Dahn, J. R. *J. Electrochem. Soc.* **1997**, *144*, 2943.

[204] Idota, Y.; Kubota, T.; Matsufuji, A.; Maekawa, Y.; Miyasaka, T. *Science* **1997**, *31*, 1395.

[205] Wang, Y.; Lee, J. Y.; Zeng, H. C. *Chem. Mater.* **2005**, *17*, 3899.

[206] Kim, C.; Noh, M.; Choi, M.; Cho, J.; Park, B. *Chem. Mater.* **2005**, *17*, 3297.

[207] Deng, Y.; Fang, C.; Chen, G. *J. Power Sources* **2016**, *304*, 81.

[208] Courtney, I. A.; Dahn, J. R. *J. Electrochem. Soc.* **1997**, *144*, 2045.

[209] Wang, C.; Zhou, Y.; Ge, M.; Xu, X.; Zhang, Z.; Jiang, J. Z. *J. Am. Chem. Soc.* **2010**, *132*, 46.

[210] Wang, C.; Du, G.; Stahl, K.; Huang, H.; Zhong, Y.; Jiang, J. Z. *J. Phys. Chem. C* **2012**, *116*, 4000.

[211] Kim, H.; Park, G. O.; Kim, Y.; Muhammad, S.; Yoo, J.; Balasubramanian, M.; Cho, Y.; Kim, M.; Lee, B.; Kang, K.; Kim, H.; Kim, J. M.; Yoon, W.-S. *Chem. Mater.* **2014**, *26*, 6361.

[212] Wang, G.; Shen, X.; Yao, J.; Park, J. *Carbon* **2009**, *47*, 2049.

[213] Dahn, J. R.; Zheng, T.; Liu, Y.; Xue, J. S. *Science* **1995**, *270*, 590.

[214] Yoo, E. J.; Kim, J.; Hosono, E.; Zhou, H. S.; Kudo, T.; Honma, I. *Nano Lett.* **2008**, *8*, 2277.

[215] Bhardwaj, T.; Antic, A.; Pavan, B.; Barone, V.; Fahlman, B. D. *J. Am. Chem. Soc.* **2010**, *132*, 12556.

[216] Zeng, M.; Xiao, Y.; Liu, J.; Lu, W.; Fu, L. *Adv. Electron. Mater.* **2016**, *2*, 1500456.

[217] Kim, Y.; Lee, H.; Sohn, H. *Electrochem. Commun.* **2009**, *11*, 2125.

[218] Braddock, D. C.; Clarke, J.; Rzepa, H. *Chem. Commun.* **2013**, *49*, 11176.

[219] Durantini, E. N.; Silber, J. J. *Synth. Commun.* **1999**, *29*, 3353.

[220] Fuse, S.; Sugiyama, H.; Kobayashi, D.; Iijima, Y.; Matsumurua, K.; Tanaka, H.; Takahashi, T. *Eur. J. Org. Chem.* **2015**, *21*, 4756.

[221] Baker, G. A.; Bright, F. V.; Detty, M. R.; Pandey, S.; Stilts, C. E.; Yao, H. *J. Porphyr. Phthalocya.* **2000**, *4*, 669.

[222] Sogawa, H.; Miyahi, Y.; Shiotsuki, M.; Sanda, F. *Macromolecules* **2013**, *46*, 8896.